2017

Device physics of perovskite solar cells

Liang Zhang
Iowa State University

Device physics of perovskite solar cells

by

Liang Zhang

A dissertation submitted to the graduate faculty

in partial fulfillment of the requirements for the degree of

DOCTOR OF PHILOSOPHY

Major: Electrical Engineering

Program of Study Committee:
Vikram Dalal, Major Professor
Rana Biswas
Mani Mina
Jiming Song
Kris De Brabanter

The student author and the program of study committee are solely responsible for the content of this dissertation. The Graduate College will ensure this dissertation is globally accessible and will not permit alterations after a degree is conferred.

Iowa State University

Ames, Iowa

2017

DEDICATION

This dissertation is dedicated to my fiancée, Furong, who accompanies me throughout the years of my PhD and keeps encouraging me when I hit rock bottom. Without her, my life would not be as beautiful as it is today. It is also dedicated to my parents, Zhichong and Youdi, for their love, patience, and inspiration. Words fail me when it comes to express how much I love them. I would also like to express my deepest gratitude to my grandparents who have played a significant role in shaping me into who I am today. This work is not possible without those people above. I am deeply indebted for what they have brought to my life.

TABLE OF CONTENTS

ACKNOWLEDGMENTS

It is my privilege to work under the guidance of Dr. Vikram Dalal. Not only has he led me towards the field of semiconductor device physics and let me experience the beauty of it, but also inspired me with his research spirit and passion, which would influence me throughout the rest of my life no matter which field I work in. I feel so fortunate to have a PhD advisor like him and really appreciate his support and mentorship in those years.

I would like to thank my committee members: Dr. Rana Biswas, Dr. Jiming Song, Dr. Mani Mina, and Dr. Kris De Brabanter for their great lecture, guidance, and encouragement during my study and research in Iowa State.

During my PhD life in MRC, I have met so many great and helpful people here. I would like to thank Max Noack for his consistent technical support, inspiration as well as fruitful discussion. I appreciate the help from Wai Leung with lab training and experiments. Special thanks go to senior group members: Mehran Samiee, Pranav Joshi, and Siva Konduri for their help and guidance in the early stage of my research. I really enjoy the discussion with Mehran and learnt a lot from him. Thank my lab mates for their help and friendship: Hisham Abbas, Ranjith Kottokkaran, Istiaque Hossain, Satvik Shah, Balaji Ganapathi, Satyapal Nehra, Mahendra Dhaka, Dipak Paramanik, Behrang Bagheri, Sabrina Stark, Harsh Gaonkar, Moneim Ismail, Tanvir Muntasir, and Mohamed El-Henaway.

I would also like to thank all my friends, department faculties and stuffs for making my stay in Ames a great memory in my life.

Finally, thank National Science Foundation for supporting my research.

ABSTRACT

Perovskite solar cell has attracted great attention recently because of its great potential. However, detailed information on electronic defects is still unknown. Here, we report Urbach energy of tail states (16 meV) with sub-gap QE measurement and two defect bands (0.24 eV and 0.66 eV) with CFT measurement. Meanwhile, the attempt-to escape frequency (~10^{11} Hz) of perovskite is calculated with our CFT data. Diffusion length of perovskite is measured by both photo-conductivity and QE vs. bias, and both methods give a diffusion length of 4-6 μm for perovskite, which is the reason we can make high efficient solar cells with it.

Being the top cell of a perovskite-silicon tandem solar cell is one of perovskite's most importance applications. In order to do that, the perovskite layer has to be sandwiched by two transparent layers, which makes the device a bifacial solar cell. In this project, we successfully made a bifacial perovskite solar cell by depositing CdS:In and ZnO:Al on top of perovskite. The CdS:In buffer layer effectively protects perovskite from plasma attacking during ZnO:Al sputtering. By optimizing the thickness of CdS:In, we achieved 14+% efficiency with light coming either from the top or bottom. This was the second best bifacial perovskite solar cell in the field at that time. The ZnO:Al layer also provided a great encapsulation to protect perovskite, which greatly improved the perovskite lifetime in ambient air from less than 20 minutes to more than 3 months.

As the top cell of perovskite-silicon tandem, the photo-stability of perovskite layer is extremely important. Systematic experiment and detailed device data analysis were performed to understand its degradation mechanism. The photon-induced degradation data of perovskite solar cell suggested that its degradation mechanism is much different from that of a-Si and organic solar cells. We found the degradation of perovskite under light exposure is attributed

to the generation and migration of ions. We proposed an ion-generation-migration model which explains every device behavior during the degradation and recovery process of perovskite solar cell. Quantitative relationship between performance degradation and ion density was investigated by transient ionic current measurement. We also provided two approaches to mitigate photon-induced degradation. By increasing the grain size or adding excess PbI_2, the degradation was mitigated by 50% respectively. The ion density we calculated from transient ionic current also showed significant reduction by applying those approaches.

CHAPTER 1

INTRODUCTION TO SOLAR ENERGY AND SOLAR CELL

1.1 Introduction to Solar Energy

Energy is the foundation for the development of the human civilization. Since the first industrial evolution, when the world energy consumption started to climb up, it has become the driving force behind technology development and innovation, which has transformed human lifestyle dramatically to the one we are having now. Especially after the end of World War II, there was a significant increase in energy consumption in industrialized and transition countries due to industrialization, urbanization, and technology boom. According to BP's report in 2016[1], from 1965 to 2015, the world energy consumption has increased from 43 petawatt-hour (PWh) to 153 PWh, which is plotted in Figure 1.1. As seen in the figure below, the growth of energy consumption every year is almost in a linear trend, and leads to a growth rate of about 2.2 PWh/year. This energy consumption growth is expected to continue since there are lots of developing countries among the world where energy hunger still exists.

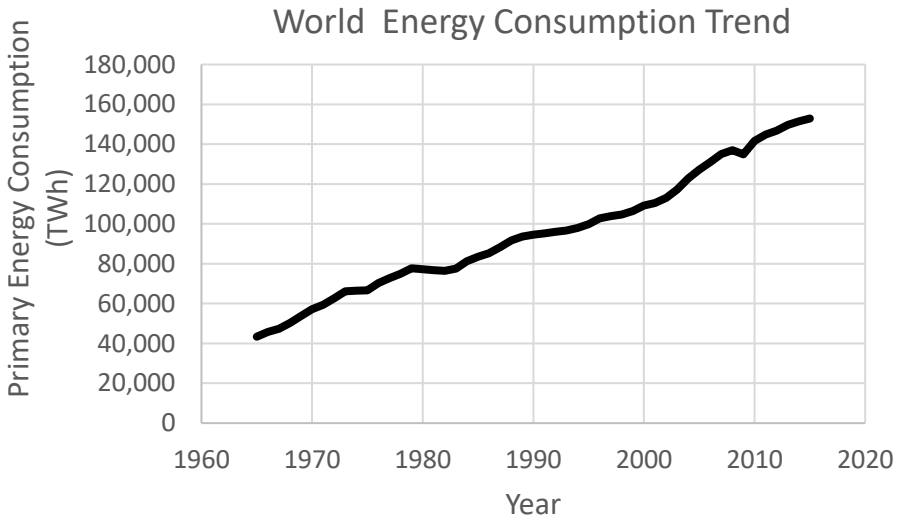

Figure 1.1: World energy consumption from 1965 to 2015[1].

Despite significant improvement of renewable energy conversion efficiency and technology in the last several decades, most of the energy (~80%) we are using still comes from fossil fuels[2], as shown in Figure 1.2. The burning of fossil fuels, especially unpurified coals, releases emissions and dusts to the environment. The emission of greenhouse gases is potentially a cause of global warming and climate change, which could tremendously impair the ecosystem and jeopardize the safety of human activity. The soot emission, on the other hand, is a great hazard to human health.

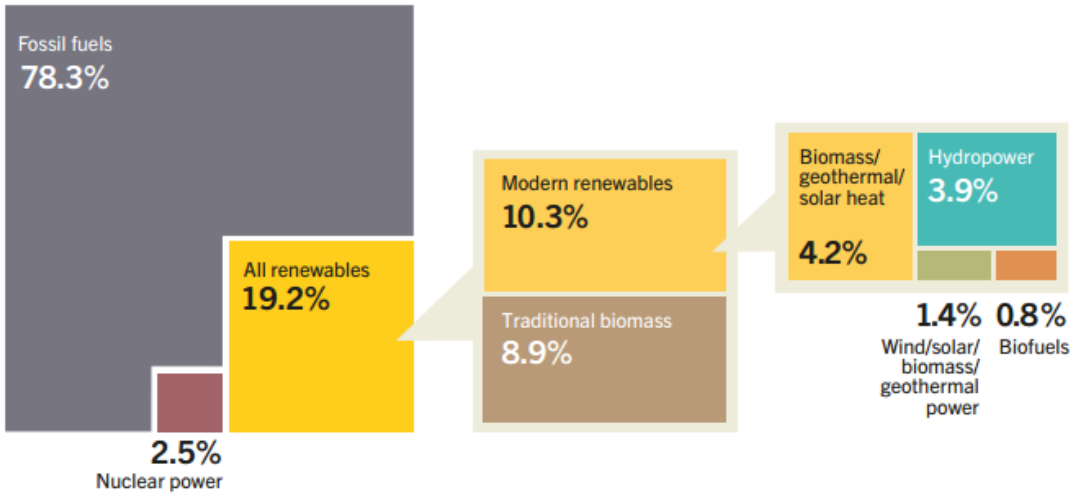

Figure 1.2: Estimated renewable energy share of global final energy consumption in 2014[2].

Renewable energy is a solution of solving energy hunger problem and mitigating environment impact of current energy system. Compared with other renewable energy types, solar energy has the advantage of better accessibility, low maintenance requirement, and low noise.

As the most abundant energy source on earth, solar energy can theoretically provide as much as 89 petawatt (PW) of energy for human utilization. However, due to the geographical accessibility, the energy we can harvest with current technology is in the range of a few

thousand terawatt (TW)[3]. Nevertheless, this amount of energy is more than enough to meet the world energy consumption demand.

1.2 Introduction to Solar Cell

There are many ways to harvest solar energy. It can be converted directly into thermal energy, and one of applications is solar water heater. Another way is using concentrated solar power (CSP). CSP uses reflector arrays to concentrate sunlight onto a small area, in which solar energy is converted into heat and drives a heat engine (normally a steam engine) to generate electricity. Among all types of solar energy conversion technology, photovoltaics (PV) is the most popular and has the highest technical potential (~7500 TW)[3].

PV power generation employs multiple solar panels composed of a number of solar cells. Solar cells can convert solar energy into electricity directly.

Figure 1.3: CSP system[4] (left) and PV system[5] (right).

Despite the advantages brought by PV technology, PV was known as an expensive alternative to current fossil fuel, which limit its application. Fortunately, as shown in Figure 1.4 (a), the price of PV has been dropped significantly in the last 40 years, from about 100$/watt to 0.6$/watt[6]. The decrease of PV price has led to great increase of PV installation

worldwide. Especially after 1992, the installation shot up exponentially to a current level of 65 GW[7].

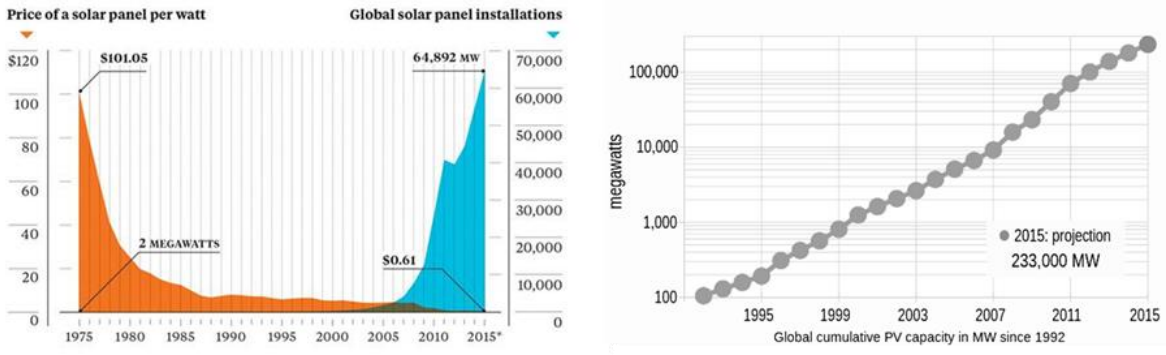

Figure 1.4: (a) Solar panel price and global installation in the last 40 years[6], (b) Exponential increase of solar panel installation after 1992[7].

Despite vast improvement in worldwide PV installation, PV still accounts for a small portion in our current energy system; only about 1.2% of electricity we use comes from PV[2]. The reason behind it is still price. According to the annual report from US Energy Information Administration (EIA), the levelized cost of energy (LCOE) of PV is 12.5 ¢/KWh, which is 67% higher when compared with that of natural gas as we can see in Figure 1.5.

LCOE is one of the primary metrics for the cost of electricity in utility industry. The calculation of LCOE considers all the cost during a system's expected lifetime (initial investment, maintenance, fuel, transportation, etc.), and divided it by the system's lifetime-expected power output. The introduction of LCOE creates a uniform price calculation standard and makes the price comparison of different energy types possible.

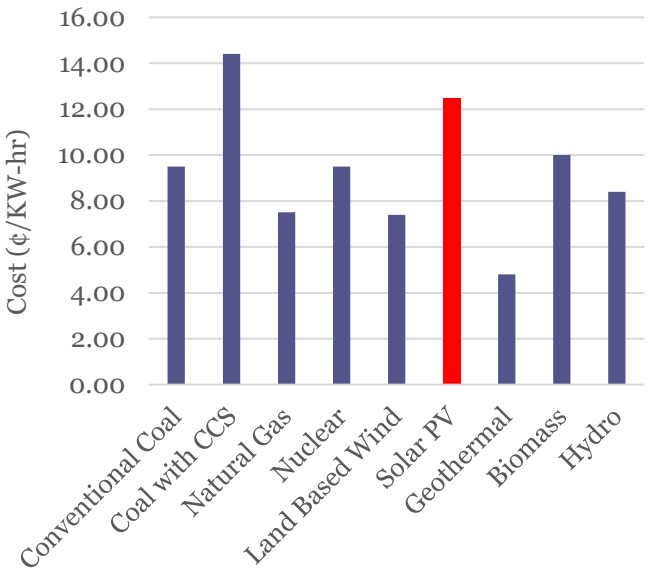

Energy Plant Type	Lifetime Cost (¢/KWh)
Offshore Wind	20.0
Peaker Natural Gas	18.0
Coal with CCS	14.4
PV Solar	12.5
Gas Combined Cycle with CCS	10.0
Biomass	10.0
Advanced Nuclear	9.5
Conventional Coal	9.5
Hydro-electric	8.4
Natural Gas Combined Cycle	7.5
Land Based Wind	7.4
Geothermal	4.8

Figure 1.5: Levelized Cost Of Energy (LCOE) for various sources of electricity as of June 2015[8].

Figure 1.6 illustrates the cost benchmark of different size PV systems from 2009 to 2016[9]. The PV module price still accounts for most of system cost (~25%-50%) although it has already decreased significantly in the last few decades. In order to make PV more competitive in our current energy system, there has to be a continuous reduction of module cost. According to US Department of Energy's SunShot initiative, the goal is to reduce the price of PV power to less than 1$/watt by the end of 2020[10].

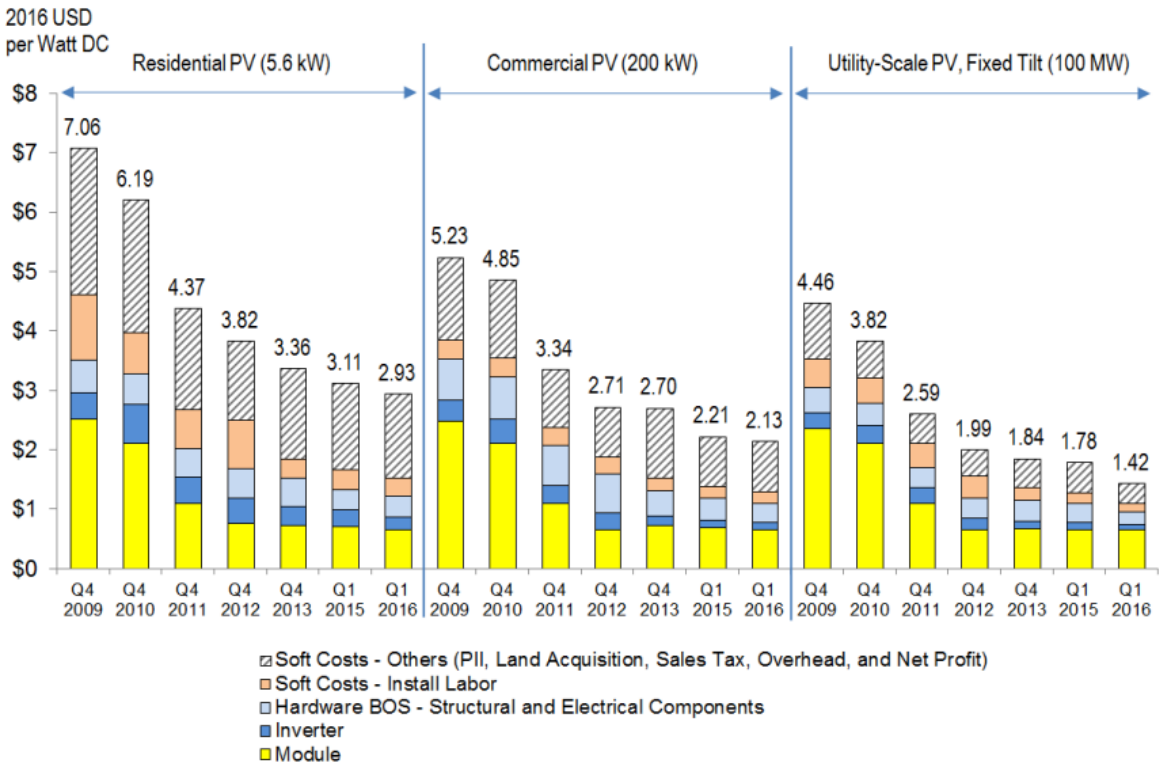

Figure 1.6: PV cost benchmark summary, Q4 2009-Q1 2016[9].

CHAPTER 2

DEVICE PHYSICS OF SOLAR CELLS

2.1 Introduction

A solar cell is a semiconductor device which coverts solar energy directly to electric energy, and it is mostly made of a PN junction as shown in Figure 2.1. When light enters a solar cell, it will get absorbed and give rise to electron-hole pairs. Those electrons and holes will drift and diffuse, and get collected on the contacts of a solar cell, which would generate photo-current inside the solar cell. This is how we harvest solar energy by using a PN junction.

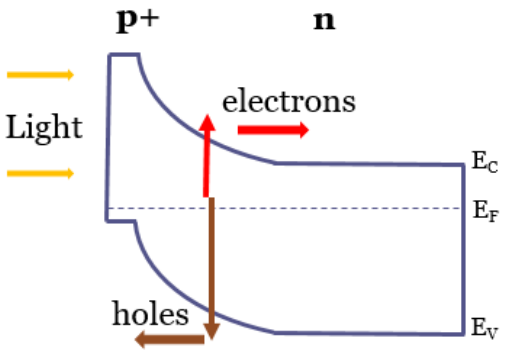

Figure 2.1: Band diagram of a typical solar cell. This solar cell is made of a p^+n junction. E_C, E_V, and E_F are the conduction band, valence band, and Fermi level of the material respectively.

Solar cells can be made with various structures. Generally, they can be categorized as two types, PIN and NIP. As shown in Figure 2.2, in both cases, solar cell's main layer (i-layer) is sandwiched by a p^+ layer and a n^+ layer. The difference between a PIN and a NIP structure is, in PIN structure, light comes from p^+ side, while in NIP, it comes from n^+ side.

In either PIN or NIP structure, the i-layer is normally a lightly doped semiconductor with high absorption coefficient. Sometimes, it is also called as main layer since it absorbs most of photons in a solar cell. The p^+ layer and n^+ layer are heavily doped p-type and n-type

semiconductors. They are used to create high internal electric filed in the i-layer and make i-layer fully depleted. Electrons and holes generated in the i-layer will drift under the effect of this electric field. Electrons will be collected in n^+ layer while holes will be collected in p^+ layer. Therefore, sometimes people call n^+ layer as electron transport layer (ETL) and p^+ layer as hole transport layer (HTL).

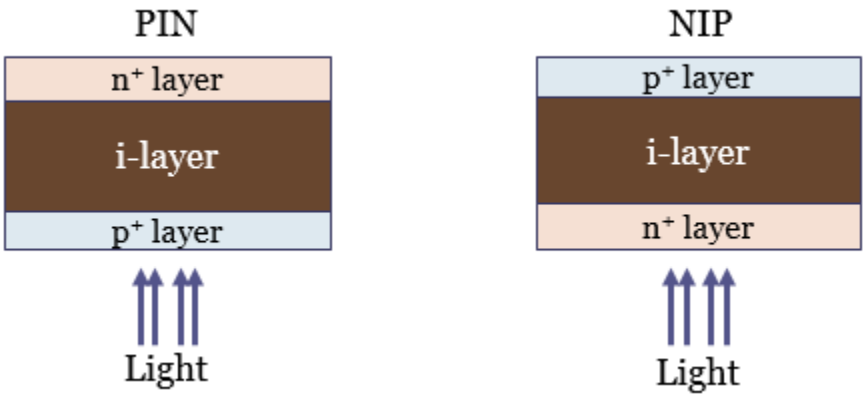

Figure 2.2: Solar cell device structure, PIN (left) and NIP (right).

Power conversion efficiency (PCE), or simply efficiency, is the most important parameter of a solar cell. It is defined as the ratio of maximum output power to the input power (solar irradiation power) of a solar cell. Efficiency of a solar cell is determined by multiple factors, among which the most important ones are the properties of absorbing material and device structure.

Figure 2.3 illustrates the basic operation of a solar cell. The solar cell efficiency depends on following processes:

1) Generation process. Free electron-hole pairs are generated when light is absorbed in the solar cell. Those free carriers will lead to a photo-current when being

collected. Therefore, we want the generation rate to be as high as possible to achieve higher efficiency.

2) Recombination process. Free electrons and holes annihilate each other, which is the reverse process of generation. Recombination process reduces the carrier concentration in the solar cell, and leads to reduction of conversion efficiency. So, it is very much important to understand the recombination process, and design the solar cell correspondingly to minimize the recombination rate.

3) Carrier transport. Free carriers not involved in the recombination will transport to the terminals of a solar cell and get collected. Depending on the electric field distribution and carrier concentration distribution, transport process can be either dominated by drift or diffusion. A careful design of transport process in a solar cell is critical to achieve high collection probability and thus high efficiency.

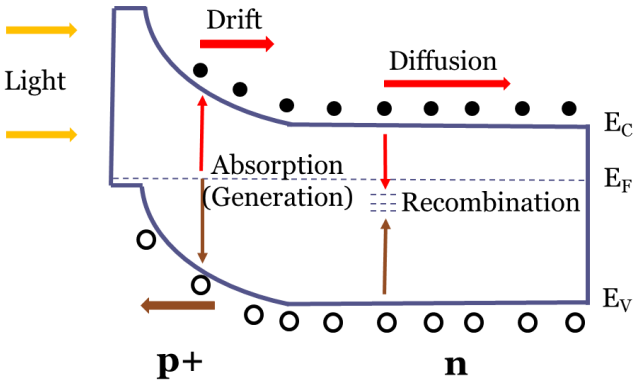

Figure 2.3: Generation, recombination, and transport of carriers inside a solar cell. Free carriers are generated by generation process and annihilated by recombination process.

2.2 Absorption

Generation of free carriers originates from the absorption of photons. When a photon enters a material, it will excite an electron from a low-energy state to a high-energy state after

being absorbed. In a semiconductor, this state transition can be divided into two types, band-to-band transition and transition through defect states. Band-to-band transition happens when the photon energy hv is higher than the bandgap, as shown in Figure 2.4. After absorbing the photon energy, an electron is excited from valence band to conduction band. The excess energy, hv-Eg, is dissipated as thermal energy while the excited electron collides with the lattice and finally relaxes to the bottom of conduction band. When the photon energy is less than the bandgap, transition of states can also be achieved through the trap states with the forbidden gap, which is shown in Figure 2.5. It can be done through either tail states or mid-gap states. This type of absorption provides us an effective way to probe the band structure of a semiconductor.

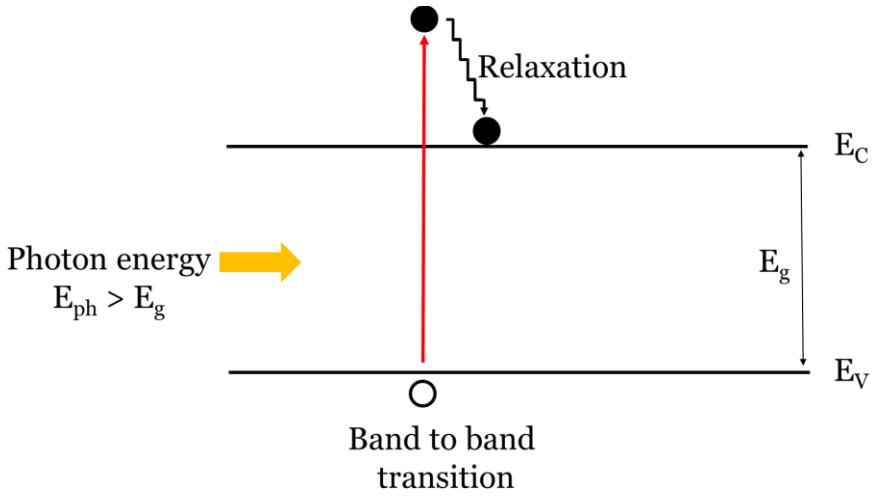

Figure 2.4: Absorption of photon through band-to-band transition.

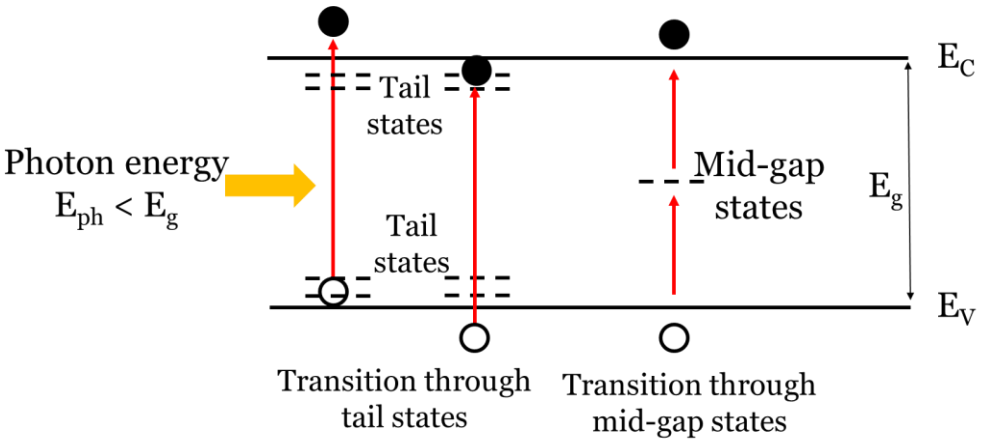

Figure 2.5: Absorption process through tail states and mid-gap states.

Absorption coefficient is a parameter used to define how efficient a material absorbs photons. For a band-to-band transition, it can be considered in two kinds of situation: direct transition and indirect transition, as shown in Figure 2.6. In direct transition, only photon is involved, making it a momentum-conserving transition. While in indirect transition, a phonon will be involved to make a state transition with momentum change.

The absorption coefficient of direct transition can be expressed as in the following equation[11].

$$\alpha = A\left(hv - E_g\right)^{\frac{1}{2}} \tag{2.1}$$

Where parameter A is correlated with the effective electron and hole masses.

In indirect transition, the absorption coefficient would be[11]

(1) When the transition involves phonon absorption

$$\alpha = \frac{A\left(hv - E_g + E_p\right)^2}{e^{\frac{E_p}{kT}} - 1} \tag{2.2}$$

When the transition involves phonon emission,

$$\alpha = \frac{A\left(hv - E_g - E_p\right)^2}{1 - e^{-\frac{E_p}{kT}}} \tag{2.3}$$

Here, Ep is the energy of photon that is being absorbed or emitted.

The absorption coefficient of transition through tail states or mid-gap states is normally very small due to their low density of states. However, it provides important information regarding the sub-gap states distribution, and can be expressed as

$$\alpha = Ae^{\frac{hv}{E_0}} \tag{2.4}$$

Here, E_0 is called Urbach energy[12], which correlate with the tail states and mid-gap states.

When the light travels through the material, its intensity will gradually decrease due to the absorption.

$$I(x) = I(x = 0)e^{-\alpha x} \tag{2.5}$$

Where I is the light intensity at distance x in the material.

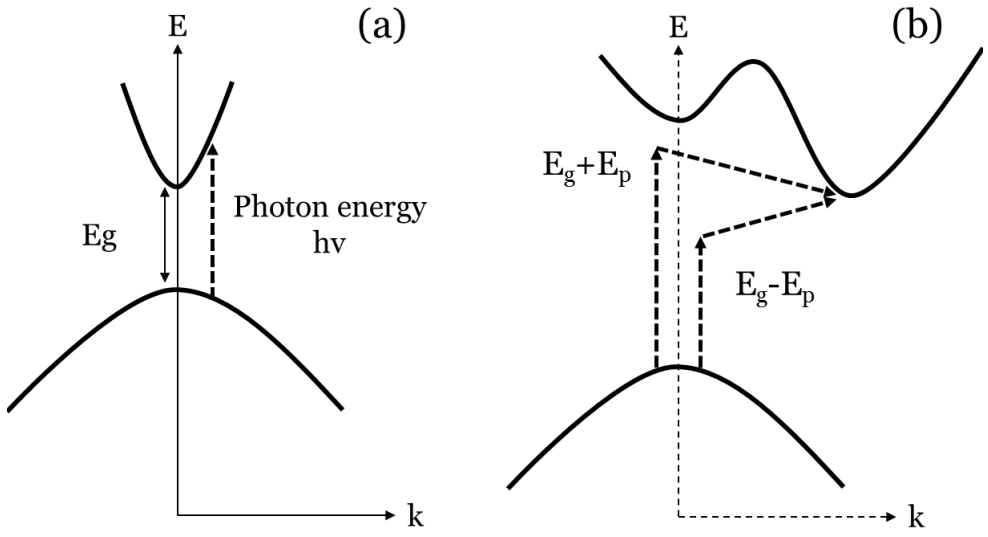

Figure 2.6: Absorption: (a): Direct allowed transition (b): Indirect transition.

2.3 Recombination

As the reverse process of generation, recombination leads to the decrease of carrier concentration in the materials. Excited electrons will fall back to the valence band, and the energy will be released either in the form of photons, which is called radiative recombination, or phonons, which is called non-radiative recombination. Generally, as shown in Figure 2.6, there are three types of recombination, band-to-band recombination, trap-assisted recombination, and Auger recombination. They will be discussed in the following part.

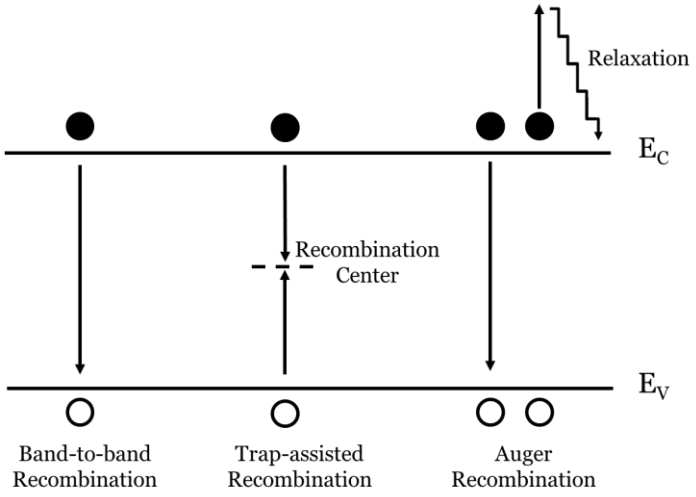

Figure 2.7: Recombination mechanisms: Band-to-band, trap-assisted, and Auger recombination.

2.3.1 Band to band recombination

In band-to-band recombination[13,14], the electron falls directly from a conduction band state into a valence band state. A photon will be generated when the electron energy is released, which makes it a radiative recombination.

The recombination rate can be expressed in the following equation:

$$R = c_B(np - n_i^2) \tag{2.6}$$

Here, c_B is the recombination coefficient. n, p, and n_i are the electron concentration, hole concentration and intrinsic carrier concentration respectively.

When the material is under low level charge injection (small signal condition, Δn, Δp << n) and it is n-type doped (n>>p and n>>n_i), equation (2.6) can be simplified as:

$$R = c_B n \Delta p = \frac{\Delta p}{1/c_B n} = \frac{\Delta p}{\tau_B} \tag{2.7}$$

Where $\tau_B = \frac{1}{c_B n}$ is the minority lifetime. It is only controlled by the majority carrier (electrons in this example) concentration.

When the material is under high level charge injection (large signal condition, Δn, Δp >> n_o, p_o), equation (2.6) would be simplified as:

$$R = c_B \Delta n \Delta p = c_B np = c_B n^2 = c_B p^2 \tag{2.8}$$

2.3.2 Trap-assisted recombination

Trap-assisted recombination[13] is also called Shockley-Read-Hall (SRH) recombination. In trap-assisted recombination, an electron and a hole will be annihilated when captured by a trap state together. It can happen either in the bulk of a semiconductor or on the interface. Trap-assisted recombination can be expressed as follows[13]:

$$R = \frac{np - n_i^2}{\tau_p(n + n_1) + \tau_n(p + p_1)} \tag{2.9}$$

Here, $\tau_p = \frac{1}{c_p N_T}$ and $\tau_n = \frac{1}{c_n N_T}$ are the minority carrier lifetime of holes and electrons respectively. $n_1 = n_i e^{(E_{T'} - E_i)/kT}$ and $p_1 = n_i e^{(E_i - E_{T'})/kT}$ are computable constants and follow the rule $n_1 p_1 = n_i^2$.

The minority lifetime, τ_p or τ_n, is controlled by the defect density N_T.

When the device is under low level charge injection condition (small signal condition, $\Delta n, \Delta p << n$), equation (2.9) will be simplified as:

$$R = \frac{\Delta n}{\tau_n} = c_n \, \Delta n \, N_T \quad \text{(p type material)} \tag{2.10}$$

$$R = \frac{\Delta p}{\tau_p} = c_p \, \Delta p \, N_T \quad \text{(n type material)} \tag{2.11}$$

So, in low signal condition, trap-assisted recombination is determined by the minority carrier life lifetime, which is inverse proportional to the defects concentration.

When the device is injected with large amount of charge (large signal condition, $\Delta n, \Delta p >> n_o, p_o$), equation (2.9) can be expressed as:

$$R = \frac{\Delta n}{\tau_n + \tau_p} = \frac{\Delta p}{\tau_n + \tau_p} \tag{2.12}$$

In this case, the effective lifetime, $\tau = \tau_n + \tau_p$, is larger than that in small signal condition. This is the part where trap-assisted recombination is different from band-to-band recombination.

2.3.3 Auger recombination

In an Auger recombination[13] process, the energy released by a band-to-band transition or trap-assisted transition will give rise to the excited free electron in the conduction band. This high-energy electron will lose its energy while colliding with the lattice, and finally relaxes to the conduction band. Auger recombination usually happens in degenerate semiconductor or a high-level injection condition where free carriers are in high concentration.

Auger recombination rate can be expressed in the following format:

$$R = c_A n(np - n_i^2) \quad (n \; type \; material) \tag{2.13}$$

$$R = c_A p(np - n_i^2) \quad (p \; type \; material) \tag{2.14}$$

In a n-type material with low-level injection, Auger recombination rate equation can be reduced to

$$\mathrm{R} = c_A n_o^2 \Delta p = \frac{\Delta p}{1/c_A n_o^2} = \frac{\Delta p}{\tau_p} \tag{2.15}$$

It shows that Auger recombination rate is a quadratic function of doping concentration. This is the reason Auger recombination dominates in materials with high carrier concentration.

Generally, all three types of recombination can happen at the same time. Therefore, the overall minority lifetime would be

$$\frac{1}{\tau} = \frac{1}{\tau_B} + \frac{1}{\tau_T} + \frac{1}{\tau_A} \tag{2.16}$$

Where τ_B, τ_T, and τ_A are band-to-band, trap-assisted, and Auger recombination lifetime.

2.4 Charge Collection

Charge collection mechanism consists of diffusion-based transport and drift-based transport[13,15]. Diffusion-based transport is driven by the gradient of carrier concentration in the semiconductor while drift-based transport is powered by the electric field in the material. Since a solar cell is biased at maximum-power condition during operation where the electric filed along the device is significantly smaller than that in short-circuit condition, it is mostly dominated by diffusion-based transport. For the device with poor diffusion length, charge collection can be significantly improved by replacing diffusion-based transport with drift-based transport.

When considering both diffusion-based and drift-based charge transport, the transport equation can be written in the following form.

$$\frac{\partial \Delta n}{\partial t} = D' \frac{\partial^2 \Delta n}{\partial x^2} + \mu' \varepsilon \frac{\partial \Delta n}{\partial x} + G - R \tag{2.17}$$

Where Δn is the excess electron concentration, D' is the ambipolar diffusion coefficient, μ' is the ambipolar mobility, ε is the electric field, G and R are the generation and recombination rate, respectively.

Ambipolar diffusion coefficient and ambipolar mobility are expressed as

$$\mu' = \frac{\mu_n \mu_p (p - n)}{n\mu_n + p\mu_p} \tag{2.18}$$

$$D' = \frac{n\mu_n D_p + p\mu_p D_n}{n\mu_n + p\mu_p} \tag{2.19}$$

In a p-type semiconductor with low-level charge injection, equation (2.17) can be expressed as

$$\frac{\partial \Delta n}{\partial t} = D_n \frac{\partial^2 \Delta n}{\partial x^2} + \mu_n \varepsilon \frac{\partial \Delta n}{\partial x} + G - \frac{\Delta n}{\tau_n} \tag{2.20}$$

Similar change can be also applied for n-type semiconductor

$$\frac{\partial \Delta p}{\partial t} = D_p \frac{\partial^2 \Delta p}{\partial x^2} - \mu_p \varepsilon \frac{\partial \Delta p}{\partial x} + G - \frac{\Delta p}{\tau_n} \tag{2.21}$$

From both equation (2.20) and (2.21), we found that the transport process in solar cell is controlled by minority carriers instead of majority carriers.

2.4.1 Diffusion-based transport

In both equation (2.20) and (2.21), the first term in the right-hand side of the equation represents the diffusion-based transport process. If we consider a sample with no charge generation and assume that there is no electric field in the material, which eliminate the second

term in the right-hand side of the equation, equation (2.20) under steady state will be reduced to

$$\frac{\partial \Delta \mathrm{n}}{\partial \mathrm{t}} = D_n \frac{\partial^2 \Delta \mathrm{n}}{\partial x^2} - \frac{\Delta \mathrm{n}}{\tau_n} = 0 \tag{2.22}$$

The solution will be

$$\Delta \mathrm{n} = \Delta \mathrm{n}(\mathrm{x} = 0) e^{-\frac{x}{L_n}} \tag{2.23}$$

Here, $L_n = \sqrt{D_n \tau_n}$ is the minority diffusion length.

From equation (2.23), we can see that the minority carrier concentration will decay exponentially under diffusion-based transport. When the diffusion length L_n is significantly large than the device thickness t, there will not be too much minority carrier loss if we compare $\Delta \mathrm{n}(\mathrm{x} = \mathrm{t})$ with $\Delta \mathrm{n}(\mathrm{x} = 0)$.

2.4.2 Drift-based transport

For solar cells with high diffusion length, diffusion-based transport can be enough to assure high charge collection probability. However, in solar cells with low diffusion length, such as organic solar cells, we need electric field (drift-based transport) to improve the charge collection.

If we only consider the effect of electric field under steady state condition, equation (2.21) can be expressed as

$$\frac{\partial \Delta \mathrm{p}}{\partial \mathrm{t}} = \mu_p \varepsilon \frac{\partial \Delta \mathrm{p}}{\partial \mathrm{x}} - \frac{\Delta \mathrm{p}}{\tau_p} = 0 \tag{2.24}$$

The solution gives

$$\Delta \mathrm{p} = \Delta \mathrm{p}(\mathrm{x} = 0) e^{-\frac{x}{R_p}} \tag{2.25}$$

Where $R_p = \mu_p \tau_p \varepsilon$ is the drift range of minority holes[16]. Notice that equation (2.25) is in the same form with equation (2.23), and the only difference is we used drift range R_p instead of diffusion length L_n.

When both diffusion-based transport and drift-based transport exist, a critical electric filed[17] is defined as

$$\varepsilon_c = \frac{kT}{qL_p} \tag{2.26}$$

Which is the electric filed when $L_p = R_p$

So, when the electric filed $\varepsilon > \varepsilon_c$, carrier transport is dominated by drift, and when $\varepsilon < \varepsilon_c$, carrier transport is dominated by diffusion.

Drift-based transport is extremely important in materials with low minority diffusion length, such as amorphous silicon and organics polymers. In a solar cell made of those materials, we have to create a strong internal electric field to promote charge transport by sandwiching the i-layer with p+ and n+ layer, which is a p-i-n structure shown in Figure 2.8. The direction of electric field created by this p-i-n structure is from right to left. So, when the electron-hole pairs are generated in the a-Si i-layer, those electrons and holes will be swept towards the n^+ layer and p^+ layer respectively before recombining with each other. Figure 2.9 illustrates how electric field (drift-based transport) helps minority transport in a semiconductor with low diffusion length. It depicts the carrier density distribution in a uniform bar with holes injected at x=0 and electric field applied only at x>0. With the help of drift-based transport, the carrier density decays much slower in the region where x>0.

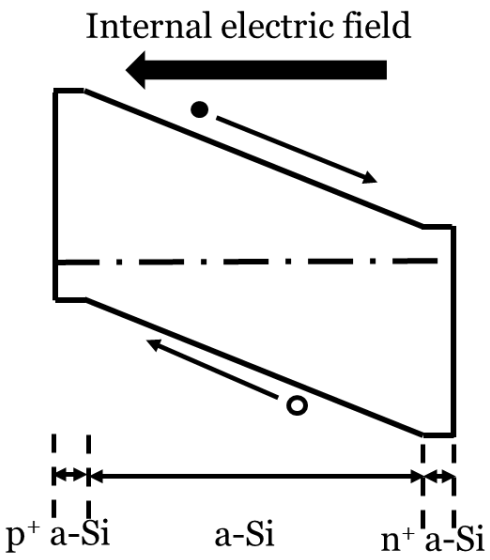

Figure 2.8: Amorphous silicon solar cell with p-i-n structure: Internal electric field promotes electrons and holes transport.

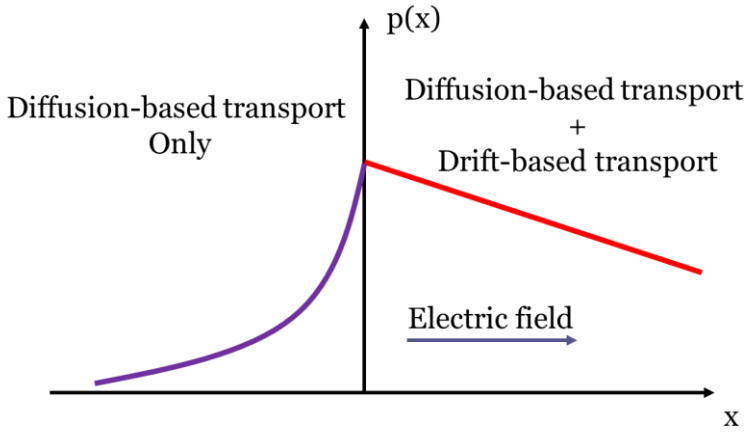

Figure 2.9: Carrier density in a uniform bar with holes injected at x=0 and electric field applied only at x>0.

2.5 Shockley-Queisser (SQ) limit

In the last three sections, the generation, recombination, and transport of free carriers have been discussed. So, under standard solar illumination, the efficiency of a solar cell can be

calculated by using the generation, recombination and transport equations with proper assumptions. This work was done by Shockley and Queisser in 1961[18]. In their calculation, they only considered absorption loss, black-body radiation loss, and radiative recombination, which set the upper limit for the achievable solar cell efficiency. The result of their work is depicted in Figure 2.10. The maximum efficiency increases with bandgap and reaches the 34% at bandgap of 1.34 eV, then it decreases with bandgap due to absorption loss.

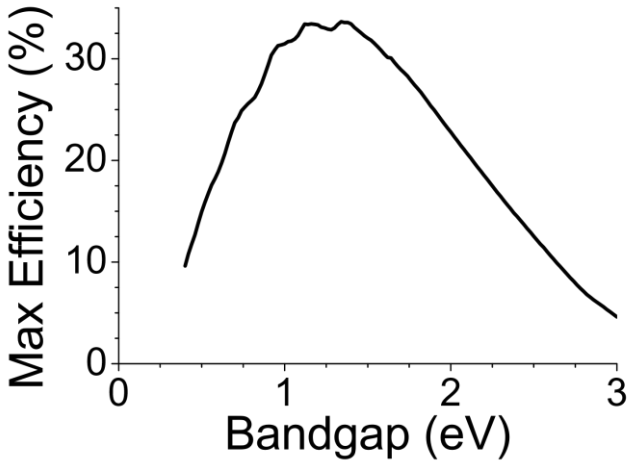

Figure 2.10: Maximum efficiency vs. bandgap for single junction solar cell[19].

Figure 2.11 shows how the energy loss is distributed at each bandgap. When the bandgap is less than 1.34 eV, most of the energy loss originates from the relaxation process. When the bandgap is higher than 1.34 eV, the energy loss is dominated by absorption loss.

There are multiple ways to push the solar cell efficiency over the Shockley-Queisser limit. A common method is to use a tandem structure which will be discussed later. Other proposed methods include concentrated photovoltaics, photon upconversion, hot electron capture, et al.

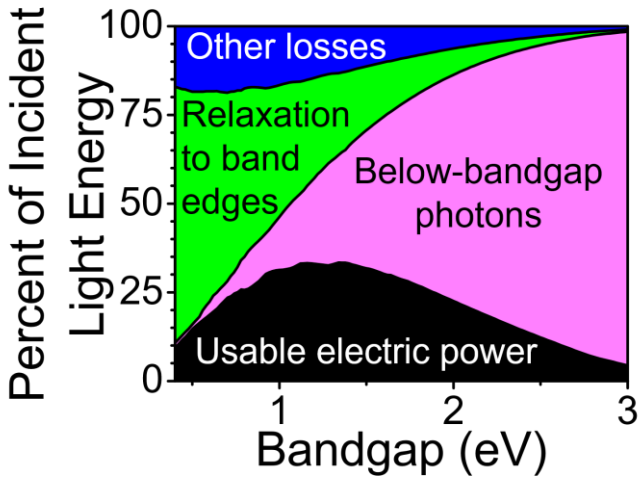

Figure 2.11: Proportion of different energy loss mechanism vs. bandgap[19].

In this chapter, we have covered the basic operation mechanism of solar cells and discussed how the generation, recombination and transport process affect the overall efficiency. We also talked about how the single junction solar cell efficiency is limited by multiple loss mechanisms.

CHAPTER 3

DEVICE CHARACTERIZATION OF SOLAR CELLS

3.1 Introduction

The electronic and optoelectronic properties are among the top interests when we study solar cells. By using proper device characterization techniques, we can study the material property, understand the device operation, and troubleshoot the problems in the solar cell.

In this chapter, I will discuss some important device characterization techniques used in our research.

3.2 Current-Voltage (IV) Measurement

Current vs. voltage (IV) measurement is one of the most basic measurement in semiconductor devices. This measurement is done by measuring the current flowing through the device while varying the voltage across it.

Before talking about the IV measurement in solar cell, I will introduce the equivalent circuit model of solar cells to give an insight of how this measurement works.

Figure 3.1 shows the equivalent circuit of a solar cell with a double-diode model. In this circuit, I_L is the generated photo-current; R_S and R_{SH} are the series and shunt resistant respectively; those two diodes represent bias dependent recombination in the solar cell.

If we apply a bias V across the circuit, the current I can be expressed as

$$\mathrm{I} = I_{01}e^{\frac{V-IR_S}{2kT/q}} + I_{02}e^{\frac{V-IR_S}{kT/q}} + \frac{V-IR_S}{R_{SH}} + -I_L \qquad (3.1)$$

Here, I_{01} and I_{02} are the diode saturation currents. Equation (3.1) is the fundamental equation that governs the current response of a solar cell in both light and dark condition.

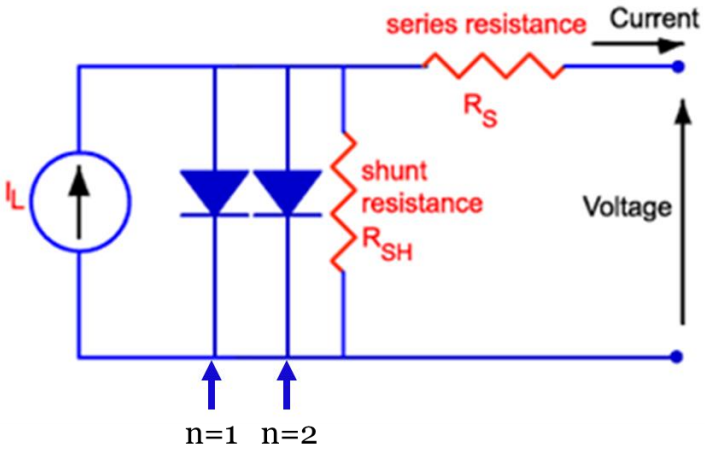

Figure 3.1: Equivalent circuit of solar cells with double-diode model under illumination.

3.2.1 Light IV measurement

Light IV is the measurement we use to determine the efficiency of a solar cell. When the solar cell is illuminated, it will generate photo-current I_L. In this case, according to equation (3.1), the IV curve we get will be the red curve in Figure 3.2. There are four important parameters in an IV curve. The first one is open-circuit voltage V_{oc}, which is the voltage when the current is 0. The second on is short-circuit current I_{sc}, which is the current when the voltage across the device is 0. The output power of a solar cell is calculated as $P = I * V$. Then, we can plot the solar cell output power vs. voltage, which is the blue curve in Figure 3.2. Clearly, it is voltage dependent, and this is the reason we have to match the impedance to achieve maximum output power when using solar cell in daily life. The third parameter, fill factor (FF), is to describe how square the IV curve is, which is defined as

$$\text{Fill facto (FF)} = \frac{P_{max}}{V_{oc} * I_{sc}} = \frac{\max(I * V)}{V_{oc} * I_{sc}} \tag{3.2}$$

Fill factor also equals to the area ratio of A and B in Figure 3.2. The last parameter, efficiency, which is the most parameter of a solar cell, is defined as

$$Efficiency = \frac{P_{max}}{P_{irradiation}} = \frac{\max(V * I)}{0.1W/cm^2} = \frac{V_{oc} * I_{sc} * FF}{area * 0.1W/cm^2} \tag{3.3}$$

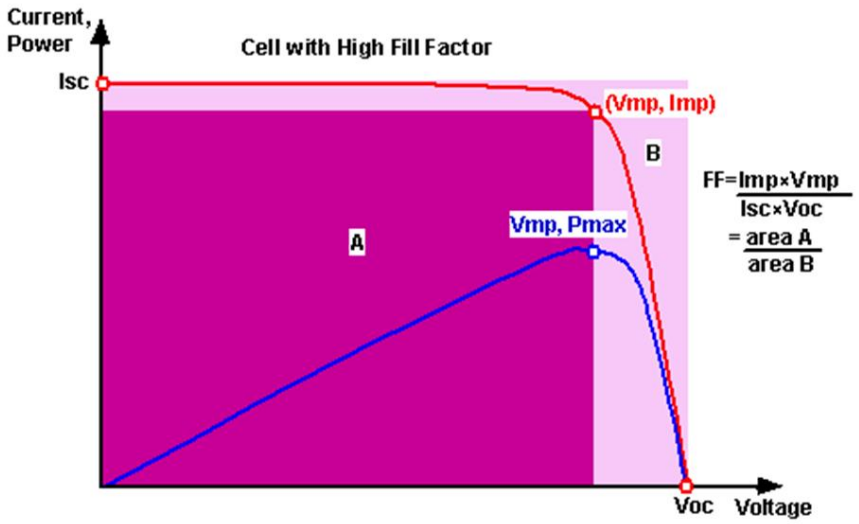

Figure 3.2: Light IV curve and output power vs. voltage curve of a solar cell[20].

Light IV measurement is also a powerful tool to figure out the resistance problem in a solar cell. According to equation (3.3), in order to achieve higher efficiency, we want the product of V_{oc}, I_{sc}, and FF to be as high as possible. V_{oc} and I_{sc} are mostly determined by material property and device structure. FF is strongly affected by the series resistant R_S and shunt resistance R_{SH} in Figure 3.1.

According to equation (3.1) and under the assumption that I_L is a constant and does not change with bias, the R_S and R_{SH} term in the equation can be expressed as the slope of the IV curve at open-circuit point and short-circuit point, which are

$$R_s = \left.\frac{\partial V}{\partial I}\right|_{V=V_{oc}} \tag{3.4}$$

$$R_{SH} = \left.\frac{\partial V}{\partial I}\right|_{V=0} \tag{3.5}$$

Figure 3.3 depicts the difference of IV curve between an ideal solar cell and a solar cell with resistance problem. The red curve (solar cell with resistance problem) has much lower fill factor when compared to the ideal one. In an ideal solar cell, the series resistance $R_s = 0$, and the shunt resistance $R_{SH} = \infty$. If the series resistance increase, the part of IV curve close to the open-circuit voltage will tilt to the left. If the shunt resistance decreases, the part close to the short-circuit point will drop, as shown in Figure 3.3.

In this way, we can calculate the shunt resistance and series resistance by measuring the light IV of a solar cell.

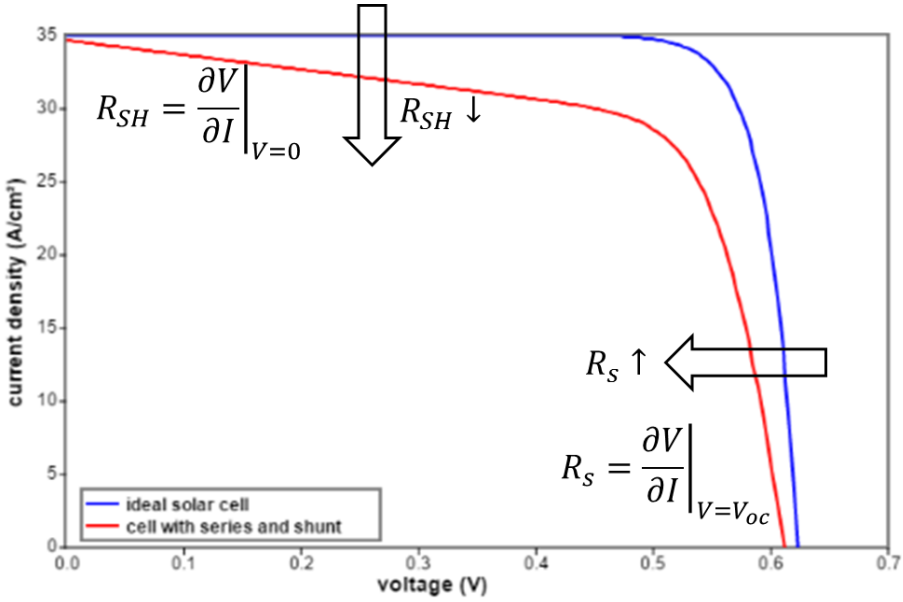

Figure 3.3: Comparison between the IV curve of an ideal solar cell (blue curve) and that of a solar cell with resistance problems (red curve)[20].

3.2.2 Dark IV measurement

Dark IV can also be used to calculate series resistance and shunt resistance. It provides better accuracy than the resistance calculation from light IV curve since the light IV curve can also be affected by other factors. For example, if the device suffers from low diffusion length,

and the solar cell has low charge collection, the IV curve will shift down even it does not have resistance problem, which would result in underestimate R_{SH} and overestimate R_s if we use light IV measurement. This issue will not happen when we use dark IV to estimate R_{SH} and R_s.

Dark IV is also a powerful tool to analyze the recombination process in the solar cell. When we apply a bias across the solar cell in the dark, the current following through the device should be

$$\mathrm{I} = I_{01}e^{\frac{V-IR_S}{2kT/q}} + I_{02}e^{\frac{V-IR_S}{kT/q}} + \frac{V-IR_S}{R_{SH}} \tag{3.6}$$

The only difference between equation (3.1) and (3.6) is the photo-current term I_L.

A typical dark IV curve is depicted in Figure 3.4. When the applied bias is low (normally 0-0.1 V), the dark current is dominated by the shunt current, which is the third term on the right-hand side of equation (3.6). Generally, low shunt resistance results from the pinholes in the i-layer or unwanted shunt path in the solar cell. When the applied bias goes higher, there will be two exponential regions, which are governed by those two exponential terms in equation (3.6). When the bias goes even higher, the dark current will be saturated and limited by the series resistance.

Since the low bias region and high bias region are dominated by shunt resistance and series resistance respectively, we can extract the information about them from those two regions. Resistance calculation from dark IV is much more accurate than that from light IV because no other factors affect the current in the dark IV measurement.

The first exponential region has an ideality factor of 2. This is the current dominated by the recombination in the depletion region of a solar cell. The pre-factor of this term, I_{01}, is the diode saturation current, and it contains the information of minority lifetime in the depletion

region, as shown in equation (3.7)[21]. So, we can use the first exponential region to estimate the minority lifetime in the solar cell.

The second exponential term is dominated by the recombination in the neutral region, and give an ideality factor of 1. The saturation current in this region, expressed in equation (3.8) [14,21], also gives us information about the recombination rate.

$$I_{01} = \frac{qAn_i x'}{2\tau} \tag{3.7}$$

$$I_{02} = qA\left[\frac{D_n n_{p0}}{L_n} + \frac{D_p p_{n0}}{L_p}\right] \tag{3.8}$$

In the above two equations, n_i is the intrinsic carrier concentration; x' is effective width of depletion layer; τ is the SRH recombination lifetime in the depletion region; D_n and D_p are the diffusion coefficient of electrons and holes; L_n and L_p are the minority diffusion length of electrons and holes; n_{p0} and p_{n0} are the minority concentration in the neutral region.

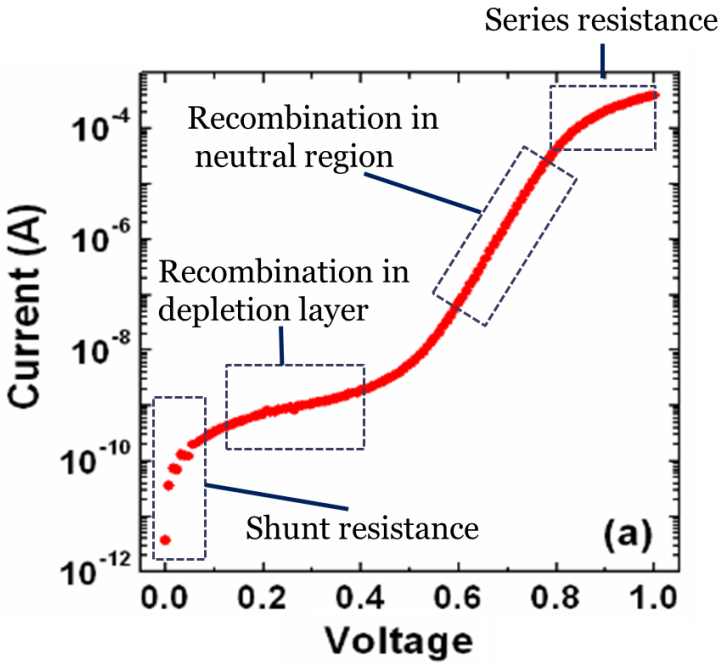

Figure 3.4: Dark IV curve can be used to give information about recombination process and resistance problem in a solar cell.

3.3 Quantum Efficiency

External Quantum efficiency (EQE) is a tool to diagnose the photon absorption and charge collection problems in solar cells. It is defined as the ratio of collected carriers to the number of incident photon at each wavelength:

$$\mathrm{EQE} = \frac{\#\ of\ collected\ carriers\ (\lambda)}{\#\ of\ incident\ photons\ (\lambda)} \tag{3.9}$$

EQE, or QE for short, is a quantity shows how efficiently photons are harvest by the solar cell at each wavelength. It gives us very important information on the location of carrier loss, and let us know in which place we should optimize the solar cell device.

Figure 3.5 shows the schematic of QE measurement setup we used in our lab. A white halogen bulb is used to generated photons with multiple wavelengths. Monochromator and optical filters are used in order to get photons with specific wavelength. By setting an appropriate incident angle, desired wavelength can pass through the monochromator after being diffracted on the slits. The optical filter is used to block the unwanted harmonics generated by higher orders of light diffraction in the monochromator. An optical chopper is used to convert the D.C light signal to A.C signal. Normally, a chopper with 13 Hz frequency is used to minimize the noise from the surrounding environment. Electrical signal from D.U.T. is collected and sent to the pre-amplifier. After that, a lock-in amplifier is used to reduce the noise by synchronizing the signal with the chopper. DC light bias and voltage bias can also be used if we want to do the measurement under different condition.

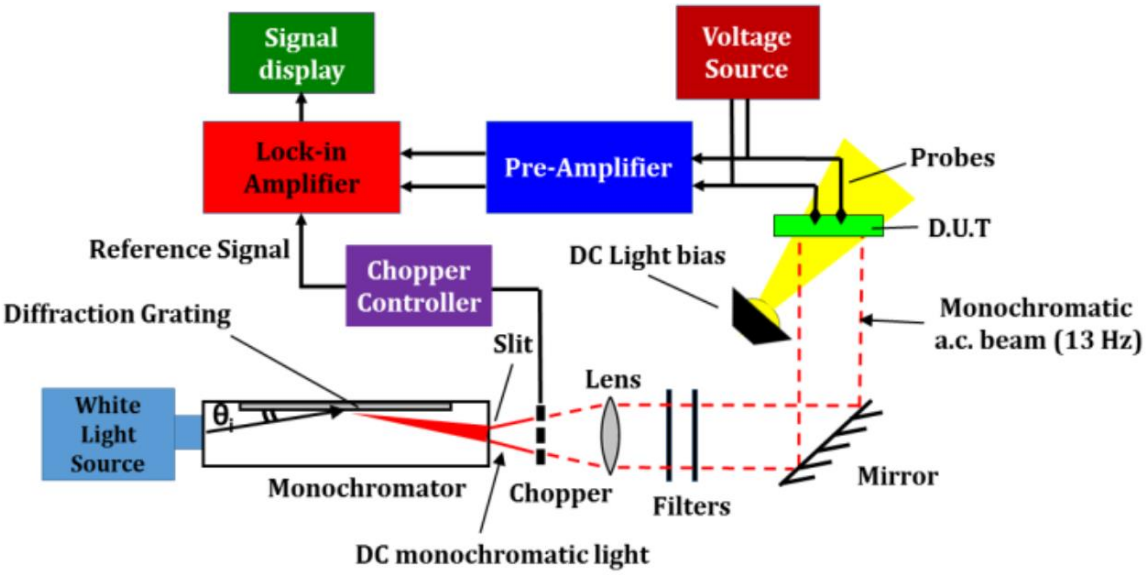

Figure 3.5: Schematic of QE measurement setup. D.U.T is the either a reference solar cell or a sample[22].

QE is one of the most important measurements in solar cell device characterization and diagnosis. Ideally, the QE signal should be 100%, which is the brown curve in Figure 3.6. However, in reality, solar cells will suffer from different kind of energy loss, such as absorption loss and recombination loss. A typical QE is depicted as the black curve in Figure 3.6. We can notice a significant signal reduction in the short wavelength region and long wavelength region. Signal loss in QE measurement can be due to many reasons, and therefore we should analyze the QE data based on the device structure and material properties of that solar cell. In Figure 3.6, the signal loss in the short wavelength region could be attributed to the parasitic absorption in the front layers or the front surface recombination. The signal loss in the long wavelength region could be because of insufficient main layer thickness and thus inadequate absorption. The overall reduction in QE signal could result from the reflection loss or low diffusion length in the main layer. Beyond a specific

wavelength, there will be no QE signal because of no absorption. That region can be used to determine the bandgap of the main layer material.

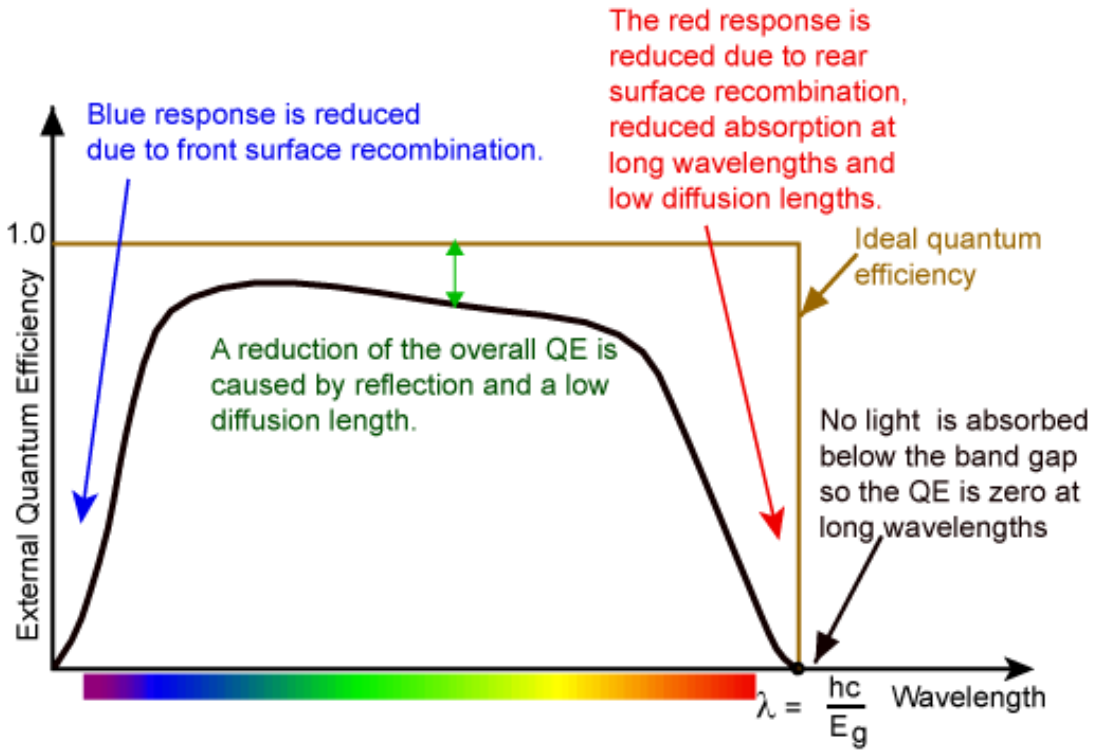

Figure 3.6: An ideal QE curve and a typical QE curve[23] .

With theoretical analysis on a finite solar cell with back surface recombination, the QE can be expressed in the following form[15]

$$QE = \frac{1}{1-\frac{1}{\alpha^2 L^2}}\left\{1-\frac{1}{\alpha L}\left[\frac{\frac{sL}{D}\left\{\cosh\left(\frac{t}{L}\right)-e^{-\alpha t}\right\}+\sinh\left(\frac{t}{L}\right)+\alpha L e^{-\alpha t}}{\frac{sL}{D}\sinh\left(\frac{t}{L}\right)+\cosh\left(\frac{t}{L}\right)}\right]\right\} \tag{3.10}$$

As we can see the equation (3.10), QE measurement can tell us a lot of information about the solar cell by fitting this equation to the measurement data, including the back-surface recombination velocity and diffusion length.

Equation (3.10) can also be simplified in some practical circumstances.

When the solar cell is illuminated by high energy photons which has high absorption coefficient in the solar cell.

In this case, $t \gg L, \alpha L \gg 1$. Equation (3.10) can be reduce as

$$QE = \frac{\alpha L}{1 + \alpha L} \tag{3.11}$$

If we plot QE vs. absorption coefficient α, we can calculate the diffusion length from the slope of the curve. There are also other methods to extract diffusion length form QE measurement, which will be discussed in the later chapter.

3.4 Sub-gap Quantum Efficiency

Sub-gap quantum efficiency (QE) is a method used to explore the mid-gap density of states distribution in a semiconductor. Figure 3.7 shows the density states distribution of a material with lattice disorder[24]. Tail states and mid-gaps states exist inside the bandgap where the former one follows an exponential distribution and the later one follows a Gaussian distribution. Since defects distribution is critical in analyzing the recombination in the device, knowing sub-gap density of state distribution will help us understand semiconductor device behavior.

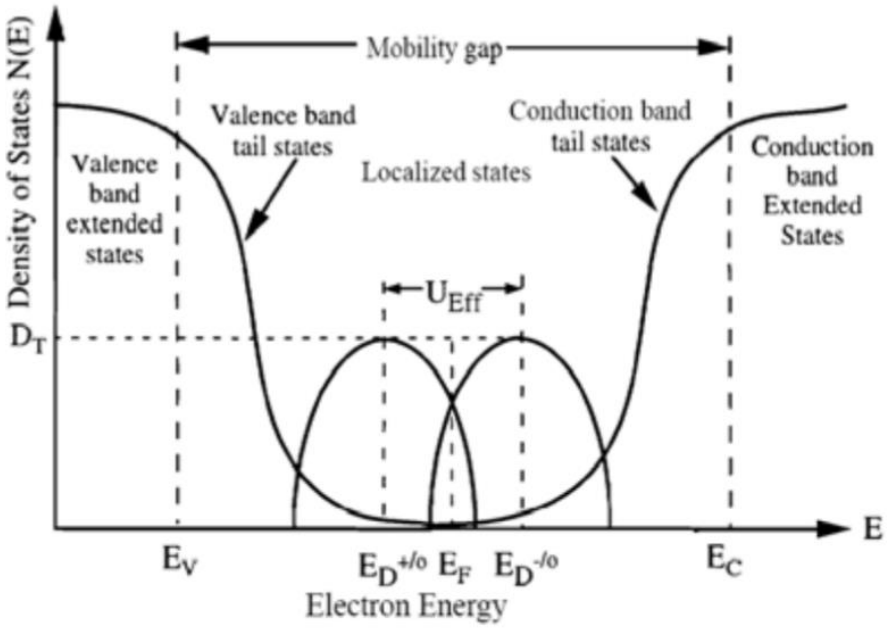

Figure 3.7: Density of states in a semiconductor with exponentially distributed tail states and Gaussian distributed mid-gap states[24].

Sub-gap QE measurement is done in a similar setup with QE measurement. A typical sub-gap QE curve of perovskite solar cell is shown in Figure 3.8. When the photon energy drops below the bandgap energy (1.6 eV), we see an exponential decrease in QE signal, which correspond to the absorption through tail states, as shown in Figure 3.9. This type of absorption follows Urbach's rule we discussed in Chapter 2.2. We can calculate the Urbach energy E_0 by taking the slope in this region. Urbach energy provides us an information of how much disorder exists in the material. The Urbach energy we get in perovskite is around 16 meV, which is much lower than that in organic polymers and a-Si (about 50 meV). This tells us that perovskite is much more crystalline when compared with organic materials. When the photon energy decreases even further (less than 1.5 eV), the states-transition mechanism will switch to mid-gap state transition, which is shown in Figure 3.9.

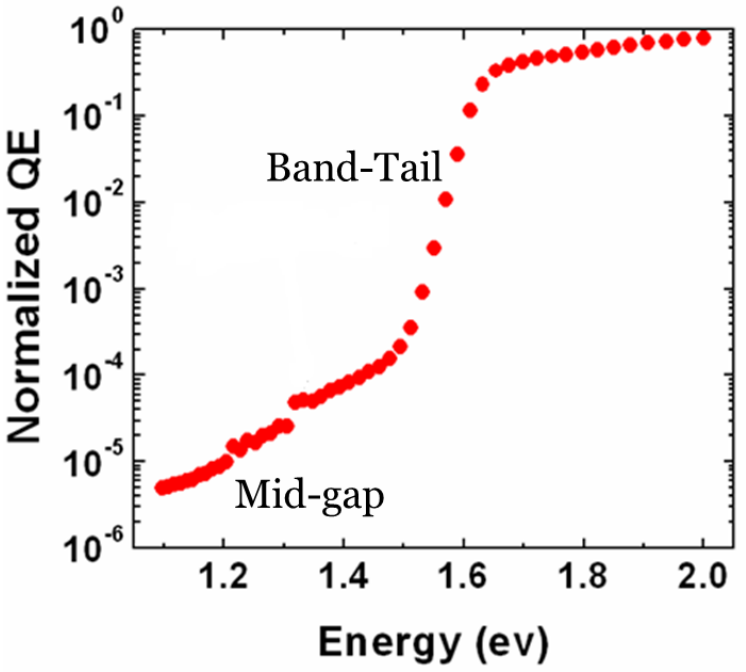

Figure 3.8: Sub-gap QE of perovskite solar cell.

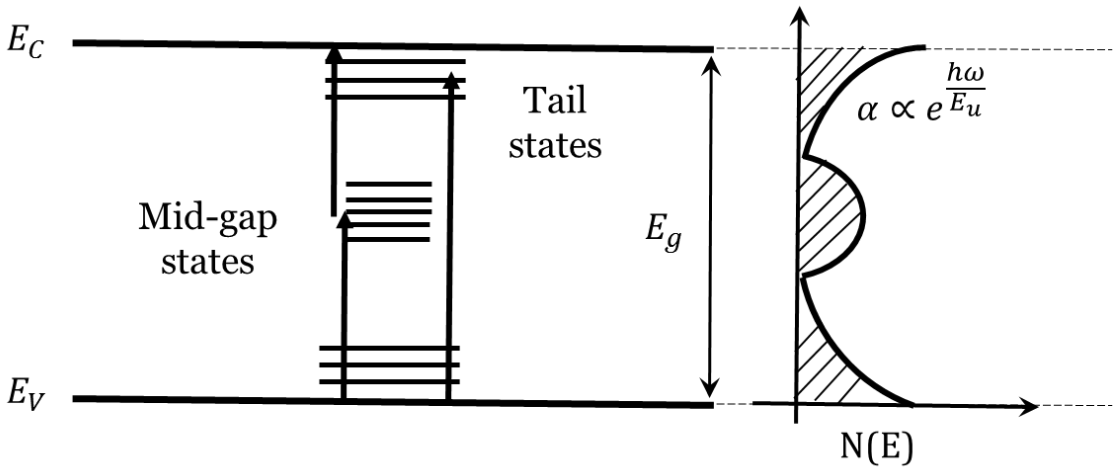

Figure 3.9: Sub-gap states transition: Transition through tail states and transition through mid-gap states.

3.5 Capacitance vs. Voltage

Capacitance vs. voltage (CV) is one of basic measurement for PN junction[14]. It can be used to measure the dopant density and depletion width of a PN junction.

The band diagram of PN junction is shown in Figure 3.10, where E_C is the conduction band; E_V is the valance band; E_F is the fermi level; E_T is the doping level, and Wd is the depletion width.

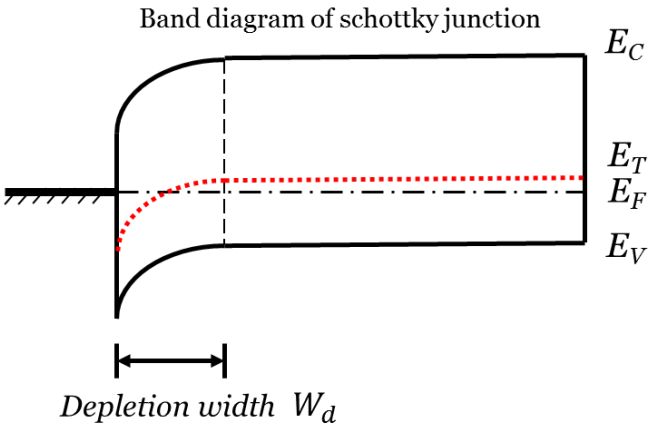

Figure 3.10: Band diagram of a PN junction with depletion width Wd.

The depletion capacitance of a PN junction can be expressed as

$$C = \frac{\epsilon}{W_d} = \sqrt{\frac{q\epsilon N_A}{2(V_0 - V)}} \tag{3.12}$$

Where ϵ is the dialectic constant of the material, N_A is the dopant density, and V_0 is the built-in voltage of the PN junction.

If we plot $\frac{1}{C^2}\ vs. V$, we should get a linear curve shown in Figure 3.11. The slope of the curve is proportional to $\frac{1}{N_A}$, and we can extract the dopant density from it. The intercept of curve with x-axis is where the built-in voltage is.

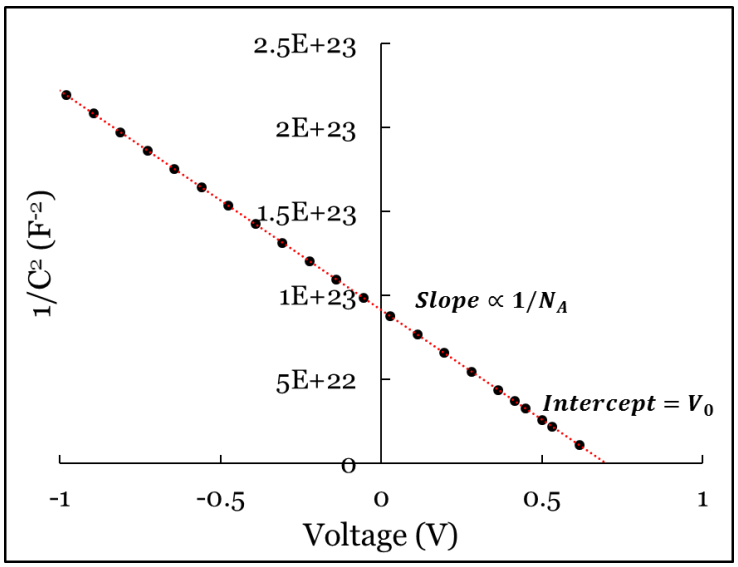

Figure 3.11: Ideal CV data of a PN junction with doping density of N_A and built-in voltage of V_o.

However, in reality, the slope of the curve would change in most cases. Figure 3.12 shows the CV data of nanocrystalline silicon (nc-Si) solar cell at different frequencies[25]. Clearly, in each set of data points, we can observe two linear regions with different slopes. This was explained by Kimerling[26] in 1974 that the slope at low bias is attributed to the density of shallow defects while the slop at high bias is due to the density of both shallow and deep defects. In this case, by scanning the voltage across both low bias and high bias region, we can calculate density of shallow defect and deep defect respectively.

At the same time, if we increase the AC signal frequency, deep defect cannot follow the drive voltage, and only shallow defects contribute to the overall capacitance. We can observe the decrease of capacitance with increasing frequency in Figure 3.12.

At very high frequency (100 kHz), the measured capacitance consists of only geometrical capacitance ($C_g = \frac{\epsilon A}{t}$) under reverse bias, where the PN junction is completely depleted. If we

know the dielectric constant ϵ and device area A, the geometrical capacitance we obtained in CV measurement can be used to calculate main layer thickness t.

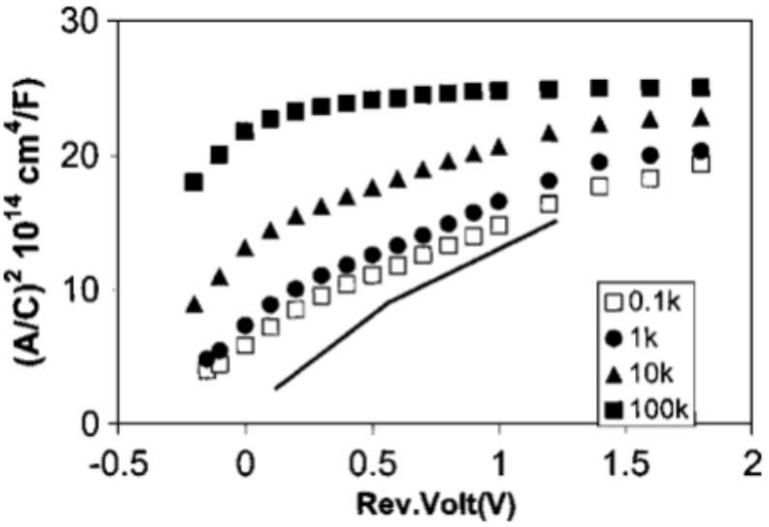

Figure 3.12: CV data of nc-Si solar cell at different frequencies[25].

3.6 Capacitance vs. Frequency and Temperature

Capacitance vs. frequency and temperature (CFT) is a powerful tool to measure the density state distribution, the attempt-to-scape frequency, traps activation energy, etc[27].

Before talking about CFT measurement, let us first introduce capacitance vs. frequency (CF) measurement.

In CF measurement, the capacitance of the sample is measured when we vary the AC signal frequency. This measurement will give us the density of state distribution within the bandgap of the semiconductor, which is an extremely important parameter we use to analyze the recombination process and photo-degradation mechanism of solar cells in the following chapters.

For a defect state located at E_T, the emission rate of electrons from the trap states to the conduction band follows the equation[13,28]

$$e_n = v_0 e^{-(E_c - E_T)/kT} \tag{3.13}$$

Where e_n is the emission rate of electrons, and v_0 is the attempt-to-escape-frequency (ATEF).

Equation (3.13) is the basic equation to understand capacitance spectroscopy. When the device is under an AC bias, the electrons on the traps states can follow the bias signal depending on where the traps states are and how fast the AC bias alters (AC frequency). According to equation (3.13), we can see that the emission rate of electrons will decrease in an exponential rate when the trap state goes deeper into the bandgap, which means deeper trap states have slower emission rate. Figure 3.13 shows how the traps states transition follows the external bias signal. If the emission rate of electrons is higher than the frequency of AC bias, the electrons in the traps can respond and charge and discharge with the external bias signal, which leads to an increase in the capacitance of the device. However, if the emission rate of electrons is low than the frequency of AC bias, they will not follow external bias and cannot contribute to the capacitance. In this case, the capacitance measured using CF method is only from the trap-state transitions that are fast enough to follow the bias signal.

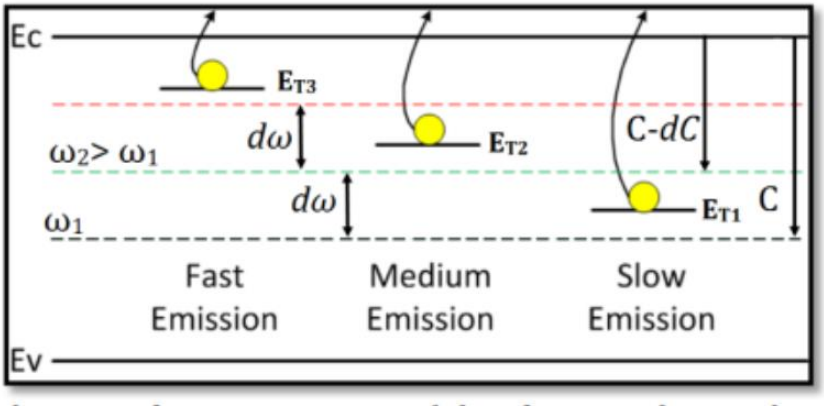

Figure 3.13: Shallow traps can follow high frequency external bias signal due to their fast emission rate while deep traps cannot[22].

Then, how do we determine the range of trap state levels that can respond to external bias, or how deep in the bandgap can we probe by using CF measurement?

The "probing depth" is determined by demarcation energy

$$E_\omega = \frac{kT}{q}\ln\left(\frac{\omega_0}{\omega}\right) \tag{3.14}$$

Where ω_0 is the angular ATET, which equals to $2\pi v_0$, ω is the angular frequency of applied AC bias.

So, only the trap states within the demarcation energy level can contribute to the capacitance in CF measurement. By lowing the "probe frequency" ω, we can increase the demarcation energy E_ω and detection range, which would increase the capacitance.

The density of states (DOS) is calculated by taking the derivative of capacitance to the frequency of applied bias.

$$N_T(E_\omega) = -\frac{V_{bi}}{qW}\frac{dC}{d\omega}\frac{\omega}{k_bT} \tag{3.15}$$

Here, V_{bi} is the built-in voltage of the device, W is the depletion width.

A typical CF curve and DOS distribution of perovskite solar cell are shown in Figure 3.14.

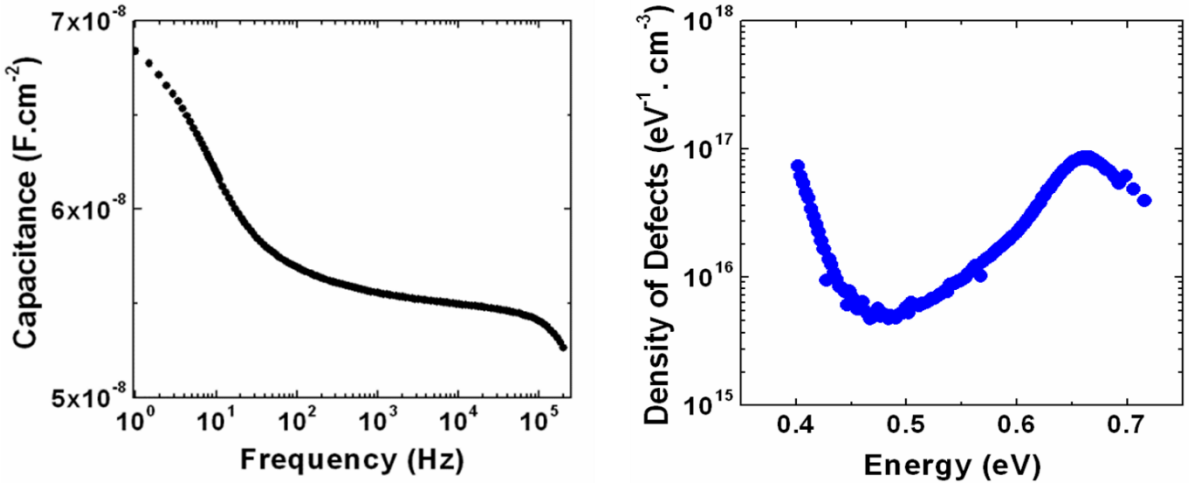

Figure 3.14: Capacitance vs. frequency curve of perovskite solar cell (left) and corresponding DOS distribution (right).

In order to calculate the DOS using CF measurement, there are two parameters, ATEF v_0 and trap level $E_c - E_T$, which are still unknown in equation (3.13).

Those two parameters can be obtained with the help of CFT measurement, which is basically a CF measurement under different temperature.

ATEF v_0 can be expressed as[29,30]

$$v_0 = N_c v_{th} \sigma_n \tag{3.16}$$

Where N_c is the effective density of states in the conduction band and σ_n is the capture cross section of the trap.

Since $N_c \propto T^{\frac{3}{2}}$ and thermal velocity $v_{th} \propto T^{1/2}$, the ATEF $v_0 \propto T^2$.

In this case, equation (3.13) can be modified as

$$\ln\left(\frac{e_n}{T^2}\right) = \ln(\xi) - \frac{E_A}{kT} \tag{3.17}$$

E_A is the activation energy of the trap states, which equals to $E_c - E_T$, and ξ is a constant.

If we plot $\ln\left(\frac{e_n}{T^2}\right)$ $vs.$ $\frac{1}{kT}$, we can get an Arrhenius plot from which we can calculate the activation energy and ATEF.

Figure 3.15 is the CFT data of a P3HT based organic solar cell[31]. As we can see, the capacitance increases with temperature due the increase of emission rate at high temperature. In the right figure, $f \times dC/df$ vs. f is plotted, and we can find the peak frequency f_{peak}, which corresponds to the emission rate.

In Figure 3.16, by fitting the $\ln(f_{peak}/T^2)$ vs. 1/T plot, we can calculate the activation energy by taking the slope of the curve, which is 210 meV. The intercept yields an ATEF of 10^9 Hz.

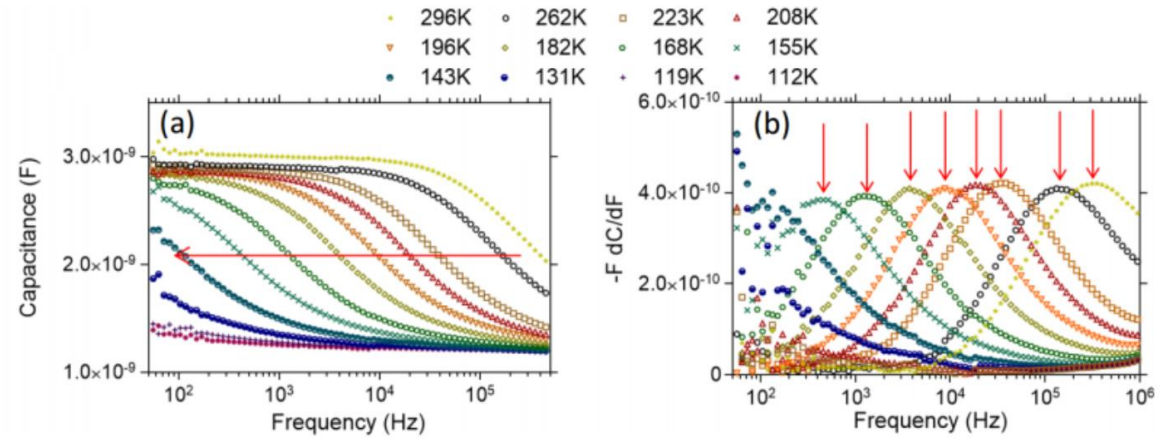

Figure 3.15: CFT data of P3HT based organic solar cells (left) and corresponding $f \times dC/df$ vs. f plot (right)[31].

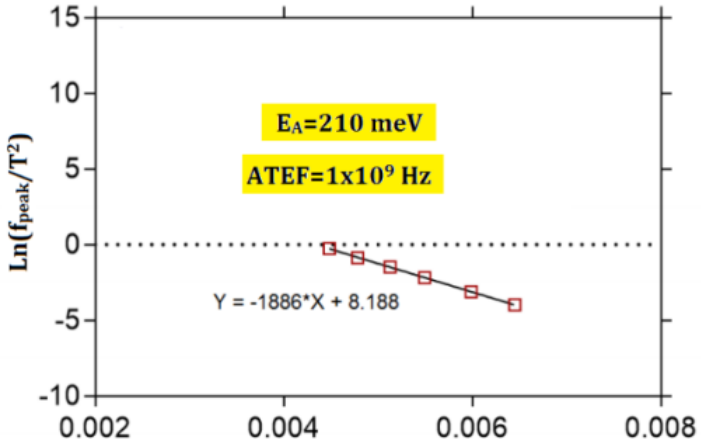

Figure 3.16: Arrhenius plot of $ln(f_{peak}/T^2)$ vs. 1/T. f_{peak} is the frequency where the DOS is the maximum. The slope gives an activation energy of 210 meV and the intercept yields an ATEF of 10^9 Hz[31].

3.7 Photo-conductivity Measurement

Photo-conductivity measurement can be used to calculate the μτ product of a material. μτ product has directly relation with diffusion length, which is one of the most important parameter for solar cell.

Photo-conductivity measurement is done by measuring the conductivity of the sample under dark and under light illumination.

In order to measure conductivity, we can deposit two metal bars with length L and width W on top the sample, as shown in Figure 3.17.

When the sample is placed in the dark, the conductivity we measure is called dark-conductivity, which can be expressed as follows.

$$\sigma_D = q\mu n \tag{3.18}$$

Photo-conductivity is measured when the sample is exposed to the light, and it can be written as

$$\sigma_L = q\mu(n + \Delta n) \tag{3.19}$$

In this case, we can calculate μτ product from the difference of dark and light conductivity.

$$\mu\tau = \frac{\Delta\sigma}{qG} = \frac{\sigma_L - \sigma_D}{\frac{qN_{abs}}{t}} \tag{3.20}$$

Here, G is the generation rate, t is the sample thickness, and N_{abs} is the number of absorbed photons in the sample, which can be calculated from the following equation.

$$N_{abs} = N_0(1 - R)e^{-\alpha t} \tag{3.21}$$

Where N_0 is the photon flux from the light source, R is the reflection of the sample, and α is the absorption coefficient.

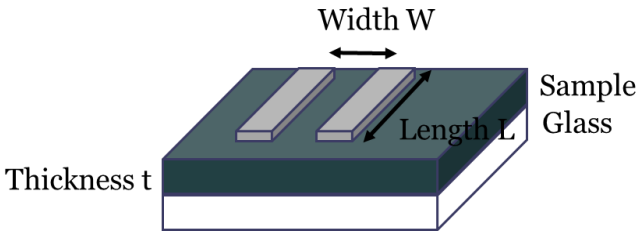

Figure 3.17: Schematic of sample structure for conductivity measurement.

CHAPTER 4

PEROVSKITE SOLAR CELLS

4.1 Introduction

As what we show in Chapter 1, the manufacture cost of silicon-based solar cells has been significantly reduced in the recent few decades. In order to make solar cell widely adopted, the price has to be decreased even further. However, currently, there is not too much room for price reduction for silicon solar cells. A new generation of photovoltaics is expected to replace the old types of solar cells. Perovskite solar cell is the one we are looking for, which offers both lower price and high energy conversion efficiency.

Perovskite or more specifically, lead-halide perovskite, is a semiconductor follows ABX_3 structure as shown in Figure 4.1[32]. In this structure, A and B are cations while X is halide. In order to form a perovskite structure, the ionic radii of A, B, and X have to follow the octahedral and tolerance factor rules[33], which is shown as follows.

$$\text{Tolerance factor: } 0.81 < \mathrm{t} = \frac{R_A + R_X}{\sqrt{2(R_B + R_X)}} < 1.11$$

$$\text{Octahedral factor: } 0.44 < \mu = \frac{R_B}{R_X} < 0.9$$

In the octahedral and tolerance factor range, the allowed material combinations are shown in Figure 4.2, where is MA is the short name of methylammonium ($CH_3NH_3^+$), and EA is ethylammonium ($CH_3CH_2NH_3^+$). Actual possible combinations are more than what are shown in Figure 4.2. The A cation in the structure could also be formamidinium (FA, $NH_2CH{=}NH_2^+$) and Cesium (Cs). The B cation could either be Lead (Pb) or Tin (Sn). X anion is halide (I, Cl, and Br). This great amount of combination offers perovskite excellent flexibility in material properties, which will be discussed in the following section.

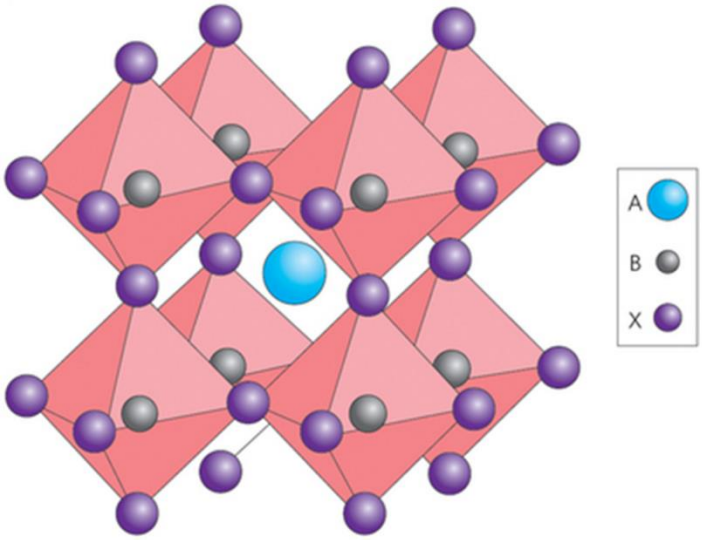

Figure 4.1: Lattice structure of perovskite. For lead-halide perovskite, A is normally organic cation, B is Lead or Tin, and X is halide[32].

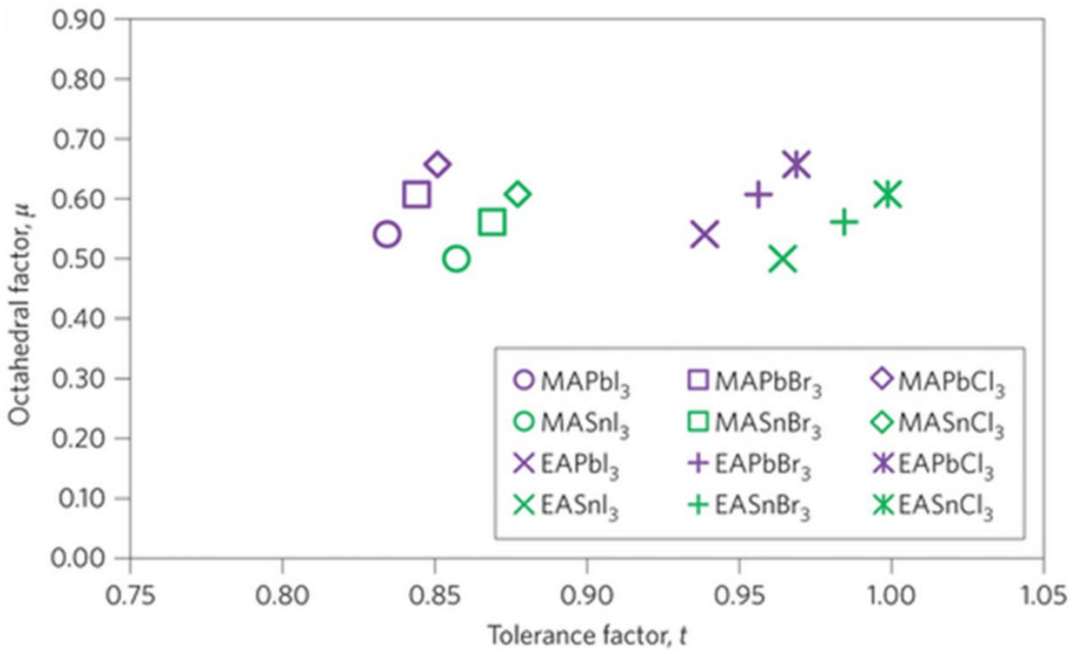

Figure 4.2: Materials combinations for lead-halide perovskite, which follow the allowed octahedral and tolerance factor region[32].

This type of organic-inorganic halide perovskite was discovered more than 100 years ago[34]. This material was first applied in the thin-film transistors and LEDs[35,36]. The first report on using perovskite as photovoltaic material was from Miyasaka's group[37,38]. In 2006, a 2.2% device was achieved by using $CH_3NH_3PbBr_3$ as the absorbing material[37]. After replacing Br with I, they were able to increase the efficiency to 3.8% in 2009[38]. Park and co-workers, by using TiO_2 as n-type layer, achieved and efficiency of 6.5% in 2011[39]. But at that time, they were using a liquid electrolyte which resulted in rapid device degradation. In 2012, Park and Grätzel introduced spiro-MeOTAD as the solid-state hole transport layer and improved the cell efficiency to 9.7%[40]. Later on , Seok's group boost the efficiency to 12.3% by using mix-halide perovskite[41]. Perovskite solar cell still did not attract too much attention in the research field until two important papers were published in middle 2013, both of which reported efficiency over 15%. The first one was from Grätzel's group[42]. They used mesoporous TiO_2 scaffold and introduced two-step solution process, which greatly improved the perovskite morphology. The second one was from Snaith's group. Instead of using solution process, they were the first group to use vapor deposition to grow perovskite[43]. After the Materials Research Society (MRS) meeting in 2013 Fall, great number of research groups joined the research of perovskite solar cells and significantly boosted the speed of efficiency improvement. The efficiency record was refreshed frequently from groups to groups, and now 20+% efficiency has been achieved by several groups[44,45].

Understanding the material property of perovskite is the first step for device physics, device optimization, and device degradation study of perovskite solar cell. In this Chapter, I will talk about our research progress on the study of perovskite material properties and formation mechanism.

4.2 Fabrication Process

4.2.1 Fabrication methods and device structure

One of the advantages of perovskite is that it can be made by lots of methods. Generally, those methods can be divided into two categories, solution process or vapor process, which are shown in Figure 4.3. In solution process, the perovskite raw materials are dissolved in an organic solvent (Mostly DMF). Solution process can be done in multiple ways, such as one-step solution process[46], two-step solution process[47], anti-solvent solution process[48,49,50], vacuum flash–assisted solution process[51], etc. The easiest one is one-step solution process, in which the perovskite solution is spun coated on the substrate and followed by an annealing process. In vapor process[43,52,53,54,55,56], the organic compound (usually MAI) and inorganic compound (usually PbI_2) are co-evaporated, and perovskite is formed on a heated substrate. Perovskite can also be made using hybrid process[57], which is simply a combination of solution process and vapor process.

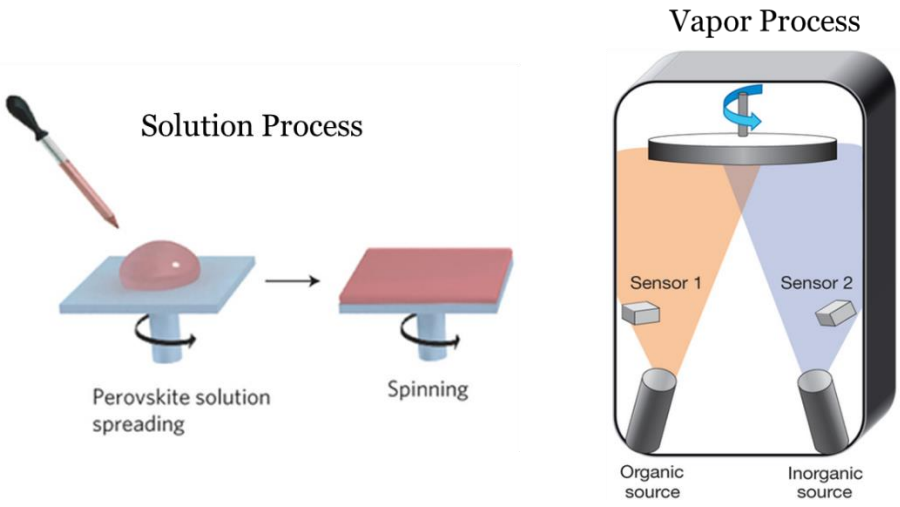

Figure 4.3: Perovskite fabrication method. It can be made by either solution process (left) or vapor process (right)[43,58].

The most popular form of perovskite is $CH_3NH_3PbI_3$. It can be formed using the chemical reaction function below.

$$PbI_2 + CH_3NH_3I \rightarrow CH_3NH_3PbI_3$$

However, some groups also reported that they can make perovskite with non-iodine lead salt[43,46,59], the reaction mechanism will be discussed later.

Perovskite solar cells can be made using either PIN or NIP structure, as shown in Figure 4.4. There is a great quantity of materials we can use for p-type layer and n-type layer. The choices for p-type layer could be PEDOT:PSS, NiO, P3HT, Poly-TPD, PTAA, etc. The options for n-type layer could be TiO_2, ZnO, PCBM, CdS, etc.

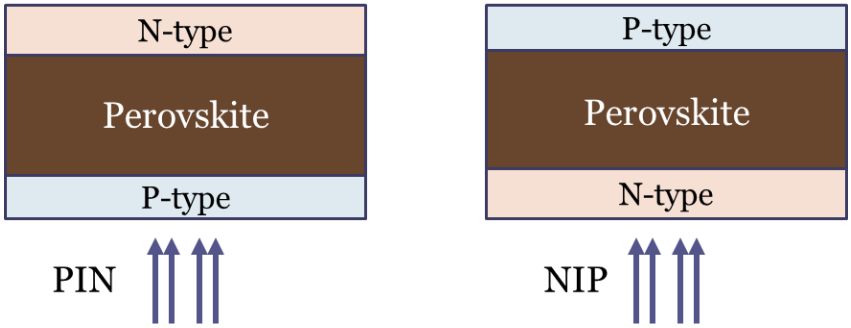

Figure 4.4: Device structure of perovskite solar cells. It can be made as PIN structure (left) or NIP structure (right).

The device structure of PIN and NIP device used in our lab is shown in Figure 4.5. The PIN structure uses PEDOT:PSS as p-type layer, and PCBM as n-type layer. In the NIP device, we use TiO_2 as the n-type layer and P3HT as the p-type layer.

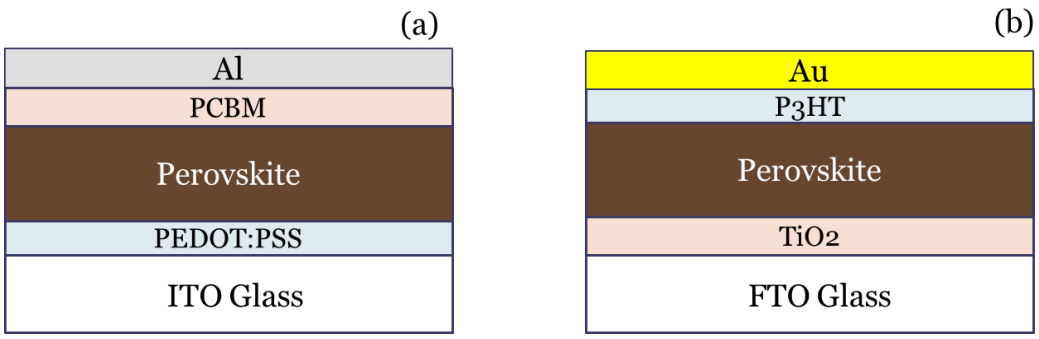

Figure 4.5: Typical device structure for PIN and NIP device.

Here are some basic process steps we use to make our PIN devices.

First, the ITO coated the glass is cleaned by sonication in surfactant, DI water, methanol, and acetone. The surfactant step takes 15 minutes, and rest of cleaning step takes 5 minutes each.

After that, we deposit p-type layer on top of ITO. In our lab, we either use PEDOT:PSS or NiO. The difference of them will be discussed later.

If we use PEDOT:PSS, the ITO substrate will be cleaned in air-plasma for 10 minutes. Then, PEDOT:PSS solution will be spin-coated on top of it at 4000 rpm, and followed by 150℃/20min thermal annealing in air.

If NiO is used as p-type layer, the ITO substrate will be loaded into an e-beam evaporator. A 30 nm thick NiO layer will be evaporated at deposition rate of 0.5Å/s. The NiO layer will then be annealed at 200℃ for 1 hour in air.

After that, the substrate will be transferred into a N_2 filled glovebox. The O_2 and H_2O level in glovebox are always maintained at less than 1ppm.

The perovskite process recipe we use in this research mostly comes from Park's group[48]. The perovskite solution is made by mix 1.67 M lead ioide (PbI_2), 1.67 M methyl-ammonium iodide (MAI), 1.67 M Dimethyl sulfoxide (DMSO) in Dimethylformamide (DMF). The solution is stirred on a room-temperature hot-plate for more than 3 hours before using.

We spin coat the perovskite solution at 4000rpm. Then, after a specific delay (normally around 10s), we pour chlorobenzene onto the film. Chlorobenzene here is used to immediately saturate the perovskite solution and results in a fast perovskite film crystallization. Perovskite film is then annealed at 60 ℃ for 1 minute and 100 ℃ for 5 minutes.

After that, 20 mg/ml PCBM in chlorobenzene is spin-coated on perovskite at 2000 rpm. And the film is then annealed at 75 ℃ for 15 minutes.

Finally, 100 nm of aluminum is thermally evaporated on top of the film at a deposition rate of 2-4 Å/s.

For PIN device structure, PEDOT:PSS is a great hole transport layer. But, unfortunately, it is not a good electron blocking layer for perovskite. A better choice is NiO. The conduction band of NiO is around -2 eV and the valence band is around -5 eV, which makes it a great electron blocking layer as well as a hole transport layer. The band diagram of perovskite solar cell with NiO as p-type layer is shown in Figure 4.6 (a). Figure 4.6 (b) shows that the efficiency of perovskite solar cell increased from 10.2% to 14.2% with the application of NiO layer, which enhanced the Voc from 0.8 V to 1 V.

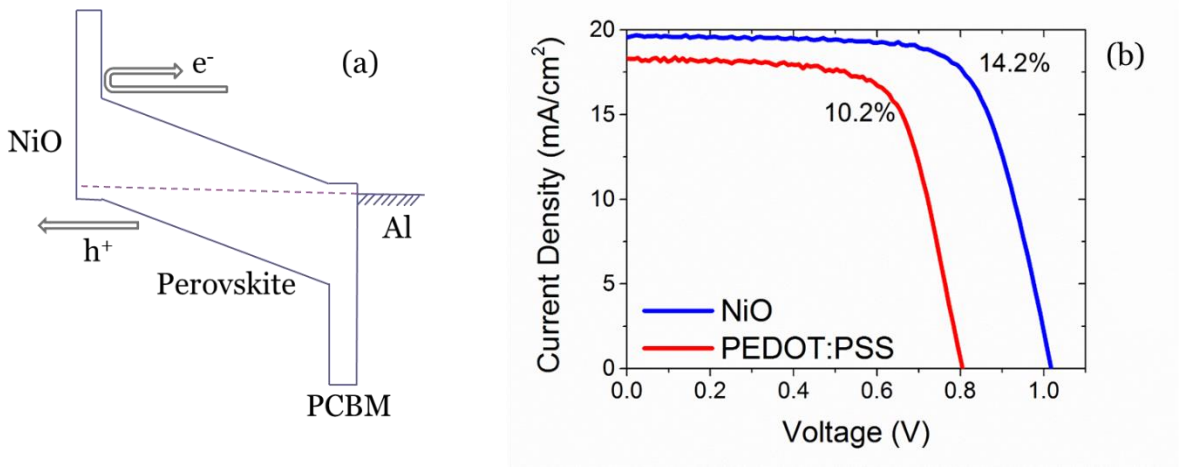

Figure 4.6: (a) Band diagram of perovskite solar cells with NiO as p-type layer. (b) IV curves of the devices using PEDOT:PSS or NiO as p-type layer. The one with NiO has much higher Voc (1 V) than the PEDOT:PSS device (0.8 V).

4.2.2 Formation mechanism

In the early stage of our perovskite research, we used the recipe from Yangyang's group[46] to grow perovskite. The perovskite precursor used in this recipe is made by mixing 212 mg of MAI and 122 mg of lead chloride ($PbCl_2$) in 1 ml DMF. Since the halide in the precursor includes both iodine and chlorine, we are not sure whether the final perovskite we get is $CH_3NH_3PbI_3$ or $CH_3NH_3PbCl_3$ or a mixture of the two.

In order to know the material composition and formation mechanism of perovskite, we use X-ray diffraction (XRD) to monitor the structure change during the material formation. Besides, $PbCl_2$, $Pb(SCN)_2$ and $Pb(NO_3)_2$ are also used in this study.

Three samples coated with $PbCl_2$, $Pb(SCN)_2$ and $Pb(NO_3)_2$ are exposed to MAI to form perovskite. Figure 4.7 (a) represents the XRD of different lead salts prior to perovskite formation. It is worthy to highlight that the lead iodide (PbI_2) showed an intense (011) peak at the 2θ values of 12.7° where as other lead salts ($PbCl_2$, $Pb(SCN)_2$ and $Pb(NO_3)_2$) do not show any peak in that region. Figure 4.7 (c) corresponds to XRD of black perovskite films. XRD peaks for perovskite formed from PbI_2 and $PbCl_2$ match perfectly with each other. Interestingly, even the peaks of perovskite formed from $Pb(SCN)_2$ and $Pb(NO_3)_2$ match with the peaks of $CH_3NH_3PbI_3$. This suggests that irrespective of lead salt used, same perovskite is formed in the end. Figure 4.7(b) represents the XRD of yellow intermediate where, for lead thiocyanate and lead nitrate along with original lead salt peak, a new peak appeared at 2θ value of 12.7°. This peak matches perfectly with the XRD peak of PbI_2 suggesting that the SCN^- and NO_3^- ions were exchanged with I^- (from MAI) resulting in the conversation of lead salt ($Pb(SCN)_2$ and $Pb(NO_3)_2$) to PbI_2. In this case, the whole picture of perovskite formation mechanism is

clear. For those non-iodine lead salt, its anion will be exchanged with I^- during the formation, and finally turns into $CH_3NH_3PbI_3$.

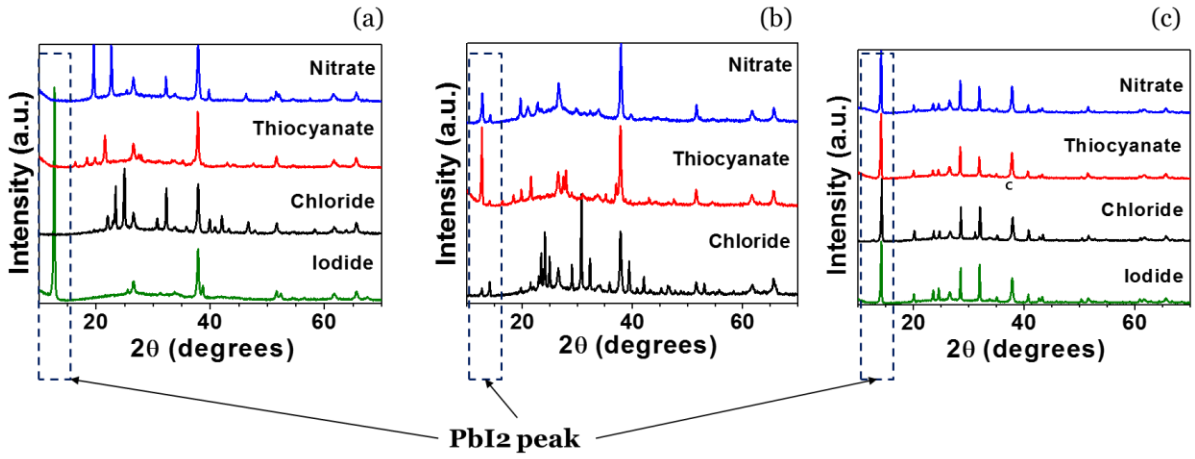

Figure 4.7: XRD images of the perovskite. (a) XRD of the film before perovskite formation (b)XRD of the film during perovskite formation (c) XRD of perovskite after formation.

4.2.3 Solvent annealing

The anti-solvent solution process provides a way to make highly uniform and smooth perovskite film with high quality. However, the perovskite formation process is too fast (<1 minute) and results in small grains (~200 nm). Small grains in perovskite provides lots of grain boundaries, which lead to huge increase in recombination rate.

In order to make perovskite films with larger grains, solvent annealing process was proposed by Huang's group[60]. Solvent such as DMF, which can dissolve perovskite, was use in this process. Later, DMSO was also applied in this process[61].

Figure 4.8 shows how solvent annealing process works. In solvent annealing process, the pristine perovskite film and DMSO solvent are placed on the same hot plate, covered by a glass petri-dish. DMSO solvent turns into DMSO vapor after being heated. Since DMSO can dissolve perovskite, DMSO vapor will gradually penetrate the perovskite film and make it

between liquid and solid phase. During the annealing process, the DMSO in the perovskite will slowly go away, leading to the recrystallization of perovskite. This slow film regrowth is the reason we can observe larger grain afterwards.

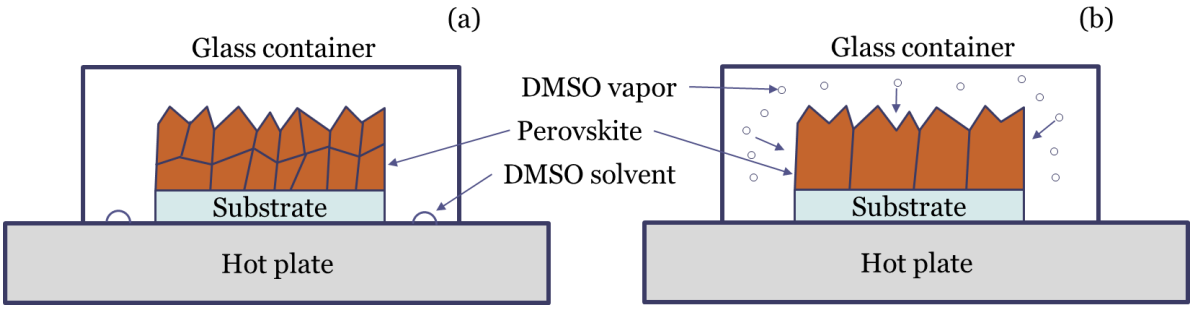

Figure 4.8: Schematic of solvent annealing process: (a) Pristine perovskite film and DMSO solvent are placed on top of a hot-plate, covered by a glass petri-dish (b) DMSO solvent turns into vapor and dissolves the gran boundary of perovskite and leads to perovskite recrystallization.

The SEM image of perovskite film is shown in Figure 4.9. The grain size of perovskite is around 200 nm before solvent annealing. After solvent annealing process, it increased significantly to around 1µm.

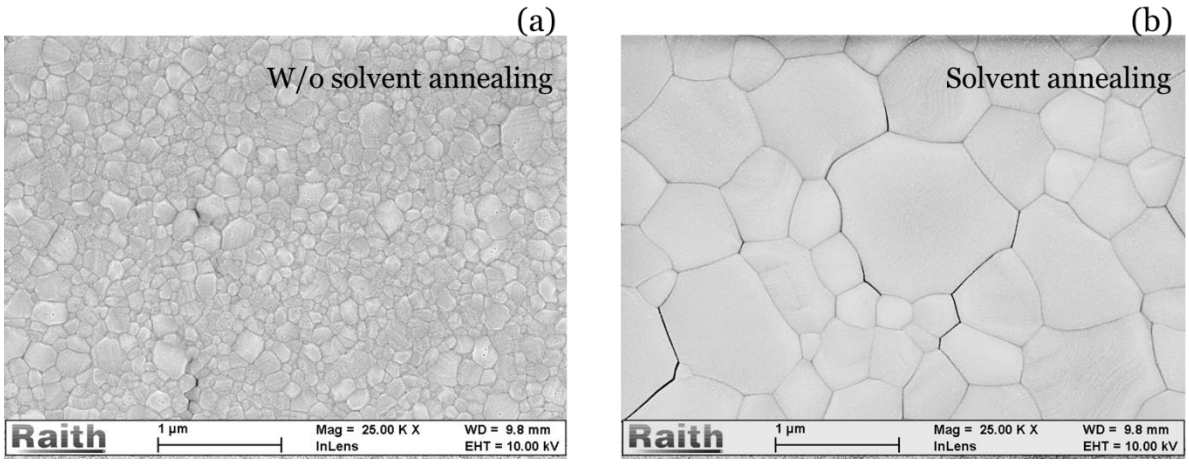

Figure 4.9: SEM of perovskite film: (a) Before solvent annealing (b) After solvent annealing.

Perovskite solar cells with and without solvent annealing process are made in our lab. The IV and QE curves are shown in Figure 4.10. With the help of solvent annealing, we greatly improve the device performance, from 6.4% to 10.2%. The detailed performance of those two devices are presented in Table 4-1. Most of the improvement comes from the increase of current, which has an increment of 38%. The QE curve in Figure 4.10 (b) clearly shows an increase all over the wavelength, which indicates a significant improvement in diffusion length benefited from larger grain size.

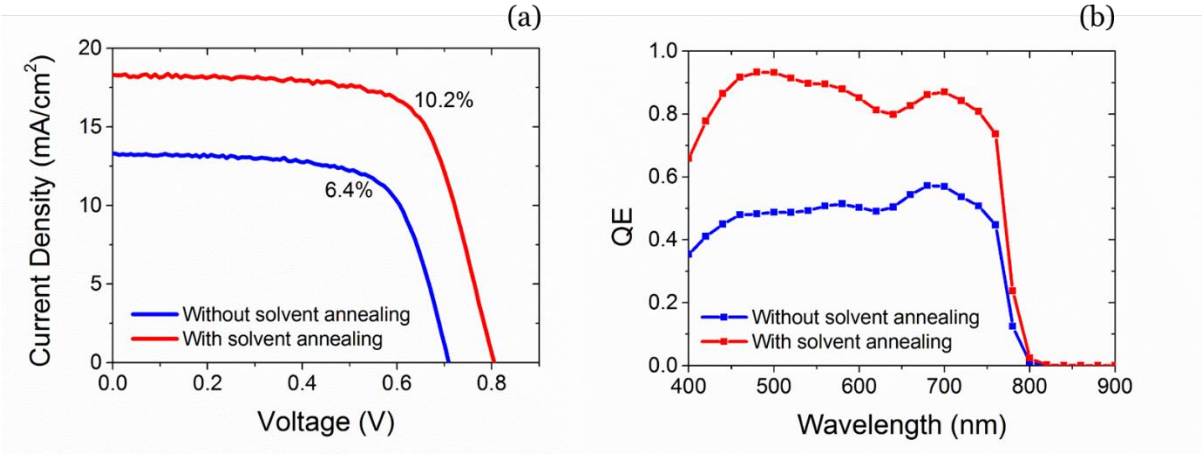

Figure 4.10: (a) IV of devices with and without solvent annealing process (b) QE of devices with and without solvent annealing process.

Table 4-1: Performance comparison of perovskite solar cells with and without solvent annealing (SA) process.

	Voc	Jsc	FF	PCE
No SA	0.71 V	13.3 mA/cm^2	68%	6.4%
SA	0.81 V	18.3 mA/cm^2	69%	10.2%
Increment	+14%	+38%	+0%	+60%

4.3 Material Property

The success we achieved in perovskite solar cell originates from its great materials properties. In this part, we will investigate some important material properties of perovskite.

4.3.1 Bandgap

Bandgap is one of most basic material properties. As we have discussed in Chapter 2.5, the maximum efficiency a solar cell can achieved directly depends on its bandgap.

Perovskite is found to be a direct bandgap material. From equation (2.1), if we plot $\alpha^2\ vs.\ hv$, we should get a linear curve whose intercept with x-axis lies on the bandgap energy of the material. Moreover, instead of measuring absorption coefficient, we can simply use the QE data to extract the bandgap of perovskite.

When the photon energy is close to the bandgap energy where the absorption coefficient is low, the QE expression can be reduced as

$$QE = c * \alpha * t \tag{4.1}$$

Where c is a constant, t is the thickness of the film, which is also a constant.

In this case, we can also plot $QE^2\ vs.\ hv$ to calculate bandgap energy. Figure 4.11 shows a plot of $QE^2\ vs.\ hv$. By fitting the points around bandgap with a linear curve, we extracted the bandgap of perovskite, which is around 1.58 eV.

Although the bandgap is not around the optimum value, which is 1.34 eV, we can still achieve a maximum efficiency of 31% with a bandgap of 1.58 eV.

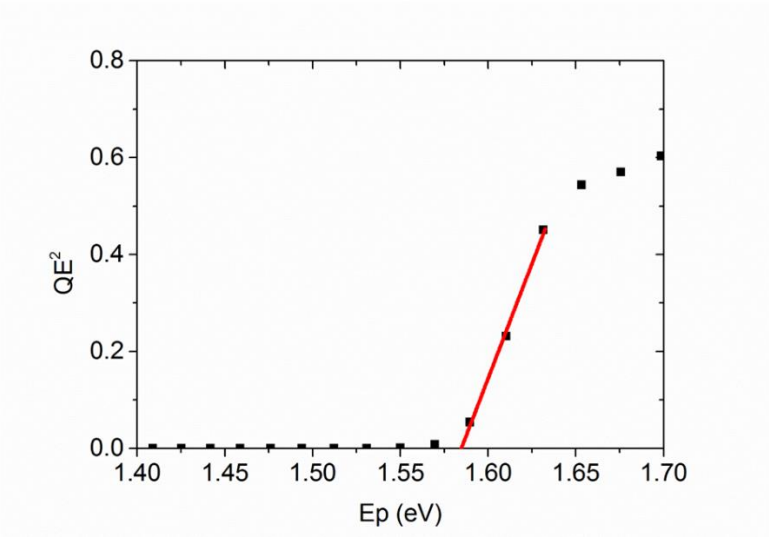

Figure 4.11: QE^2 vs. photon energy: The intercept on x-axis represents the bandgap energy of perovskite.

4.3.2 Doping type

The dopant type determines what the minority carrier is in a semiconductor. Since solar cells are controlled by minority carrier, knowing what the dopant type is critical for the future device design and optimization.

The determination of doping type can be done in many ways, such as Hall effect and hot-probe measurement. Here, we proposed an easier way. As shown in Figure 4.12 (a), the perovskite layer is sandwiched by two p-type layer, P3HT and NiO. The valance band of P3HT and NiO perfectly matches that of perovskite. However, there is a huge barrier between the conduction band of those materials, which makes it a hole-only device. The dark IV of this device is presented in Figure 4.12 (b). The IV curves are symmetric in the first and third quadrant. In both quadrant, the dark current I is proportional to V^2, which indicates a space-charge-limited current. In this case, the perovskite layer should be lightly p-typed doped. If it

is n-type doped, we should expect an exponential relation between current and voltage, which does not exist here.

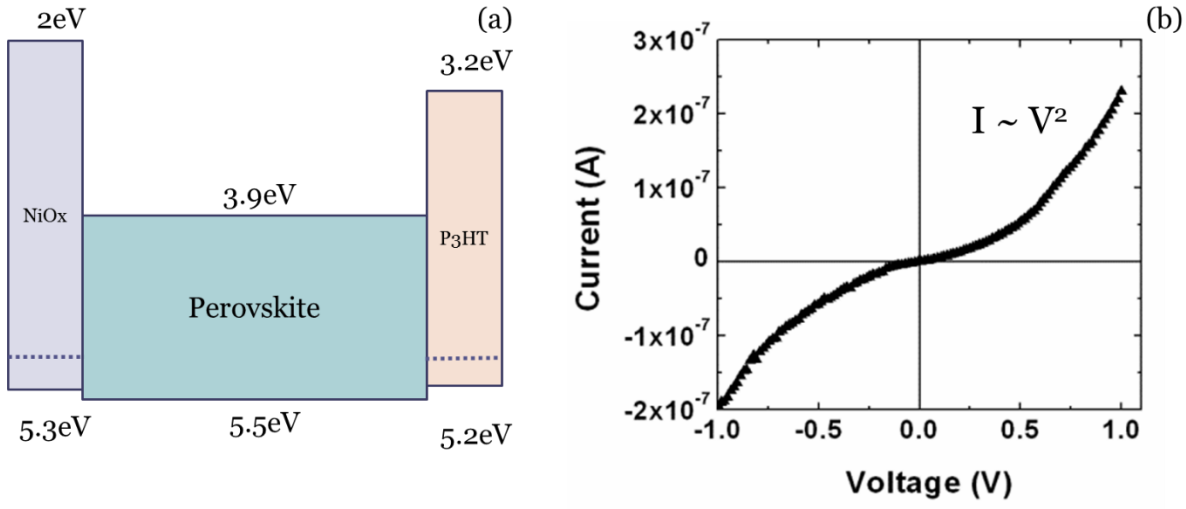

Figure 4.12: (a) Band diagram of a p-perovskite-p structure. (b) The dark current of this device follows space-charge-limited-current rule.

4.3.3 Sub-gap defects density

The sub-gap QE of perovskite solar cell is depicted in Figure 4.13. It shows the presence of tail state with an Urbach energy of 15 meV. This is much lower when compared with the Urbach energy of a-Si and organic materials, which is around 50 meV. Lower Urbach energy indicates better crystallinity for perovskite. When the photon energy goes down below 1.5 eV, we observe the state transition through mid-gap states.

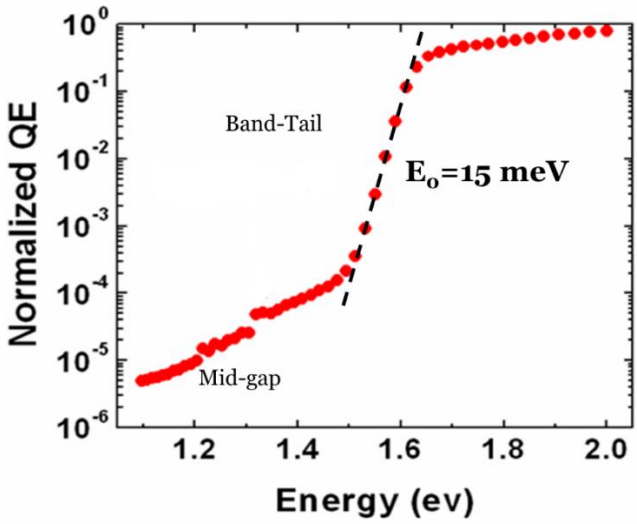

Figure 4.13: Sub-gap QE of perovskite. The Urbach energy of tail states is around 15 meV, which indicates high crystallinity of perovskite film.

In order to obtain more information of the electronics defect within the bandgap, we did CFT measurement on our perovskite sample[62]. Figure 4.14 is plot of CFT data with y-axis as $(-f\times dC/df)$ and x-axis as the frequency of applied AC bias. The capacitance vs. frequency was measured under different temperatures varied from 175K to 344K. Two peaks are observed at those temperatures; one is found in low frequency range and the other in high frequency range, which correspond to the deep defects and shallow defects in perovskite respectively. As the temperature goes up, the emission rate of the traps will increase and lead to higher peak frequencies. If we plot them in an Arrhenius diagram described in Chapter 3.6, we can obtain the level of shallow and deep defects. The activation energy of shallow defects is 0.24 eV while that of deep defects is 0.66 eV. At the same time, we also determined the attempt-to escape-frequency of perovskite, which is around 2E11 Hz at room temperature.

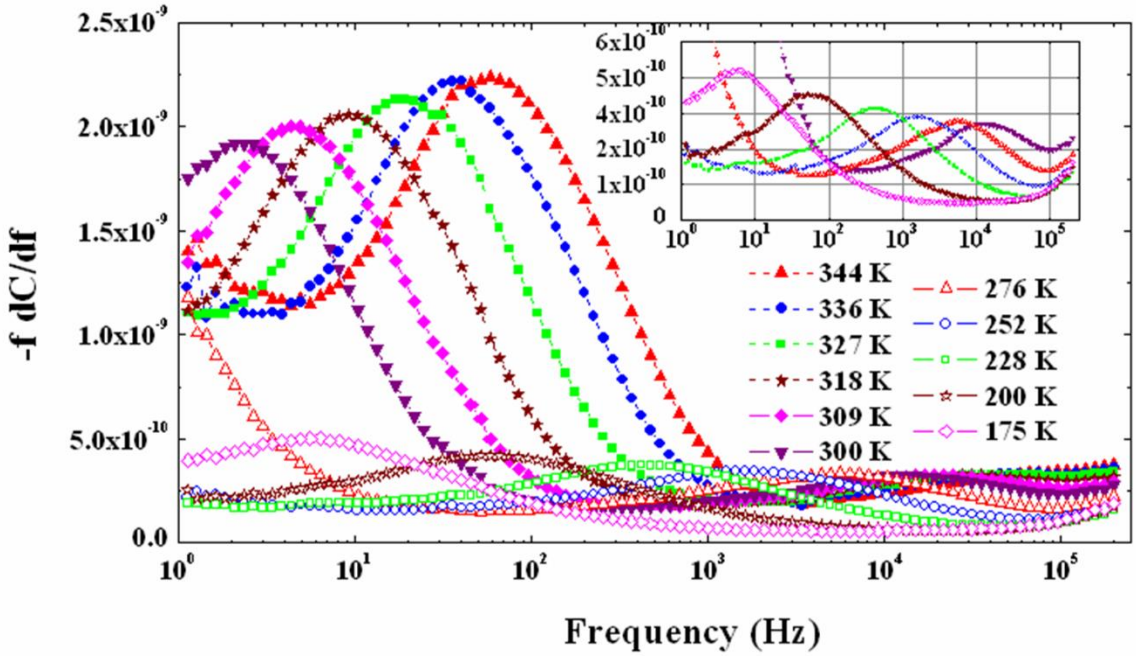

Figure 4.14: CFT data of perovskite solar cell. The inset is the magnified part of shallow defect band. The peak of the curve shifts to higher frequency when the temperature goes up, which indicates higher emission rate.

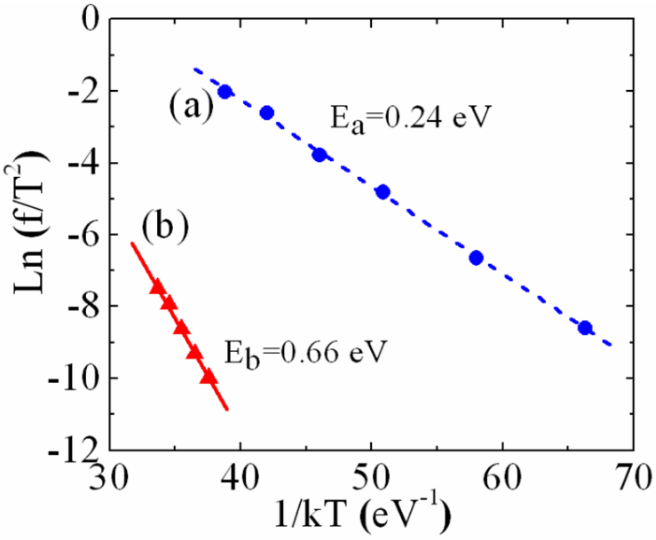

Figure 4.15: Arrhenius plot of CFT data. Two defect levels are observed. (a) a shallow defect level at 0.24 eV (b) a deep defect level at 0.66 eV.

Then, the capacitance spectroscopy is applied to evaluate the density of states distribution in the perovskite, and the result is shown in Figure 4.16 (a). The DOS curve has a mid-gap states peak at 0.66 eV. If we focus on the mid-gap state region, the DOS distribution can be fitted by a Gaussian distribution in Figure 4.16 (b).

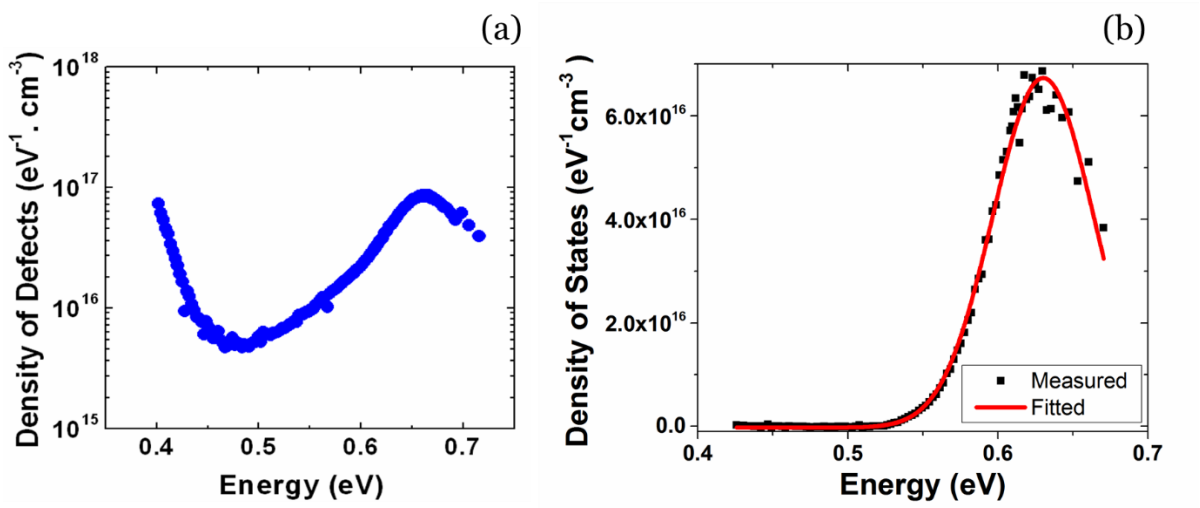

Figure 4.16: (a) Density of states distribution inside perovskite. (b) The DOS distribution of mid-gap states fitted by Gaussian distribution.

The dark IV of our perovskite solar cell is depicted in Figure 4.17 (a). In the low bias region, the current is dominated by the shunt current, following a quadratic relation with the applied voltage. When the applied voltage goes higher, the current follows the two-diode model, which is shown in Figure 4.17 (b). The dark current is perfectly fitted by this model between 0.3 V to 0.8 V. The fitted curve give an ideality factor of 2 in the low bias region, which indicates the recombination in the depletion region. The ideality factor of the fitted curve in the high bias region (0.6-0.8 V) is 1. That corresponds to the recombination in the neutral region. When the voltage is over 0.8 V, the current is then limited by the series resistance.

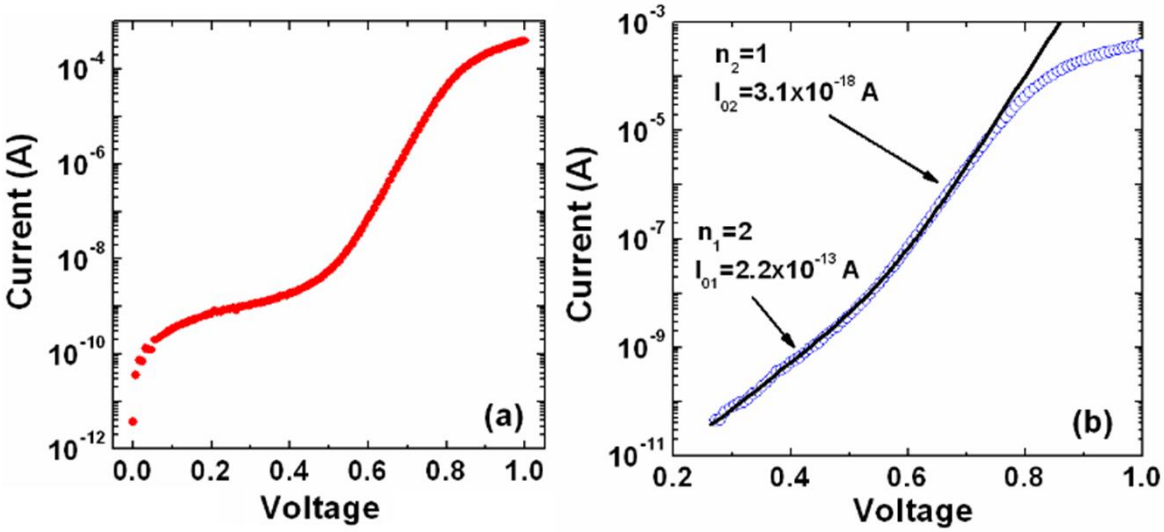

Figure 4.17: (a) Dark IV of perovskite solar cell at room temperature (b) Dark IV (shunt current subtracted) fitted by two-diode model.

4.3.4 Diffusion length

Diffusion length can be measure using many approaches. Here, we presented measured diffusion length using photo-conductivity. As we discussed in Chapter 3.7, photo-conductivity can be used to extract the μτ product of a solar cell, where μ is the mobility of majority carriers and τ is the lifetime of minority carriers. Unfortunately, the mobility of minority carriers is not provided by using this method, which is essential for diffusion length calculation. However, Snaith and co-workers showed that the mobility of electrons and holes is almost the same in perovskite[63]. In this case, the μτ product we obtained using photo-conductivity measurement can be directly used to calculate diffusion length.

Figure 4.18 (a) shows the IV curve of dark conductivity and photo-conductivity measurement. The inset of Figure 4.18 (a) show the two curves plotted in log scale. The calculated diffusion length is plotted vs. generation rate in Figure 4.18 (b). The diffusion length we get using 800nm light illumination is between 7-13 μm. This diffusion length decrease

dramatically when the generation rate increases. The diffusion length calculated is around 4 μm, which matches the what we get from QE vs. bias measurement in the next Chapter.

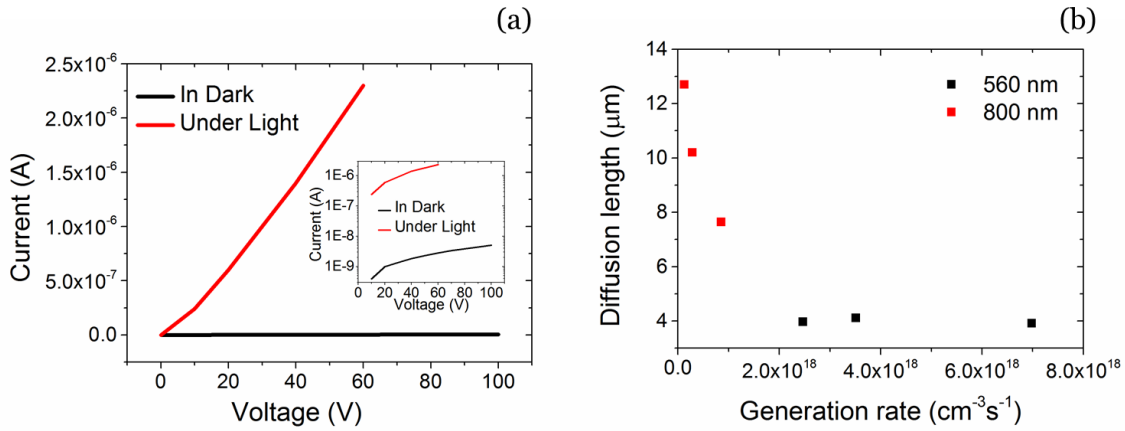

Figure 4.18: (a) Dark conductivity and photo-conductivity measurement data. (b) Diffusion length vs. generation rate at different wavelength.

4.3.5 Problems and Disadvantages

Apart from the great advantages of perovskite, such as high absorption coefficient, high dielectric constant, and high diffusion length, it also suffers from several problems.

The first problem is that perovskite contains lead currently, which is an environment hazard. Currently, lots of research groups are working on making perovskite with non-lead compound[64,65,66].

The second problem is the stability issue. Perovskite has very poor thermal stability and environment stability[67,68,69], which limit its application in real-life photovoltaics.

The mostly used perovskite, $CH_3NH_3PbI_3$, can be easily degraded when being heated at over 100 ℃, as shown in Figure 4.19 (a). The thermal stability can be significantly improved by replacing MA with FA in perovskite structure. After being heated at 150 ℃ for 1 hour, no color change in perovskite film was observed[70].

When the perovskite is exposed to humid environment, it will decompose even at room temperature. Figure 4.19 (b) shows how perovskite film changes when being exposed to moisture in the air and immersed in water[71]. The environmental stability can be significantly improved by encapsulation techniques, which protects perovskite from moisture attacking. An intrinsic encapsulation technique is proposed by our group, which will be discussed in next chapter.

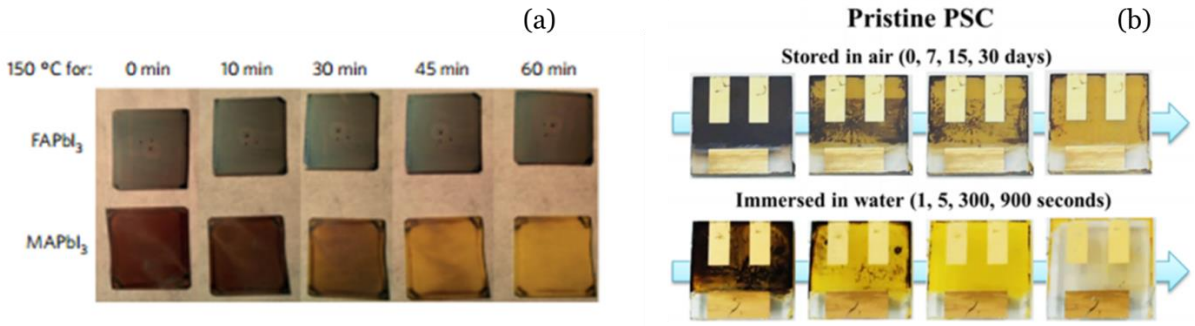

Figure 4.19: (a) $MAPbI_3$ degrades quickly after being heated at 150 ℃ while $FAPbI_3$ shows great thermal stabilty[70]. (b) Perovskite can easily decompose under humid enrionment[71].

CHAPTER 5

BIFACIAL PEROVSKITE SOLAR CELL

5.1 Introduction

The efficiency of single junction perovskite solar cell has been recently boosted to more than 20%, which is above 65% of its efficiency limit. Pushing the efficiency further up would be more and more difficult.

As we mentioned in Chapter 2.5, the Shockley-Queisser limit can be boosted by using a tandem structure. A GaAs tandem solar cell from Sunlab[72] is shown in Figure 5.1 (a). This tandem solar cell is made by stacking three individual solar cells on top of each other with tunnel junction in between. The solar cell with larger bandgap is placed on the top while the one with smaller bandgap is placed on the bottom. Tandem solar cells can significantly broaden the absorption range of the device, which is shown in Figure 5.1 (b), and thus improves the power conversion efficiency.

Figure 5.2 depicts the theoretical efficiency of a tandem solar cell under different combinations of top cell and bottom cell bandgaps[73]. If we use c-Si as the bottom cell (1.1 eV bandgap), in order to achieve maximum efficiency, the bandgap of the top cell should be around 1.7 eV. The bandgap of perovskite can be easily made into 1.7 eV by tuning the composition of organic cations[70,74,75]. If we make a perovskite-silicon tandem, the theoretical efficiency can be as high as 45%. So, using perovskite as the top cell in a tandem system is one of its most important application.

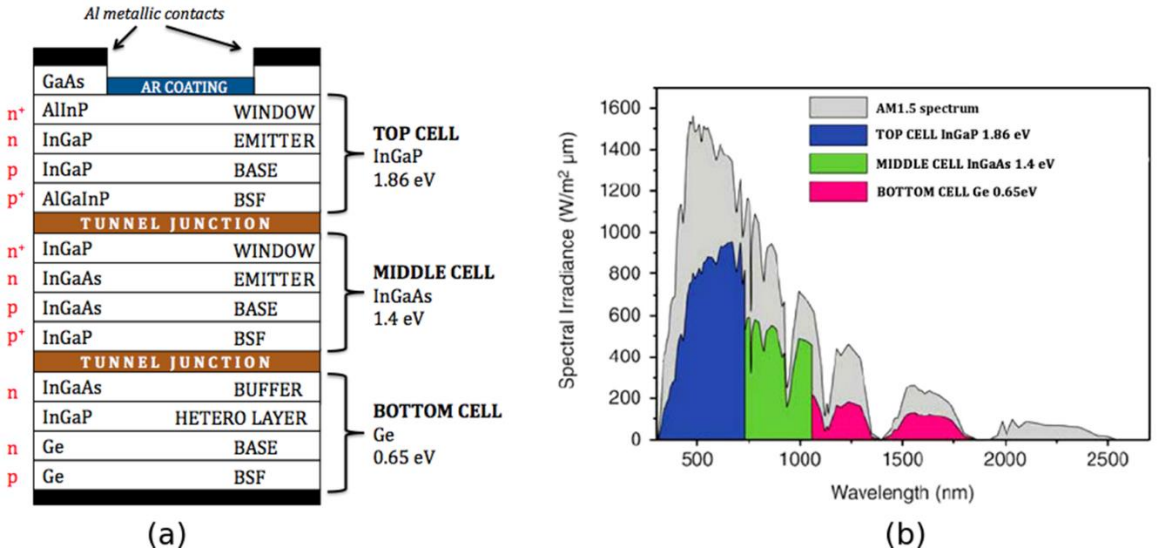

Figure 5.1: (a) Device structure of a GaAs tandem solar cell made of three junctions (b) The absorption spectrum of this tandem cell; each junction of solar cell is responsible for the photon absorption in a specific range[72].

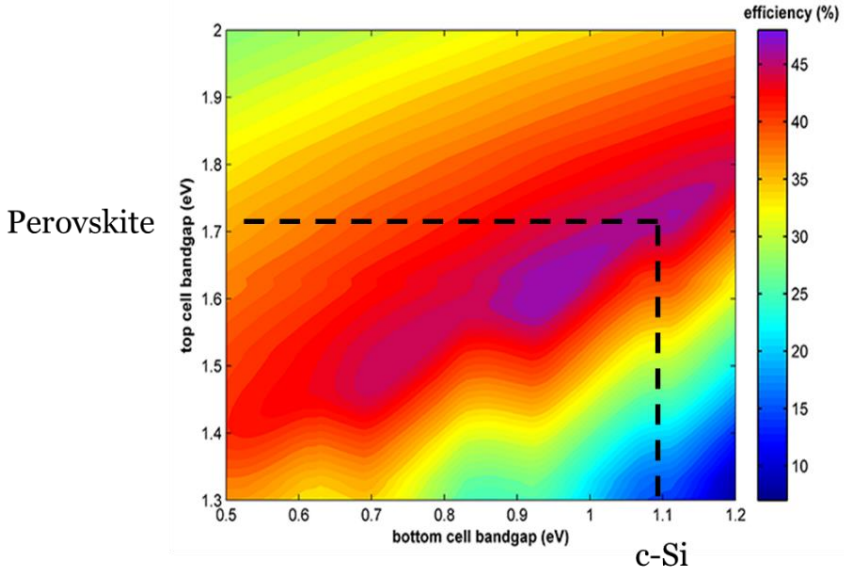

Figure 5.2: Theoretical efficiency of tandem cells as a function of top cell bandgap and bottom cell bandgap[73].

5.2 Fabrication Technique

5.2.1 Introduction of bifacial perovskite solar cells

In order to be the top of cell in a tandem, the perovskite top cell should allow the light to enter from the both sides. This means both sides of the device should be covered by transparent layers, as shown in Figure 5.3 (a). One side is used to let light enter the perovskite layer and get absorbed, and the other side is to let unabsorbed light leave the perovskite layer for entering the silicon cell underneath. This is what is called a bifacial solar cell. A perovskite-silicon tandem cell is formed when we put a bifacial perovskite solar cell on top of a silicon solar cell. A typical perovskite-silicon tandem is represented in Figure 5.3 (b).

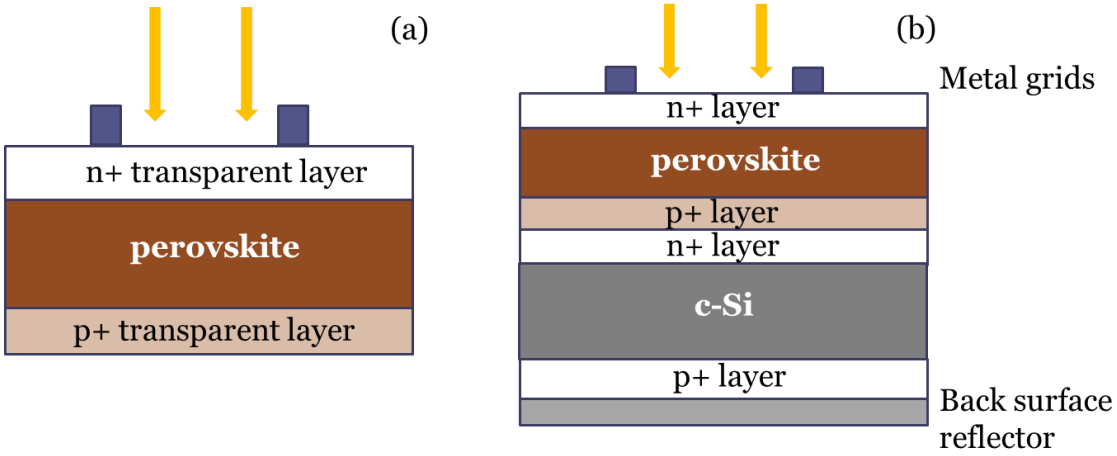

Figure 5.3: (a) Device structure of a bifacial perovskite solar cell (b) A perovskite-silicon tandem cell formed by placing a bifacial perovskite solar cell on top of a silicon cell.

5.2.2 Room-temperature ZnO:Al sputtering

The p^+ transparent layer of a bifacial perovskite solar cell can be either PEDOT:PSS or NiO. To avoid conduction band mismatch and Voc loss, the conduction band level of n^+ transparent should be close to -3.8 eV. In this case, the material we can used would be either

ITO, SnO, or ZnO:Al. Since this n^+ layer is deposited on top of perovskite, the deposition temperature must be less than 100 ℃. However, most of the deposition techniques of ITO and ZnO:Al are performed at temperature higher than 150 ℃, which remains as a challenge for our bifacial perovskite solar cell fabrication process.

Here, we have developed a room-temperature ZnO:Al sputtering process. The transmission of room-temperature ZnO:Al film is shown in Figure 5.4. Compared with our standard ZnO:Al process, which is done at 150 ℃, there is no sacrifice in transmission. Both exhibit same transmission response all over the wavelength. However, the resistivity of the film increases from 2E-4 Ω*cm to 2E-3 Ω*cm when the process temperature reduces from 150 ℃ to room-temperature. But 10^{-3} resistivity is still fine for a transport layer.

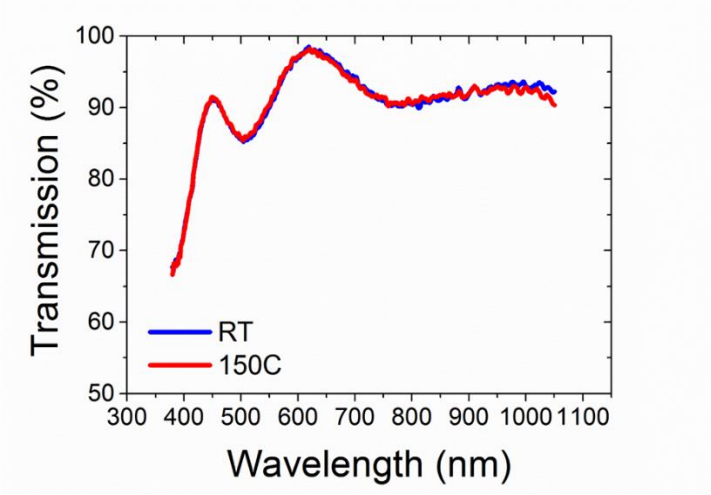

Figure 5.4: Transmission of ZnO:Al deposited with room-temperature substrate and 150 ℃ substrate.

5.2.3 CdS buffer layer

After being able to deposit high quality ZnO:Al at room temperature, we tried to made a device by depositing ZnO:Al on top of perovskite layer. However, due to its unstable nature, the perovskite layer was destroyed by the Argon plasma during sputtering, even after we

reduced the power to 20W. The photo of perovskite after ZnO:Al sputtering deposition is shown in Figure 5.5.

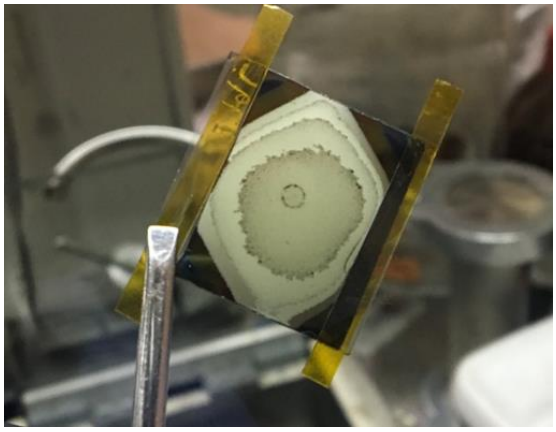

Figure 5.5: Perovskite film is destroyed by Argon plasma during deposition.

Clearly, we need a buffer layer on top of perovskite to protect it. We choose CdS as the buffer layer due to the following reasons. First, CdS can be deposited using thermal or e-beam evaporation, both of which will leave minimal damage to the substrate during deposition. Second, the conduction band of CdS is around -4 eV, which perfectly match the conduction band of perovskite. Third, CdS can be easily doped to achieved higher conductivity. The absorption coefficient curves of both indium doped and undoped CdS are depicted in Figure 5.6. The bandgap of CdS is calculated to be around 2.5 eV from the absorption data. After being doped with indium, the conductivity of CdS increased by 1000 time, from 1.4E-2 to 20 S/cm, as shown in Table 5-1.

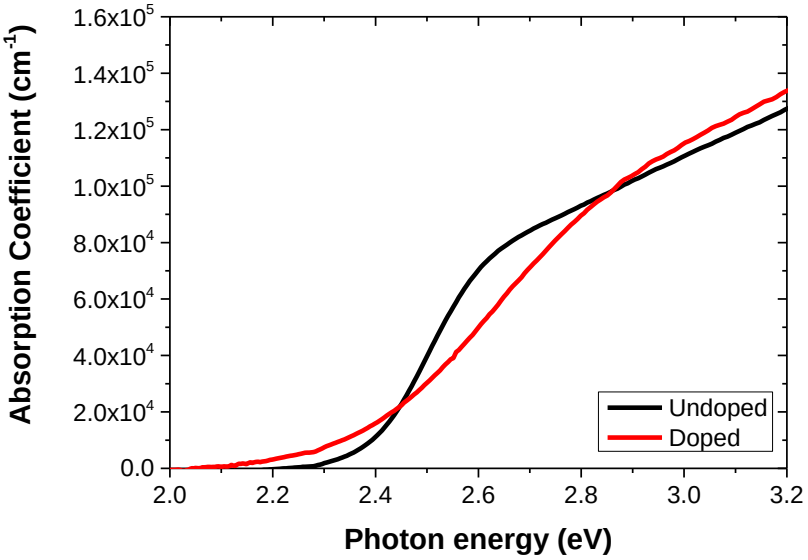

Figure 5.6: Absorption coefficient of undoped and doped CdS.

Table 5-1: Conductivity and bandgap of undoped and doped CdS

	Conductivity (S/cm)	Bandgap (eV)
Undoped CdS	1.4E-2	2.46
Indium doped CdS	20	2.52

After depositing 100 nm of CdS:In, we are able to sputter 320 nm of ZnO:Al without damaging the perovskite layer. The complete device structure is illustrated in Figure 5.7 (a). The light IV of the device is provided in Figure 5.7 (b). When the light comes from the top ZnO:Al layer, this device offer a power conversion efficiency of 11.4% with 1.01V Voc, 15.8 mA/cm^2 Jsc, and 71% FF. This efficiency is lower than that of our standard perovskite solar cell (~15%). It is mostly due to the drop of short-circuit current, which is only 15.8 mA/cm^2 when compared with the Jsc of 20 mA/cm^2 in standard cell.

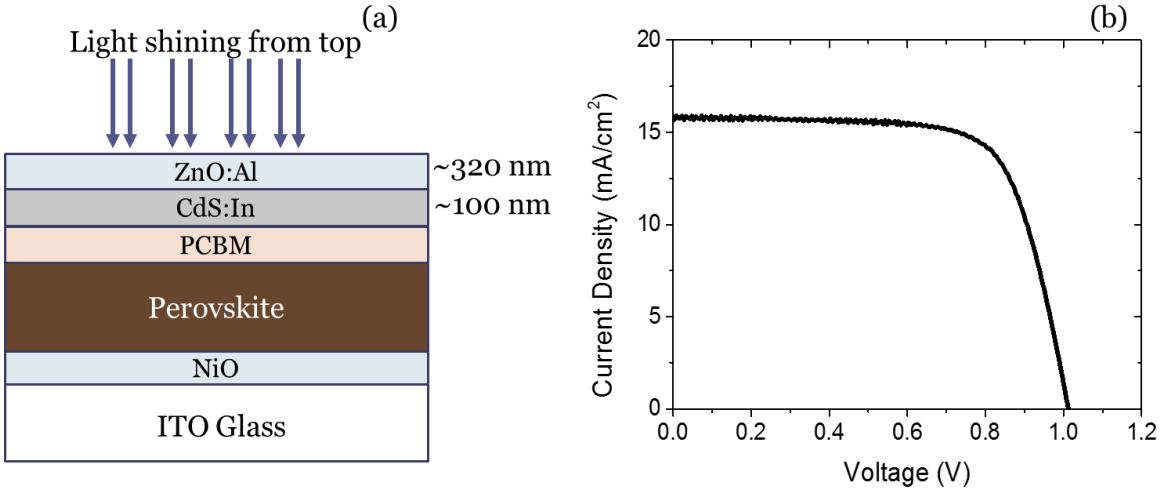

Figure 5.7: (a) Device structure of bifacial perovskite solar cell with 100nm of CdS:In and 320 nm of ZnO:Al (b) IV curve of this cell. The efficiency of the device is 11.4% with 1.01V V_{oc}, 15.8 mA/cm^2 J_{sc}, and 71% FF.

The QE data in Figure 5.8 tells us why we would have such a low current. We observe a huge reduction in QE signal between 400 to 525 nm. And this is due to the parasitic absorption in CdS:In layer since the bandgap of CdS:In is 2.5 eV, which matches the onset of absorption edge.

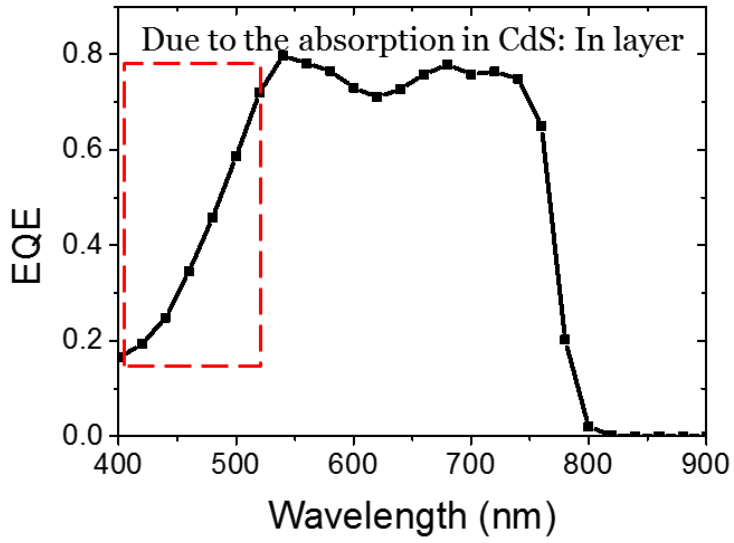

Figure 5.8: QE of bifacial perovskite solar cell with 100 nm thick CdS:In. There is huge reduction in QE signal between 400 to 525 nm because of the parasitic absorption in CdS layer.

5.2.4 Device optimization

In order to reduce the parasitic absorption in CdS:In layer, we gradually reduce the thickness of CdS:In layer. As shown in Figure 5.9, there is a significant recovery of QE signal in the low wavelength range after the thickness of CdS:In reduced from 100 nm to 50 nm and further to 25 nm. There is a trade-off between parasitic absorption and film protection for CdS:In layer thickness optimization, and we find 25 nm of CdS:In works the best.

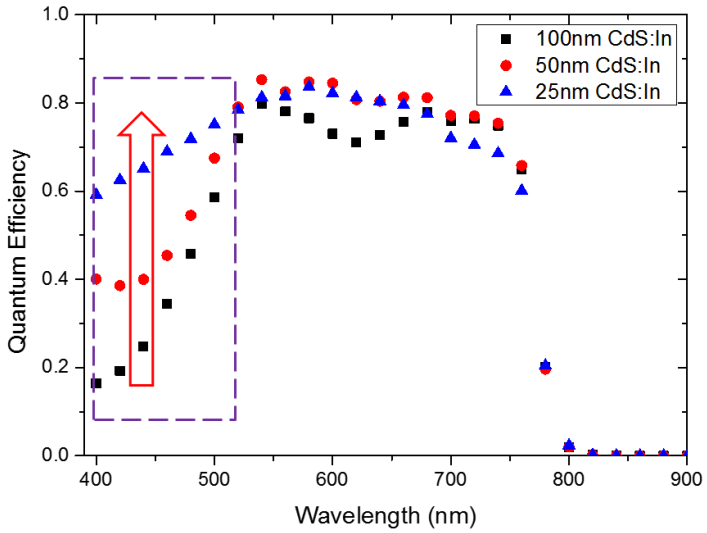

Figure 5.9: QE of bifacial perovskite solar cell with 100 nm, 50 nm, and 25 nm thick of CdS:In. We observe a significant increase of QE signal between 400 nm to 525 nm.

After depositing 25 nm of CdS:In and 380 nm of ZnO:Al, we successfully made a bifacial perovskite solar cell with 14% efficiency. The IV and QE of device with light coming from top and bottom are shown in Figure 5.10, and detailed device performance is presented in Table 5-2. Figure 5.11 shows how this bifacial perovskite solar cell looks through light. With 14% efficiency when the light comes from the top, this was the second best bifacial device at that time (the best in the field was 14.1%).

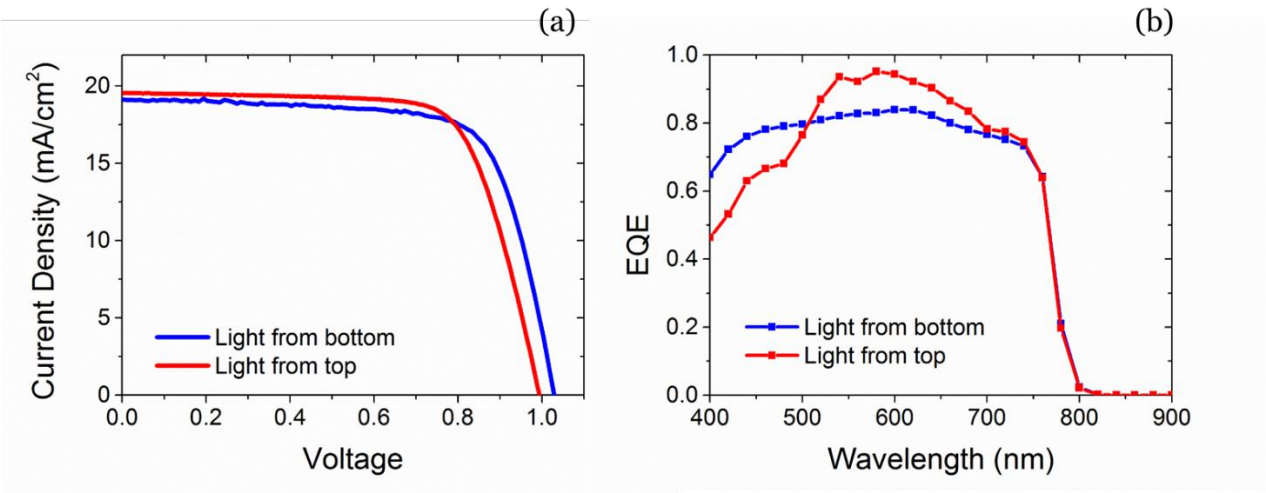

Figure 5.10: (a) Light IV of optimized bifacial perovskite solar cell with light coming either from top or bottom. (b) The corresponding QE of the device.

Table 5-2: Detailed device parameters of optimized bifacial perovskite solar cell.

	V_{oc}	J_{sc}	FF	PCE
Light from bottom	1.03 V	19.1 mA/cm^2	72%	14.2%
Light from top	1 V	19.5 mA/cm^2	72%	14%

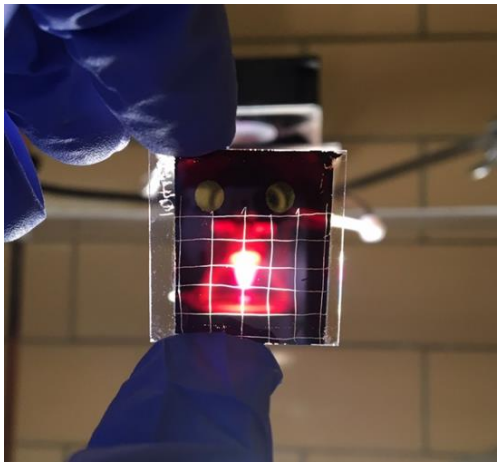

Figure 5.11: Photo of bifacial perovskite solar cell illuminated under light.

5.3 Diffusion Length from QE vs. Bias

Apart from being the top cell in a tandem system, bifacial perovskite solar cell also provides us a way to measure the diffusion length of both electrons and holes.

This measurement consists of two parts. Firstly, the CV measurement is performed to determine the depletion width of the device under each bias. Secondly, the QE vs. bias is measured with light shining from the top and bottom. Then, normalized QE vs. depletion width is plotted, which is shown in Figure 5.12.

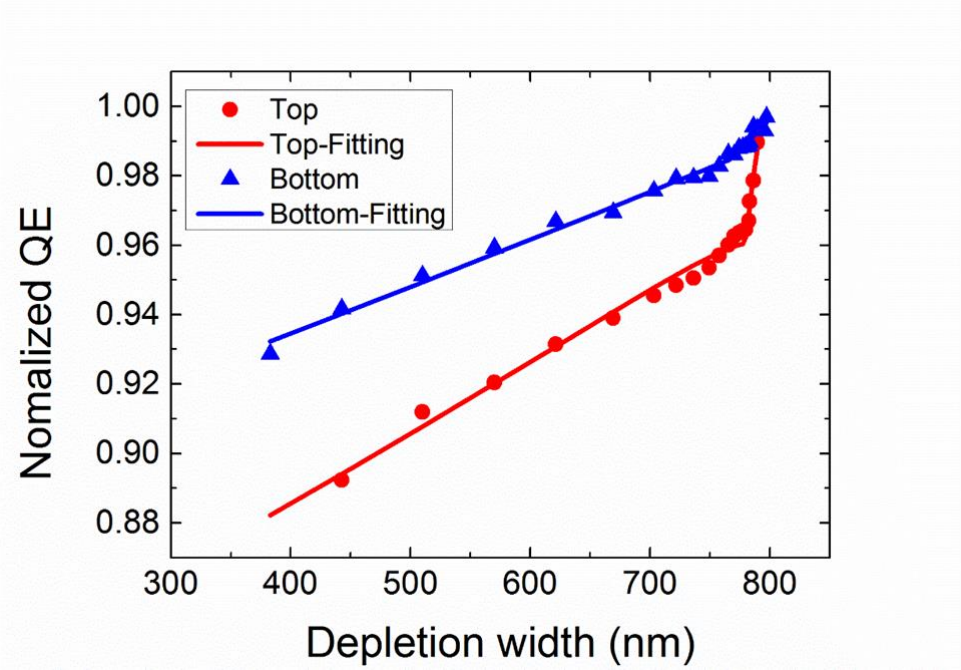

Figure 5.12: Normalized QE vs. depletion width with light coming either from top or bottom. The scatter data points are from measurement.

Based on the device parameters of perovskite layer in Figure 5.13, the relation between QE and diffusion length can be expressed by following equations.

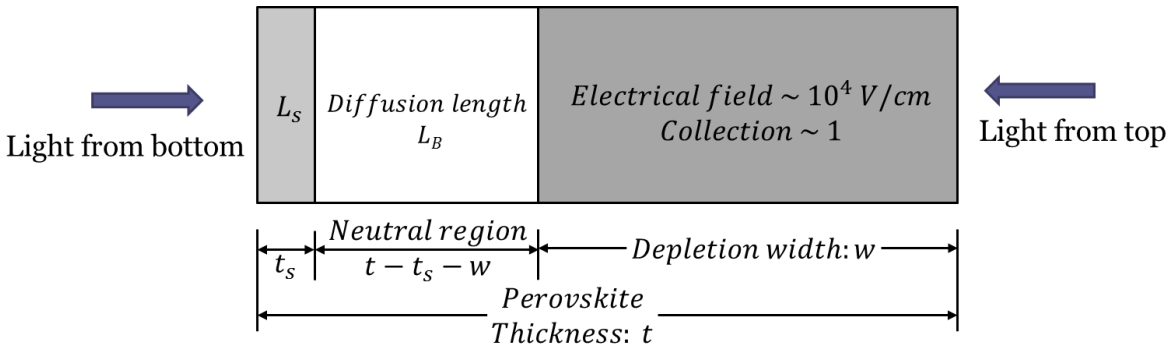

Figure 5.13: Device parameters in perovskite layer.

When light comes from the bottom layer (NiO side),

$if\ w \geq t - t_s,$

$$QE = (1 - e^{-\alpha w})e^{-\alpha(t-w)} + e^{\frac{-(t-w)}{L_s}} \frac{\alpha L_s}{\alpha L_s - 1}\left(1 - e^{\frac{-(t-w)}{L_s}(\alpha L_s - 1)}\right) \tag{5.1}$$

$if\ w \leq t - t_s,$

$$QE = e^{-\frac{t-w-t_s}{L_B} - \frac{t_s}{L_s}} \frac{\alpha L_s}{\alpha L_s - 1}\left(1 - e^{-\frac{t_s}{L_s}(\alpha L_s - 1)}\right)$$

$$+ e^{-\frac{t-w}{L_B}} \frac{\alpha L_B}{\alpha L_B - 1}\left(e^{-\frac{t_s}{L_B}(\alpha L_B - 1)} - e^{-\frac{t-w}{L_B}(\alpha L_B - 1)}\right) + e^{-\alpha(t-w)}$$

$$- e^{-\alpha t} \tag{5.2}$$

When light comes from the top (ZnO:Al side),

$if\ w \geq t - t_s,$

$$QE = (1 - e^{-\alpha w})e^{-\frac{t-w}{L_s}} + e^{-\left(\alpha w + \frac{t-w}{L_s}\right)} \frac{\alpha L_s}{\alpha L_s - 1}\left(1 - e^{-\frac{t-w}{L_s}(\alpha L_s - 1)}\right) \tag{5.3}$$

$if\ w \leq t - t_s,$

$$QE = e^{-\frac{t-w-t_s}{L_B} - \frac{t_s}{L_s}}(1 - e^{-\alpha w}) + e^{-\frac{t_s}{L_s}} \frac{\alpha L_B}{\alpha L_B - 1}\left(e^{-\left(\alpha w + \frac{t-t_s-w}{L_B}\right)} - e^{-\alpha(t-t_s)}\right)$$

$$+ \frac{\alpha L_s}{\alpha L_s - 1}\left(e^{-\left(\alpha(t-t_s) + \frac{t_s}{L_s}\right)} - e^{-\alpha t}\right) \tag{5.4}$$

In the above four equations, t is the thickness of the perovskite layer; w is the thickness of depletion layer, which changes with bias; t_s is the thickness of interface region where surface recombination dominates; L_s is the diffusion length in the interface region, and L_B is the diffusion length in the bulk region. α is the absorption coefficient.

In our measurement, light with wavelength of 420 nm is illuminated on our sample, either from the bottom side or top side. By fitting the measurement data with above equations, we can extract the diffusion length of electrons and holes.

The device parameters we get by fitting the data are shown in Table 5-3.

Table 5-3: The device parameters extracted from the fitted curve.

Thickness	800 nm
Absorption coefficient	3E5 cm^{-1}
Hole diffusion length (Ls)	370 nm
Hole diffusion length (L_B)	4.7 μm
Electron diffusion length (Ls)	1.8 μm
Electron diffusion length (L_B)	7 μm

The diffusion length we extracted from the fitted curve is around 4.7 to 7 μm, which is the same range with what we got from photo-conductivity measurement.

5.4 Environmental Stability

As we discussed before, perovskite suffers from poor environmental stability; the device degrades within 5 minutes after being exposed to air. This limits its use in photovoltaic application and brings more difficulty for device characterization since most of the characterization instruments are stored in humid air.

Several approaches have been proposed to prolong the device lifetime in humid environment. Cheng's group used an epoxy layer or plastic encapsulant film to encapsulate the perovskite device and achieved good stability under humid environment[76, 77]. However, the encapsulant need either heat treatment or UV exposure, which will damage the perovskite layer. Meanwhile, the encapsulation layer also absorbs part of photons, which results in a reduction in device performance.

Here, we find that the ZnO:Al layer we grow on top of perovskite provides a great encapsulation for the perovskite layer under humid environment. Figure 5.14 (a) demonstrates the device structure of the this solar cell, which is ITO/NiO/Perovskite/PCBM/CdS/ZnO:Al/Al. The device maintains at 16% after being kept in humid air for more than 3 months.

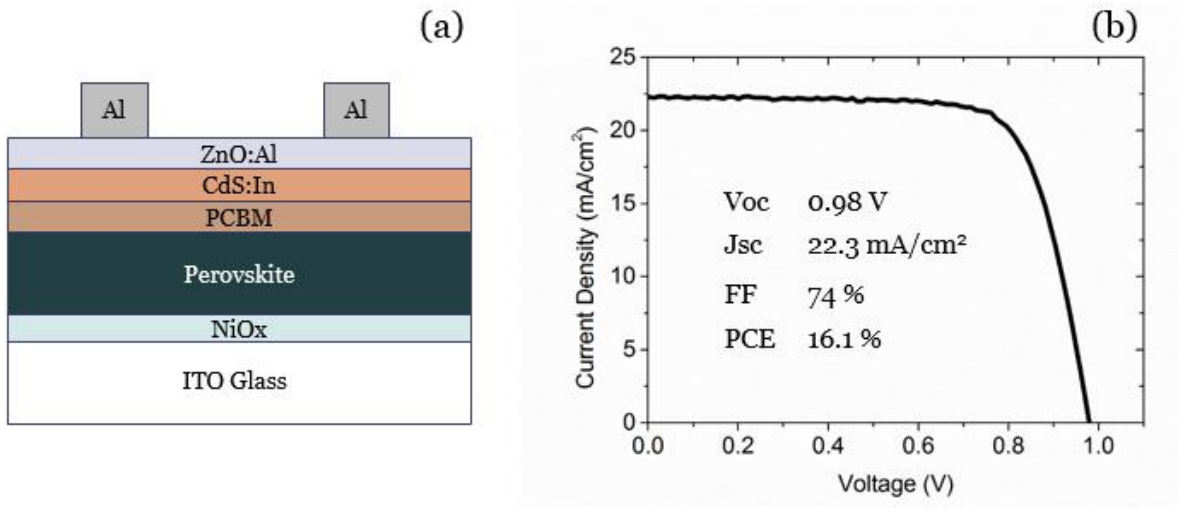

Figure 5.14: (a) The device structure of the solar cell is ITO/NiO/Perovskite/PCBM/CdS/ZnO:Al/Al. (b) Perovskite device performance stays at 16% after being kept in humid environment for more than 3 months with intrinsic encapsulation.

Since there are two extra layers added on top, which are CdS:In and ZnO:Al, we are not sure which one makes most of contribution in improving the environmental stability of this perovskite solar cell. So, we made a device with only CdS:In on top, whose device structure is

shown in Figure 5.15 (a). The IV curve and device performance is provided in Figure 5.15 (b). It also has an initial power conversion efficiency of 16%. Notice that this device has a Voc of 1.09 V, which is much higher than the normal ones (around 1V). The improvement of Voc will be covered in next chapter.

We first expose this device in humid air (about 50% relative humidity) for 20 minutes. There is no change in IV curve, as shown in Figure 5.16. However, after we stored this device in N_2 environment for more than 1 day, the series resistance of device starts to increase, and resulted in a reduction in efficiency. This tells us that CdS:In layer is not good enough to protect perovskite layer for more than 3 months, and most of protection should come from the ZnO:Al layer although CdS:In does have some blocking effect.

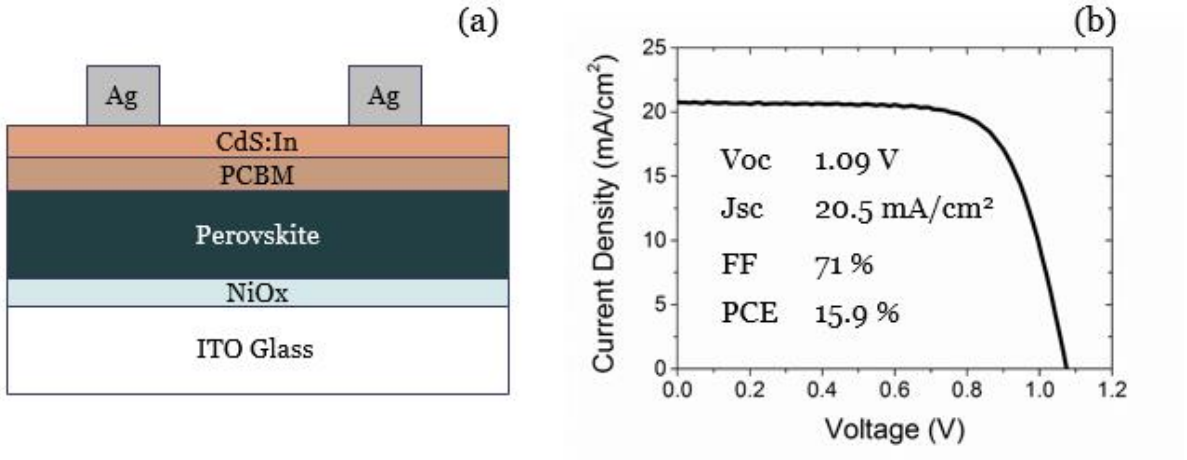

Figure 5.15 (a) The device structure of solar cells without ZnO:Al on top (b) IV of this cell after fabrication.

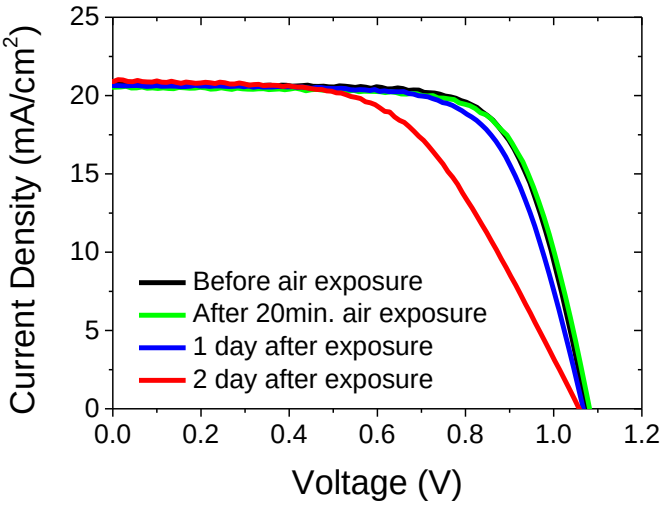

Figure 5.16: Change of IV curves over time of the device exposed to moisture.

Similar work has been done by Yang Yang's group[78]. However, they used spin-coated nano-particle ZnO, which is not as compact as our sputtered ZnO. Thus, the encapsulation effect is not as good as ours. Their device shows a 10% decrease in efficiency after being kept in air for 2 months.

CHAPTER 6

PHOTON INDUCED DEGRADATION OF PEROVSKITE SOLAR CELL

6.1 Introduction

In the early stage of the research on perovskite solar cell, efficiency improvement was placed at the first place in the field. However, no so much research was done on the stability of perovskite, especially the photo-induced degradation. Now, we have already achieved more than 20% efficiency; it is time for us to switch to solving the stability issue.

The stability of perovskite mainly consists of thermal instability, environmental instability, and photo-induced instability. Thermal stability issue can be solved by water cooling, which can keep the temperature of perovskite under 80 ℃. The environmental stability issue can also be fix by depositing a layer of ZnO:Al as an intrinsic encapsulation using our method. The only one left is the photon-induced stability issue. The photon-induced instability of a solar cell is something we cannot avoid since solar cell is designed and supposed to work under light. Particularly, as the top cell in a perovskite-silicon tandem, the perovskite layer will be exposed to most of the photons, which makes the stability of perovskite layer extremely important.

In 2013, Snaith's group reported that the TiO_2 layer in the NIP device will accelerate the photon-induced the degradation of perovskite due to the UV component in the spectrum[79]. And by replacing TiO_2 with Al_2O_3, a significant increase in stability was observed. As shown in Figure 6.1, with the application of UV filter and encapsulation, the degradation of the performance was greatly slowed. Figure 6.2 illustrates the degradation of device performance when Al_2O_3 is used. Note that, this device was exposed for 1000 hours, and there was almost no change in efficiency in the first 5 hours.

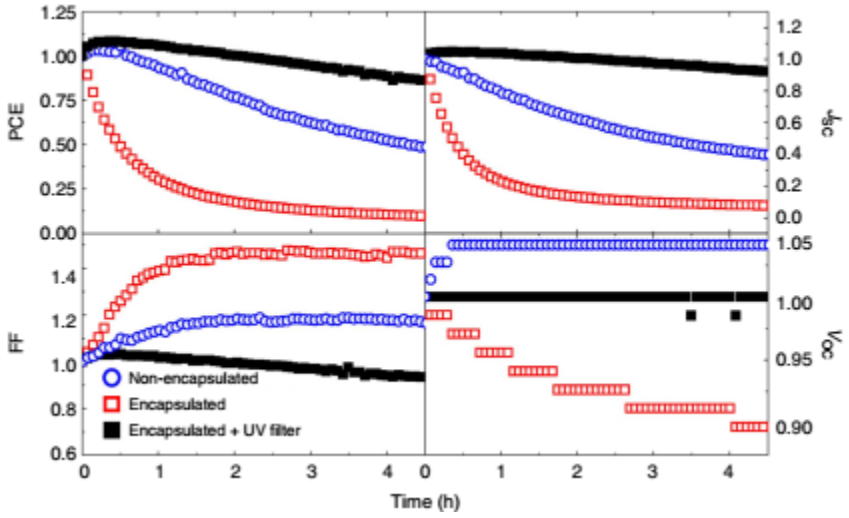

Figure 6.1: Performance degradation of the NIP device with TiO_2 under the exposure of full spectrum sun light[79].

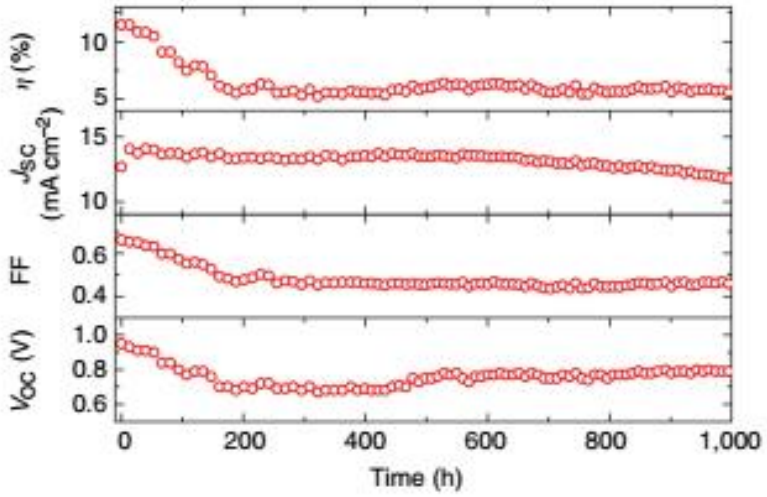

Figure 6.2: After replacing TiO_2 with Al_2O_3, the performance degradation was significantly slowed[79].

The shunt path created by metal diffusion in the transport layer is another source of degradation during light exposure. Guarnera et al found that the perovskite device with a buffer layer in the HTL degraded less after 350 hours of light exposure[80]. Figure 6.3 shows the

comparison of performance degradation between the device with and without buffer layer. The dark IV in Figure 6.4 indicates that the device with buffer layers suffers less shunt resistance problem during light exposure.

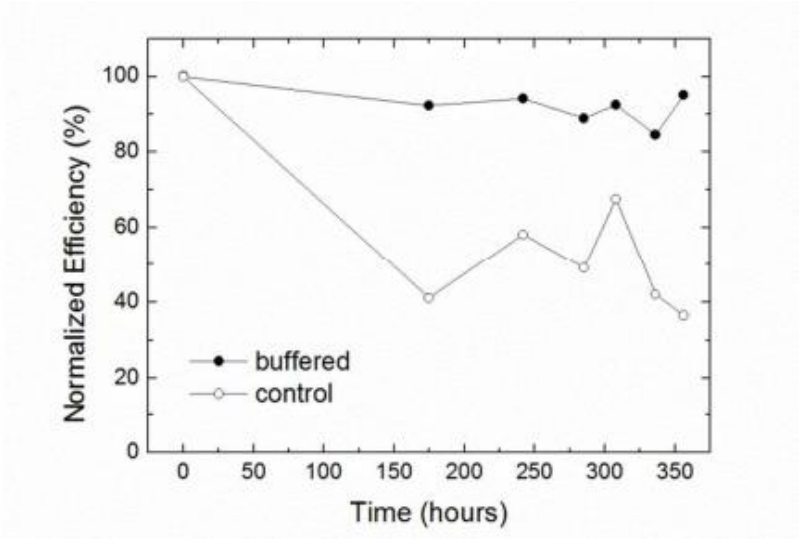

Figure 6.3: With a buffer layer in HTL, the degradation of the device performance is highly mitigated[80].

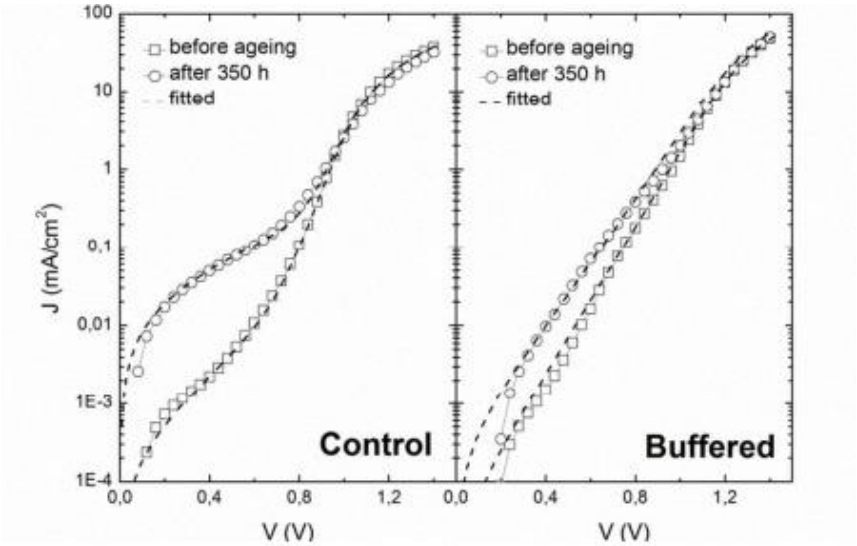

Figure 6.4: The one without buffer layer shows more shunt paths after degradation[80].

All the reports mentioned above are based on NIP device structure, and most of them suffer from hysteresis problem, which will be discussed later. Light induced degradation study on PIN device was conducted by Bag et al[81]. The device they used has a structure of ITO/PEDOT:PSS/Perovskite/PCBM/Ca/Al. The perovskite layer was made by two-step liquid process, in which PbI_2 was first spin-coated on top of PEDOT:PSS substrate, followed by spin coating of MAI solution. They also made a mixed-cation perovskite by using both MAI and FAI.

This PIN perovskite device was exposed under different light conditions.

1. White LED (without IR wavelength)
2. AM 1.5
3. AM 1.5 with air cooling
4. AM 1.5 with IR filter

From Figure 6.5 (a), the device with FA has better stability in both illumination conditions. Figure 6.5 (b) shows the efficiency degradation of $MAPbI_3$ under different exposure conditions. The one exposed by LED light has the least performance reduction while the one exposed by AM 1.5 has the most. Under the illumination of AM 1.5 spectrum and with the IR filter, there is more performance degradation when compared with LED illumination. This suggests the UV light in AM 1.5 plays a significant role in degradation mechanism. The device degrades more when there is no air-cooling nor IR filter, which means the degradation is thermally-activated.

Those reports have given us a clear understanding of the factors that could impact the photon-induced degradation process of perovskite. However, none of them has detailly studied

the device physics behind the degradation process nor proposed the degradation model, and those are what we are going to discuss in the following part of this dissertation.

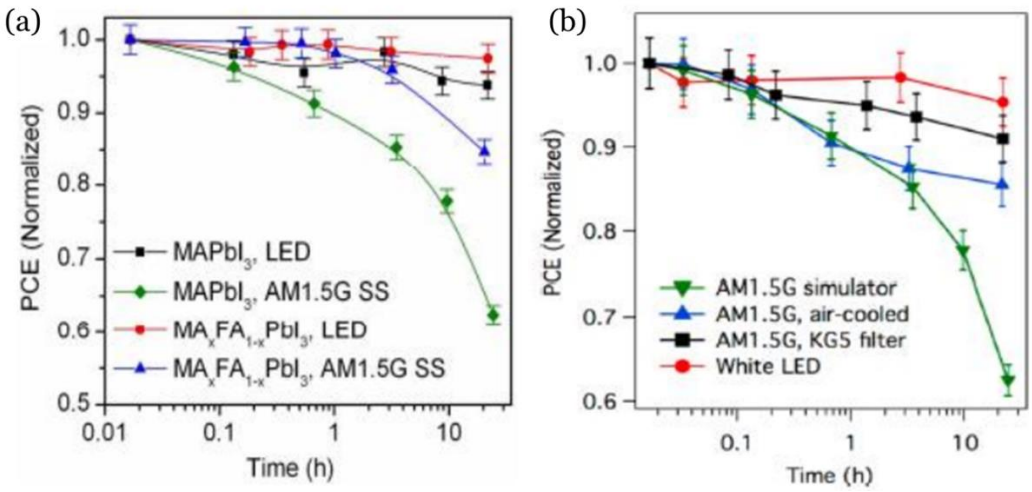

Figure 6.5: (a) Efficiency degradation of $MAPbI_3$ and $MA_xFA_{1-x}PbI_3$ devices under LED or AM 1.5 illumination. (b)) Efficiency degradation of $MAPbI_3$ under different light and cooling conditions[81].

6.2 Abnormal Behavior of Perovskite Solar Cells

6.2.1 Hysteresis

Apart from the stability issues we mentioned before, hysteresis is another problem exists in perovskite solar cell. Hysteresis happens when the IV curve of a solar cell depends on the history of the applied voltage bias. More detailed description is the IV curve of a perovskite solar cell changes when 1) it has been under a voltage bias before the voltage sweep or 2) the voltage sweep direction changes or 3) the sweep rate changes. Almost any treatment the perovskite solar cell received before or during the IV scan would change its IV curve.

This phenomenon was first reported by Snaith's group[82], and widely observed in numerous reports[83,84,85,86,87,88]. Theoretically, the IV curve of a solar cell should not change

under different voltage sweep direction. However, this kind of IV hysteresis exists in perovskite solar cells, and a typical IV curve with hysteresis is illustrated in Figure 6.6. The device was measured twice with difference voltage sweep direction: first swept from forward bias to short-circuit point then from short-circuit point to forward bias. There is distinct difference between those two IV curves. The one scanned from forward bias has much higher V_{oc}, FF, and thus PCE. The hysteresis phenomenon in perovskite solar cell leads to huge obstacle for us to accurately characterize the device and correctly interpret the device data.

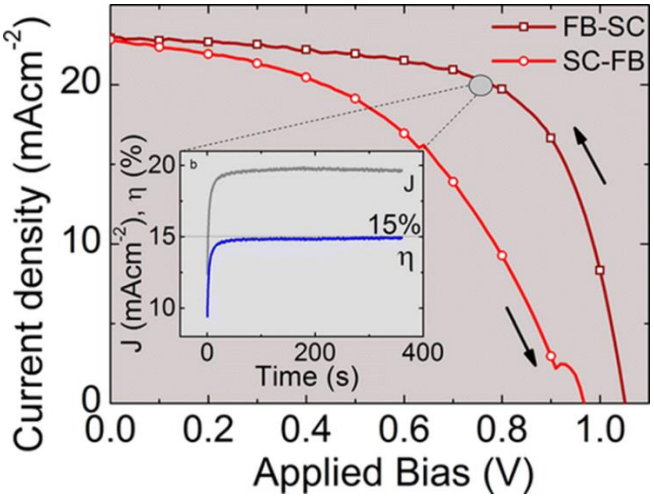

Figure 6.6: Typical IV hysteresis in perovskite solar cell[82].

The amount of hysteresis changes with sweep conditions. In Snaith's report, as shown in Figure 6.7, they found the hysteresis goes less when the sweep rate increases[82]. However, it is not the same in all perovskite films. The report from Grätzel's group[89] shows that the IV hysteresis first increases then decreases when the sweep rate goes up, which is shown in Figure 6.8. So, there is a specific sweep rate which will result in the most amount of hysteresis in each film. The reason behind this phenomenon will be discussed later.

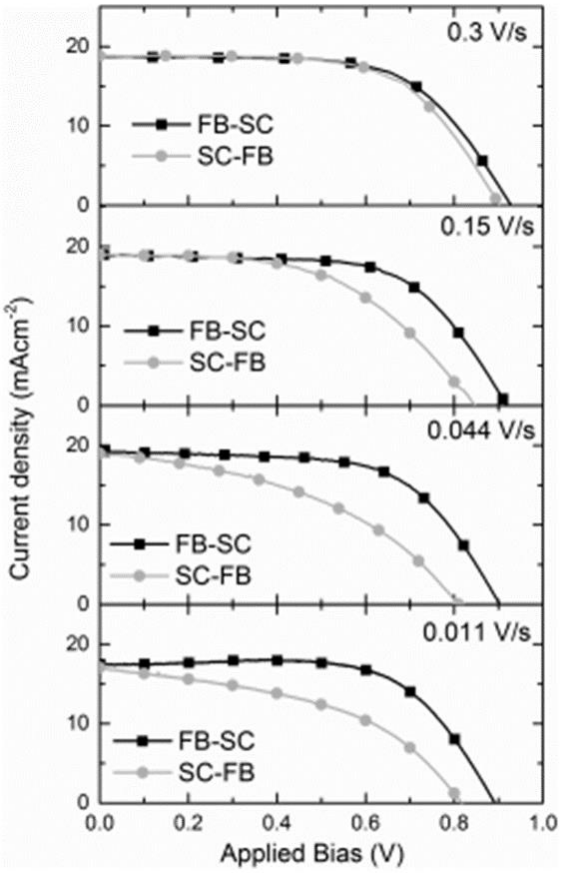

Figure 6.7: IV hysteresis changes with voltage sweep rate: less hysteresis with faster sweep[82].

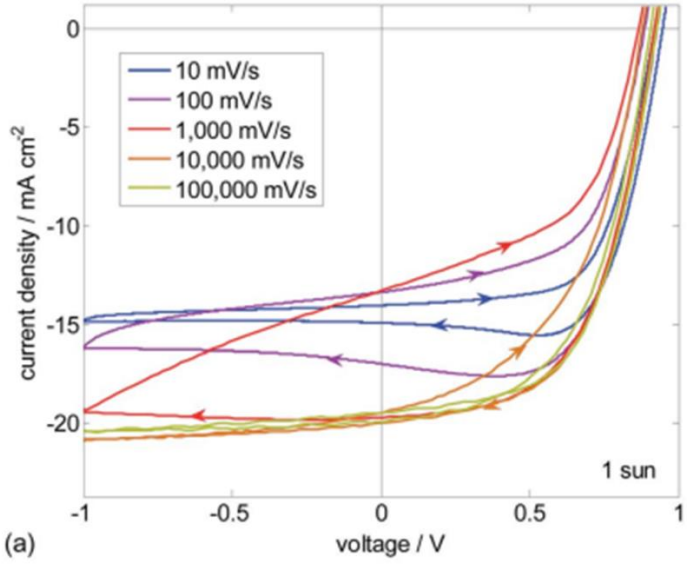

Figure 6.8: The IV hysteresis first increases then decreases when the sweep rate goes up[89].

The IV hysteresis also changes with pre-biasing condition. In Figure 6.9, with different pre-biasing condition, the IV curve changes significantly[89].

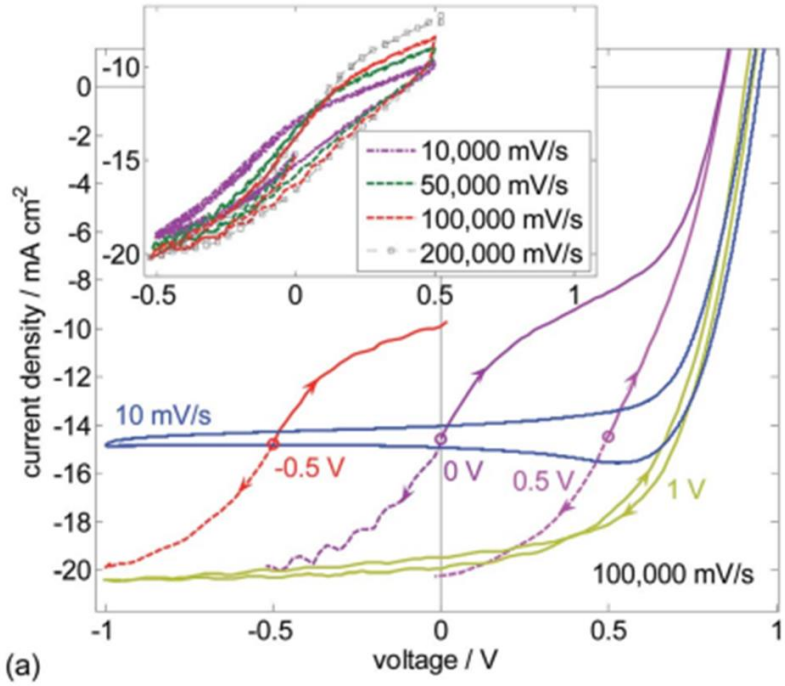

Figure 6.9: IV hysteresis changes with pre-biasing condition[89].

Apart from IV measurement parameters, the hysteresis effect also depends on the fabrication process and device structure. As shown in Figure 6.10, Park's group found that the IV hysteresis reduces when the perovskite grain size increases[83]. The hysteresis also depends on the n-type layer. With thicker mesoporous TiO_2 layer, the perovskite solar cell shows less hysteresis[83].

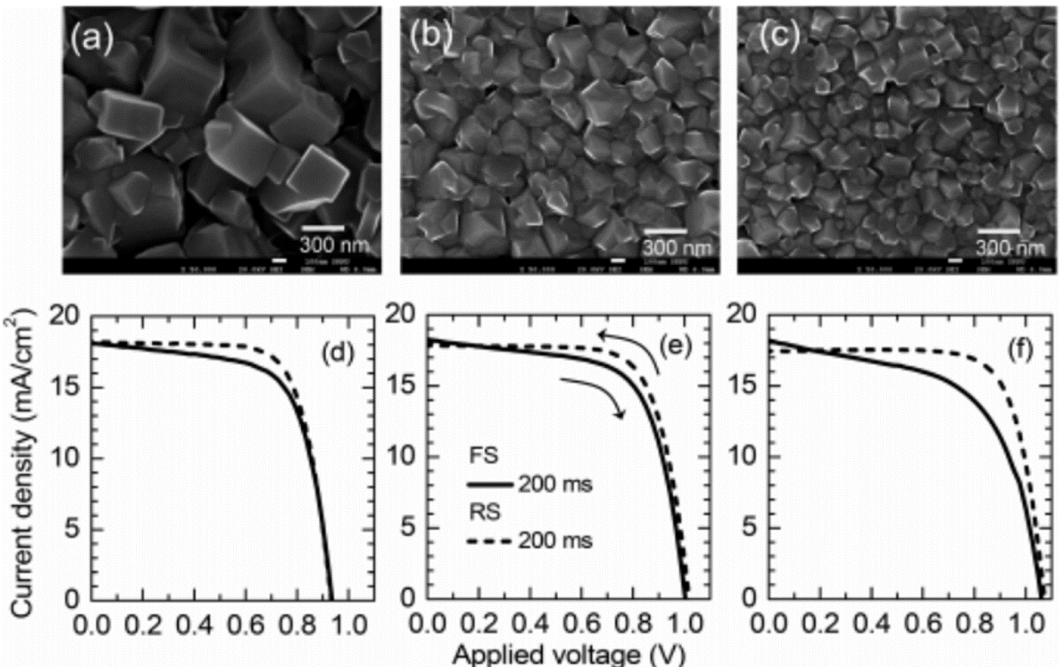

Figure 6.10: IV hysteresis reduces when the grain size increases[83].

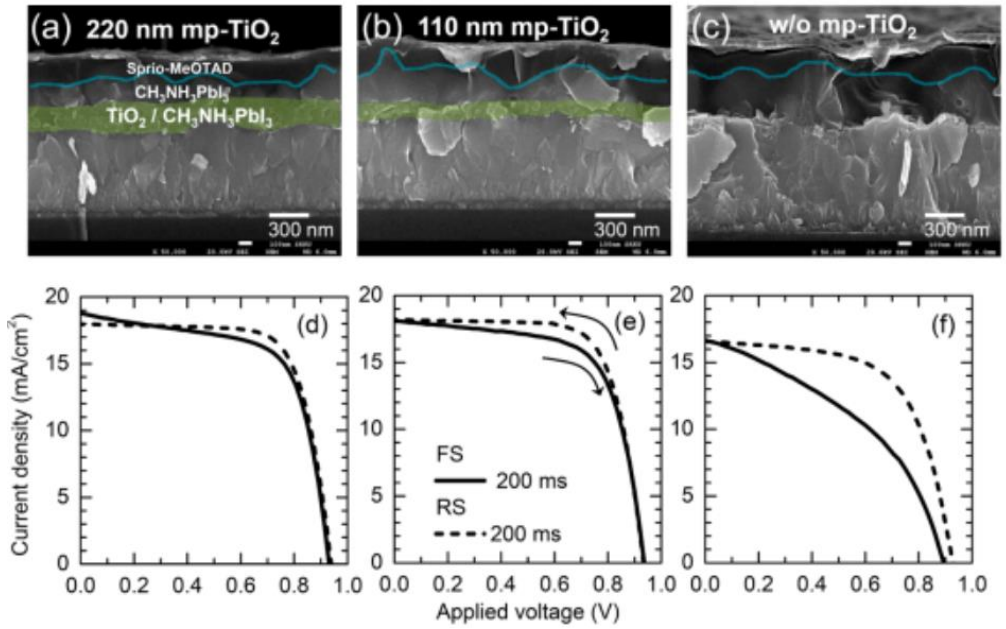

Figure 6.11: With thicker mesoporous TiO_2 layer, the perovskite shows less hysteresis[83].

6.2.2 Ion migration

The origin of hysteresis effect of perovskite solar cell was studied by lots of research groups[71,90,91,92]. Four types of mechanism were proposed to explain the IV hysteresis. 1) Ferroelectric polarization[93,94]. 2) Ion migration[95,96] 3) Charge trapping[97]. 4) Capacitive effects[83,87].

Among all of them, ion migration mechanism is the most adopted one in the field. It was first proposed by Huang's group[98]. The device structure they used is shown in Figure 6.12 (a). The perovskite layer was sandwiched by two p-type materials. So, theoretically, there should be no or minimal photo-voltage under illumination, and the IV curve will not depend on the voltage sweep direction. However, the polarity of this device changes with the bias. Figure 6.12 (b) and (c) are the dark IV and light IV of this device with different bias sweep direction. This device was biased at negative or positive voltage before the IV scan, and the Voc of device in each scan is plotted in Figure 6.12 (d). This switchable photovoltaic effect was explained by using an ion migration model. In this model, there exist two kinds of ions: positive charged cations and negative charged anion. When the device is under the polling of a positive bias or a negative bias, those two kinds of ions will drift towards the interface and accumulate on the interface, which creates an internal electric field inside the devices. When the polarity of polling bias changes, the internal electric field will change as well. This is the reason we can observe a switchable photovoltaic effect in this type of device. The accumulation of ions on the interface also results in the change of perovskite material. In Figure 6.13, it shows that the anode of the device becomes transparent after 2 hour bias pooling[98].

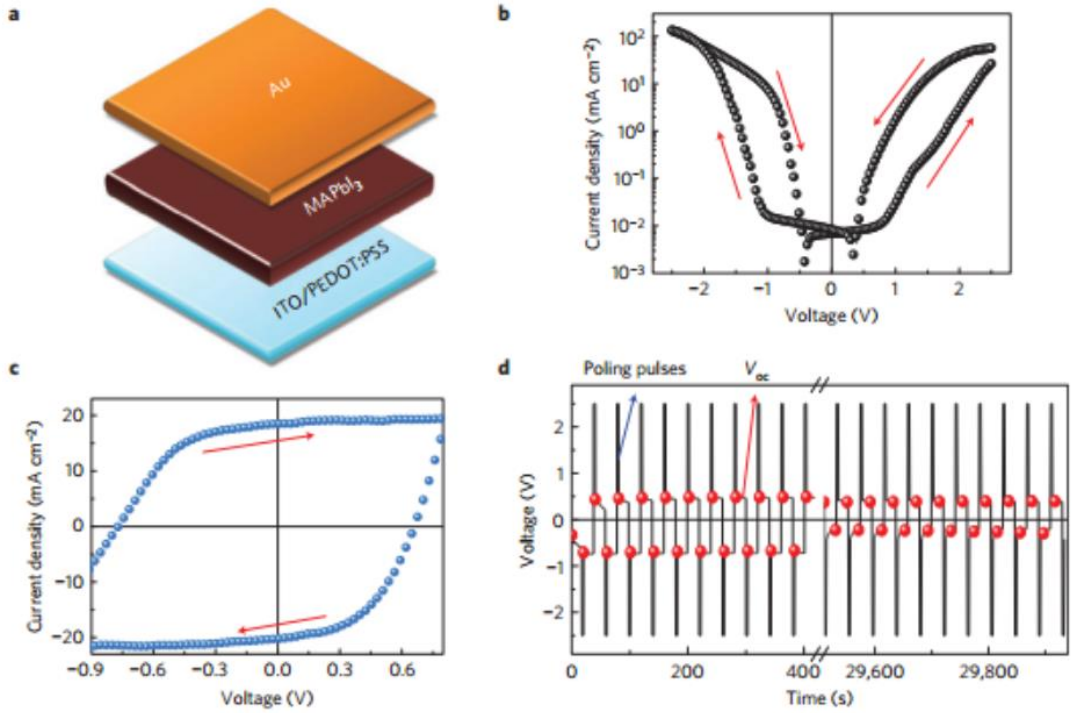

Figure 6.12: (a) Device structure of a symmetric Perovskite device. (b) Device under continuous sweep between -2.5V to 2.5V (c) Photo-current hysteresis of the device. (d) Open-circuit voltage of the device after repeated poling by 2.5V and -2.5V bias for more than 750 cycles[98]

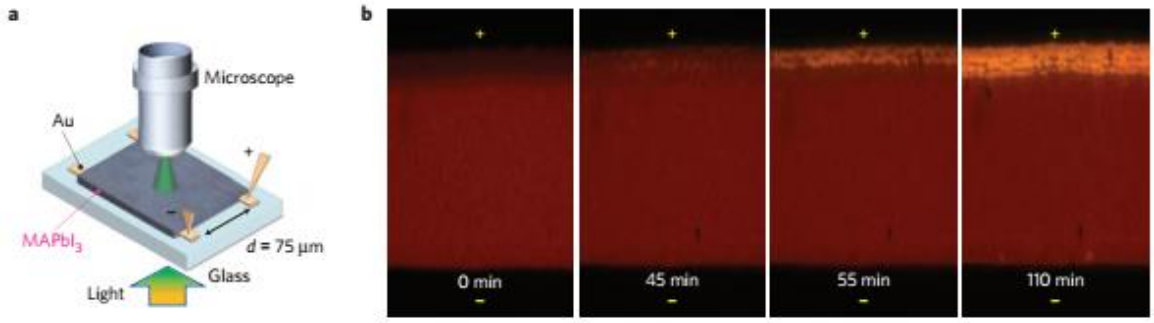

Figure 6.13: (a) Instrument and device structure used in an in-situ monitoring of polling process. (b) Microscope photos of perovskite layer during polling process[98].

Figure 6.14 is a figure from a report by Eames et al. explaining the ionic transport in perovskite[96]. Before the ion migration process, positive charged and negative charged ions are uniformly distributed in the device. Under the effect of internal electric field, the positive

charged cations drift towards the interface between perovskite and p-type layer, and the negative charged anions drift towards the interface between perovskite and n-type layer. Those charged ions on the interface screen the electric field inside the perovskite and result in a change in charge collection, which finally leads to a change in IV curve.

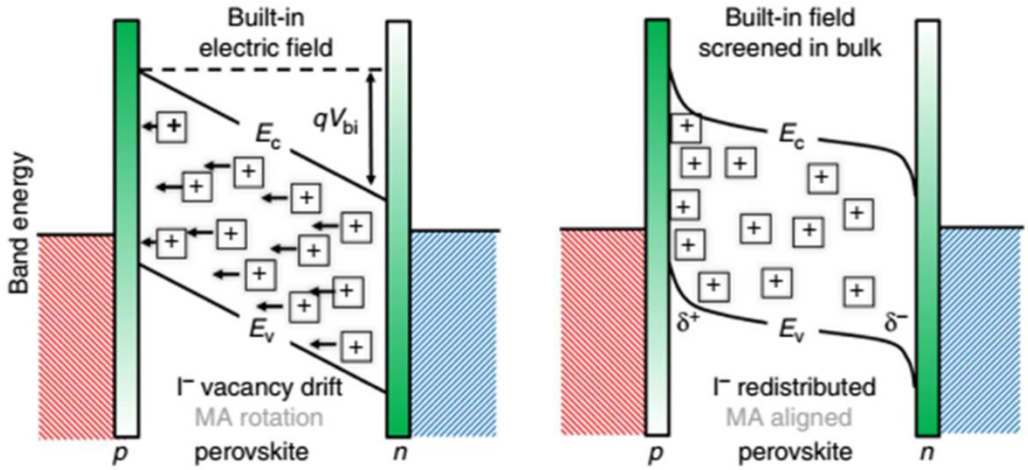

Figure 6.14: Band diagram of perovskite solar cell before and after ion migration[96].

So, what are the dominant cations and anions in perovskite? Walsh et al. calculated the formation energy of all types of defects in perovskite and found that MA and I vacancies have the lowest formation energy[99], which means most of ions generated in perovskite are MA cations and I anions. The detailed formation energy is shown in Table 6-1.

Table 6-1: Formation energy of defects in perovskite.

Reaction	ΔH_S [eV per defect]	K_c	n [cm^{-3}]
$nil \rightarrow V'_{MA} + V''_{Pb} + 3V^{\bullet}_{I} + MAPbI_3$	0.14	0.41	2×10^{19}
$nil \rightarrow V'_{MA} + V^{\bullet}_{I} + MAI$	0.08	3.82	2×10^{20}
$nil \rightarrow V''_{Pb} + 2V^{\bullet}_{I} + PbI2$	0.22	0.02	8×10^{17}

The migration activation energy shown in Table 6-2 was calculated by Eames et al[96]. MA cation and I anion have much lower activation energy than that of Pb cation, which indicates those two ions are much easier to move around the perovskite lattice.

From the formation energy and activation energy data, we can conclude that most of the mobile ions in perovskite are MA cations and I anions.

Table 6-2: Migration activation energy of I, Pb and MA vacancies[96].

Table 1 | Calculated activation energies for ionic migration in $CH_3NH_3PbI_3$.

Migrating vacancy	Defect notation	E_A (eV)
I^-	$V_I^\bullet$	0.58
Pb^{2+}	V_{Pb}''	2.31
$CH_3NH_3^+$ (MA^+)	V_{MA}'	0.84

The migration of ion species is mediated by vacancy defects.

Although those mobile ions exist in both NIP and PIN perovskite solar cells, IV hysteresis is barely visible in most of the PIN devices. This is explained by Levine and co-workers[100]. They made two perovskite solar cell with different device structure, one with PIN structure and the other one with NIP. When both devices are measured at room temperature with a bias sweep rate of 50 mV/s, the NIP shows huge hysteresis while the PIN device does not. Both IV curves are illustrated in Figure 6.15 (a). This observation is in accordance with the most of reports. However, as shown in Figure 6.15 (b), when the PIN device is measured at lower temperature (200 K), there is more hysteresis in the IV curve. Same thing also happens when the sweep rate increases, which is illustrated in Figure 6.16 (a), although it is not as significant as that at lower temperature. When measured at both lower temperature and fast sweep rate, the PIN device is observed with huge hysteresis in Figure 6.16 (b).

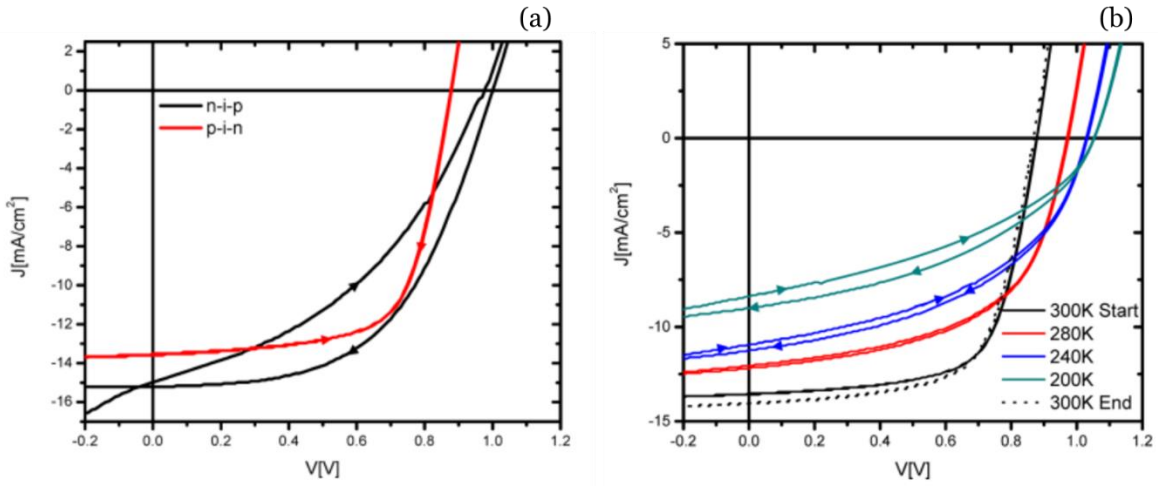

Figure 6.15: (a) IV of PIN and NIP device measured with sweep rate of 50 mV/s at room temperature. (b) PIN device measured at different temperatures with sweep rate of 50 mV/s. Device shows more hysteresis at lower temperature[100].

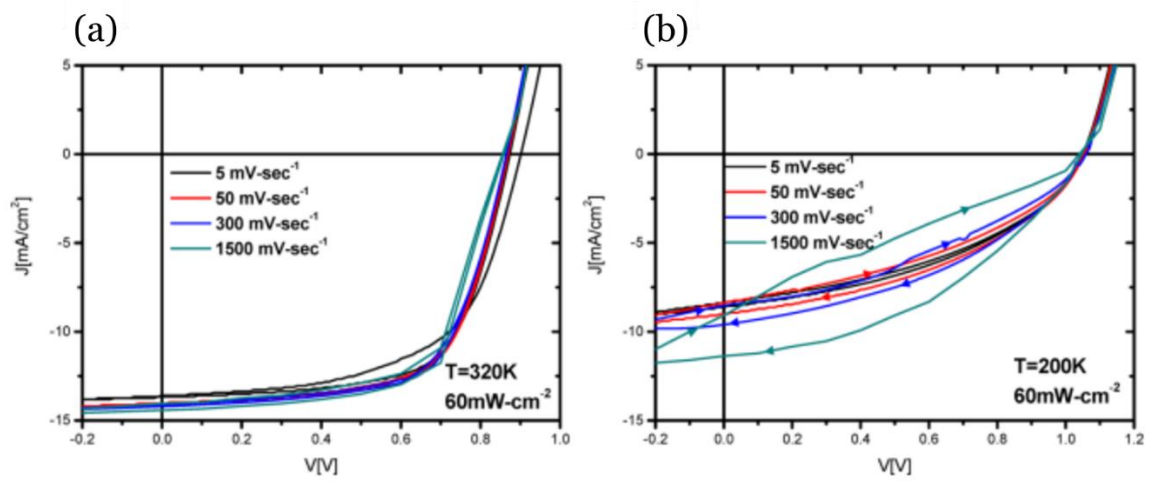

Figure 6.16: (a) PIN device measure with different sweep rate at 320K. (b) PIN device measured with different sweep rate at 200K[100].

They explained the change of hysteresis by introducing a factor R, which is defined as the ratio of scan rate to system response rate. When the scan rate is much faster than the system response rate (R is high), the mobile ions in the perovskite cannot follow the change of the voltage, which results in a low hysteresis effect. When the scan rate is much slower than system

response rate (R is low), the mobile ions can easily rearrange themselves under the bias, which also leads to a low hysteresis. Therefore, we are not able to observe hysteresis when PIN device is measured at room temperature since its mobile ion response rate is too fast. Only by lowering the measurement temperature and increasing the scan rate, the hysteresis of PIN device is revealed. What happens in NIP device falls into the third category in which the scan rate is close to the ion response rate. In this case, there is a lag between the bias change and ion motion, which leads to significant hysteresis in IV curve.

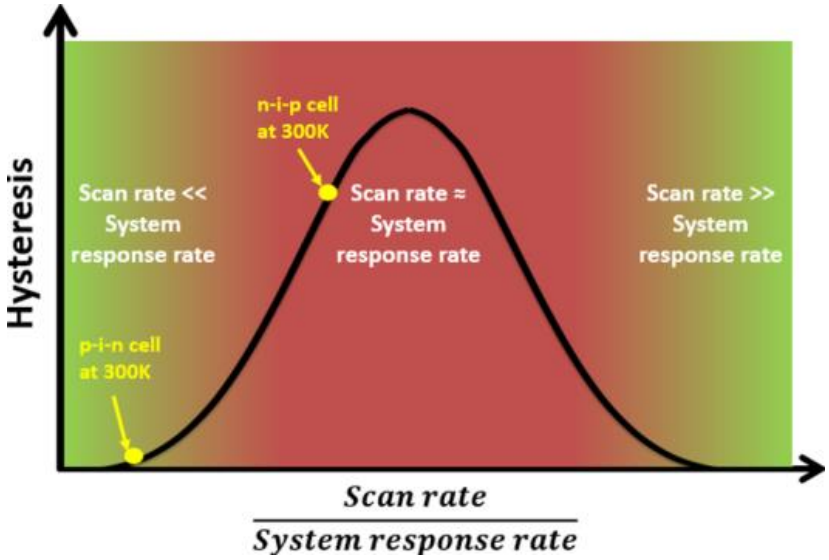

Figure 6.17: Illustration of HF (hysteresis factor) as a function of R, which is defined as the ratio of scan rate to system response rate[100].

6.3 Measurement Setup

The degradation setup we use in perovskite degradation study is an environmental chamber, which is shown in Figure 6.18. Environmental chamber has a glass window which allows the simulated light to enter and being reflected to the sample. The sample is connected to SMU and LCR meter outside of the chamber. The chamber is also connected with N_2 cylinder and vacuum pumps to control the gas environment inside.

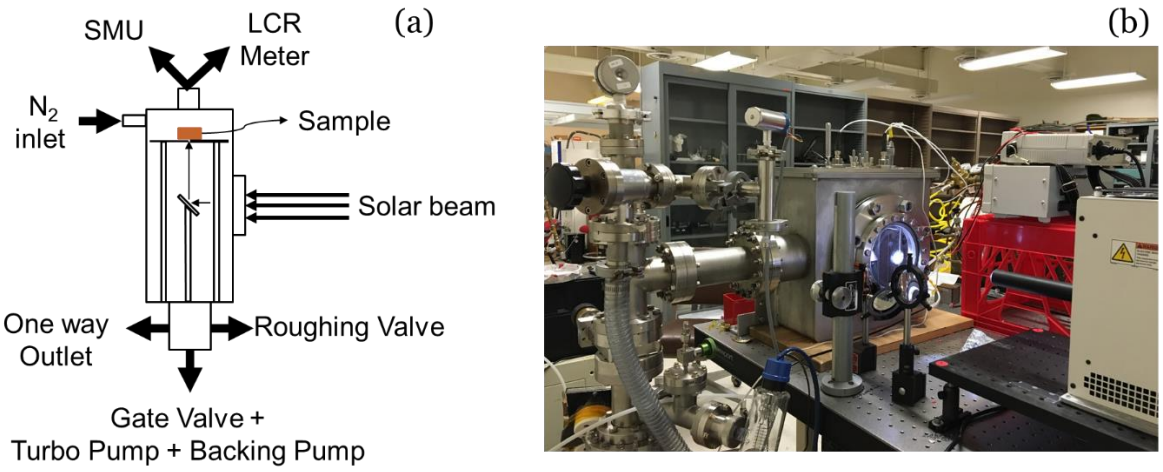

Figure 6.18: (a) Schematic of the structure of our environmental chamber (b) Photo of environmental chamber.

6.4 Photon Induced Degradation and Degradation Model

The perovskite solar cell in this work is made using a PIN structure shown in Figure 6.19. First, a 30nm thick NiO layer is deposited using e-beam evaporation, followed by 200 ℃ thermal annealing in air for 1 hours. Then, perovskite layer is spin-coated with process recipe from Park's group[48]. After that, around 60 nm of PCBM is deposited by spin-coating 20mg/ml PCBM solution in chlorobenzene. Finally, 100 nm of aluminum is evaporated on top of the device.

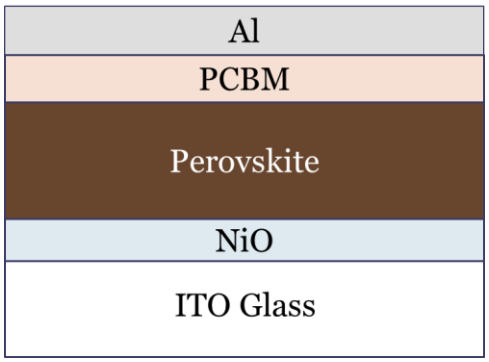

Figure 6.19: Device structure of the PIN perovskite device we used in this work.

Figure 6.20 suggests that the grain size of the perovskite layer is around 200 nm. Later we will also discuss the effect of grain size on the photo-induced degradation.

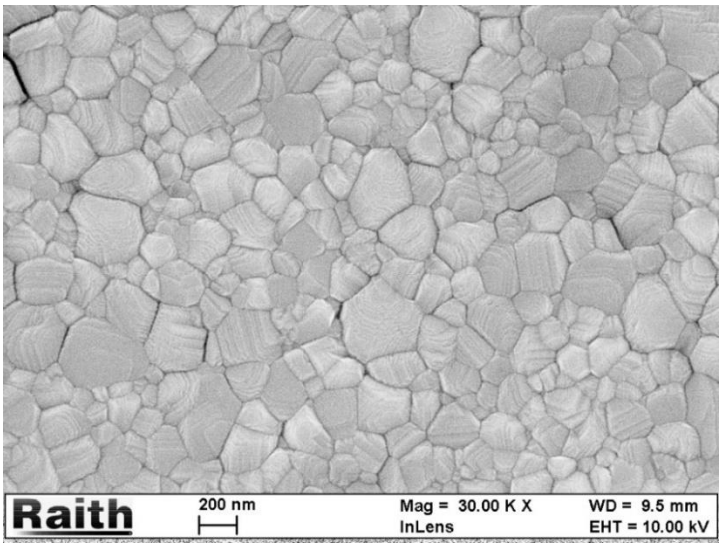

Figure 6.20: SEM image indicates around 200 nm perovskite grain size.

The typical efficiency of the device is around 13%, and the best efficiency is around 15%. Figure 6.21 depicts a typical IV curve of PIN perovskite solar cell, and there is no hysteresis when the voltage bias is swept in different direction after fabrication.

PIN perovskite solar cell samples are then loaded into the environment chamber for light exposure study. The sample is first kept under vacuum (~1E-6 Torr) in dark condition for more than 3 hours to make sure that most of the trapped O_2 and H_2O are released. Then, the environmental chamber is filled with N_2 and maintained at a pressure close to 1 atm. During the light exposure, the sample is always blew with cool N_2 to make sure it is not overheated. The light intensity during exposure can be adjusted to 25%, 50%, 100%, 200%, 400% of the intensity of sunlight, depending on which exposure condition we want.

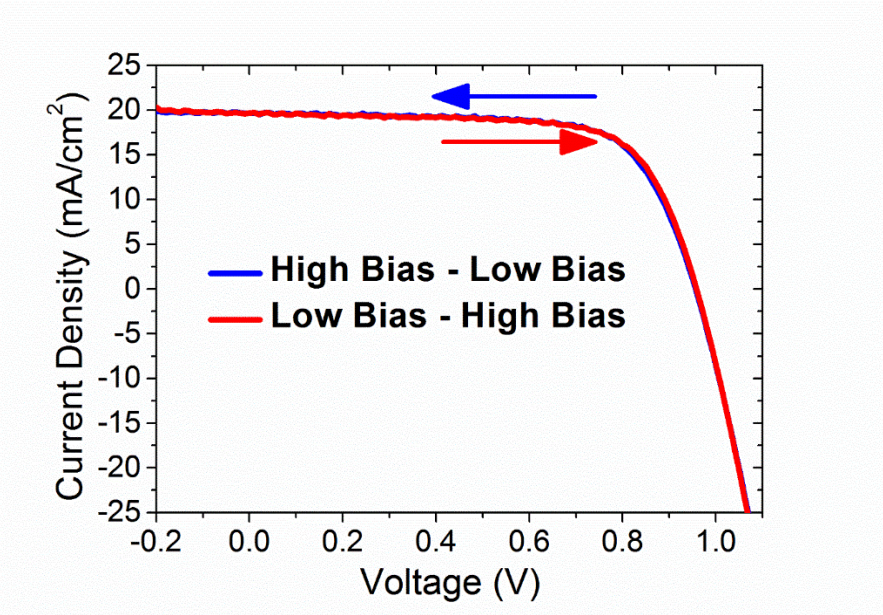

Figure 6.21: Typical IV curve of a PIN perovskite device with no hysteresis.

6.4.1 Change of IV during and after exposure

In this study, we keep our PIN device at open-circuit condition during exposure. The light intensity is set as 1X as default.

Figure 6.22 illustrates how the IV curve change during and after exposure. The detailed change of performance over time is provided in Figure 6.23. Unlike the degradation process of a-Si and organic solar cells in which all the IV parameters decrease during exposure[101], the Voc of perovskite device gradually increases and saturates to about 15% higher than the initial value during 100 hours of light exposure. However, the Isc will decrease by 35% during exposure. Fill factor normally does not change and stay stable around 100%. Overall, the efficiency would decline by 25% after 100 hours of one-sun exposure.

What makes the degradation process of perovskite solar cell more interesting is the unique “recovery” of device performance. After being kept in dark condition for some time

(normally 15 to 24 hours), the performance of the device will revert to its initial condition, and the IV curve turns back to where it was before the exposure.

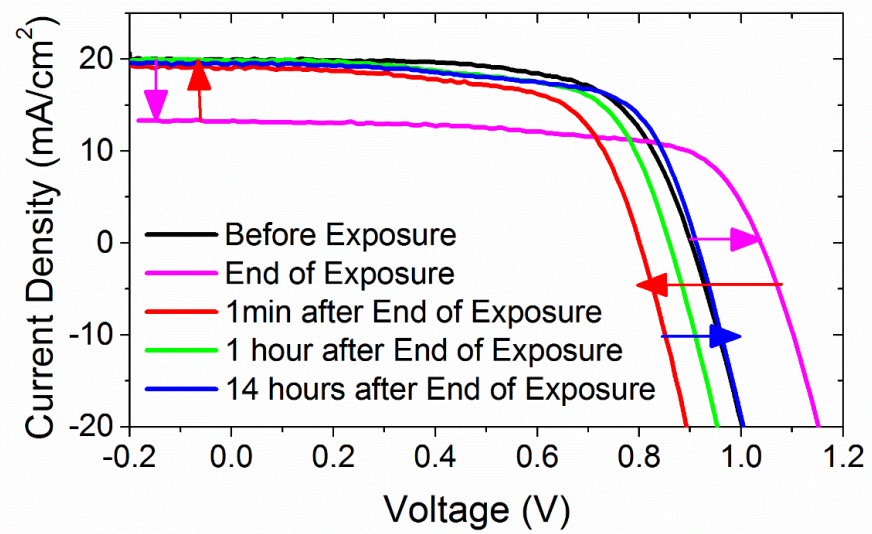

Figure 6.22: Change of IV after exposure. Voc increases during light exposure and suddenly drops below the original value just after exposure, and then it gradually increases back to the initial Voc during recovery process.

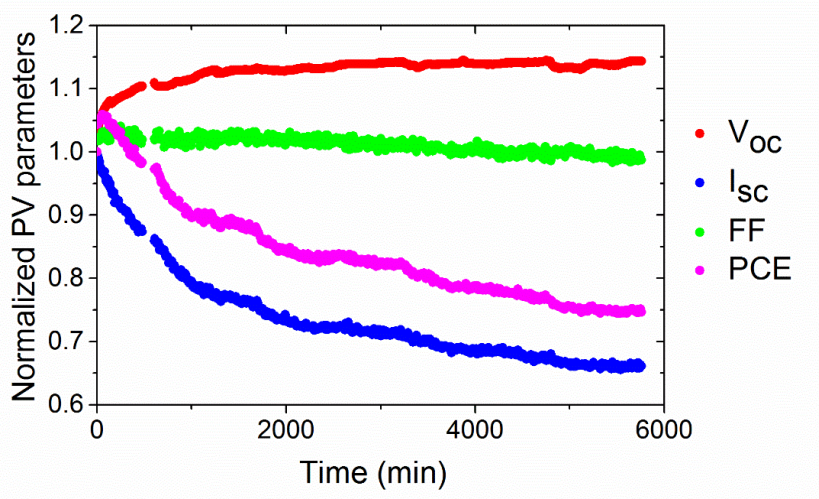

Figure 6.23: Change of Voc, Isc, FF, and PCE during 100 hours of light exposure. Compared with parameter before exposure, the Voc increases by 15%. Isc decreases by 35%. FF is almost the same during exposure. PCE decreases by 25% overall.

As shown in Figure 6.22, the current of the device almost recovers to its initial value when we keep the device in dark condition immediately after the light exposure. However, the Voc suddenly drops below the initial value. Then, during the "recovery" process, which is just keeping the device under dark condition, the Voc will gradually improve and finally reach its initial value. Generally, this recovery process takes about 15 to 24 hours and varies from device to device. After the device recovery, the IV curve is almost the same as the one before exposure.

The recovery process is also temperature dependent. During the recovery process, we keep the device at elevated temperature, and monitor its Voc recovery. The Voc vs. recovery time curve is plotted in Figure 6.24. The initial Voc is placed at -50 minutes just for comparison. Recovery time of 0 minutes is defined as the end of the exposure or the start point of recovery. The inset is the recovery happens in the first 100 minutes. The recovery under 75 ℃ finishes within 25 minutes, which is significant faster than that under 50 ℃ and room temperature.

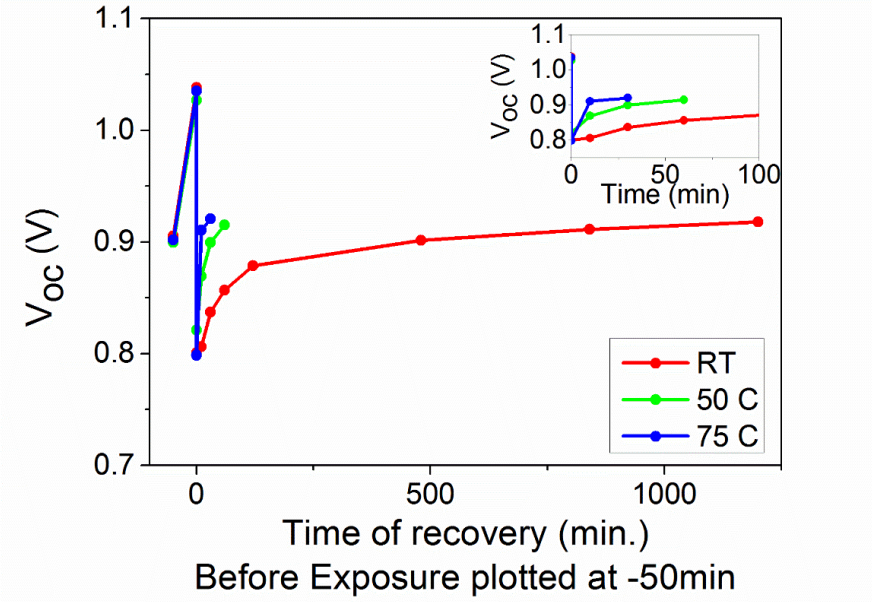

Figure 6.24: Recovery of Voc at different temperature. The Voc recovers faster at higher temperature.

We proposed an ion-generation-migration model to explain our degradation data[102]. The qualitative model is represented in Figure 6.25. Since the formation energy of MA cations and I anions is slow, we should have a large number of positive charged and negative charged ions in perovskite layer at the beginning. Due to the internal electric field, those ions will mostly accumulate on the interfaces between perovskite and transport layers, which is shown in Figure 6.25 (a). As shown in Figure 6.25 (b), those charged ions on the interface will screen part of the internal electrical field and band-bending in the perovskite layer would be slightly less than the one without ions in it. During light exposure, there will be lots of ions generated due to the weak bond of MAI. Since the device is biased under open-circuit condition, there is little electric field in the perovskite layer. Those generated ions and initially accumulated ions on the interface will diffuse back to the bulk of perovskite layer, which is illustrated in Figure 6.25 (c). The absent of interface charge will give rise to the band-bending of perovskite layer in Figure 6.25 (d), and therefore we observe an increase in Voc during exposure. The ions in the bulk of the perovskite layer also act as recombination centers, which results in the reduction of Isc during exposure. After the exposure is finished, the device is kept under dark condition. In this case, the ions in the bulk will again drift towards the interfaces. However, there will be more charges accumulated on the interface this time, which leads to a huge reduction in Voc. The ions on the interfaces are not effective recombination centers since the electric field on the interface is much higher, so the Isc will quickly recover to its initial value. The ion motion and its effect on band-bending are illustrated in Figure 6.25 (e) and (f). The electric field distribution in perovskite solar cell is depicted in Figure 6.26. The electric filed on both interfaces is significant larger than that in the bulk layer, which explains why we can observe Isc increase even there are huge numbers of ions on the interface. Those interface charges will

screen the electric field and lead to a reduction in electric field in the perovskite layer, which would result in less built-in voltage across the main layer.

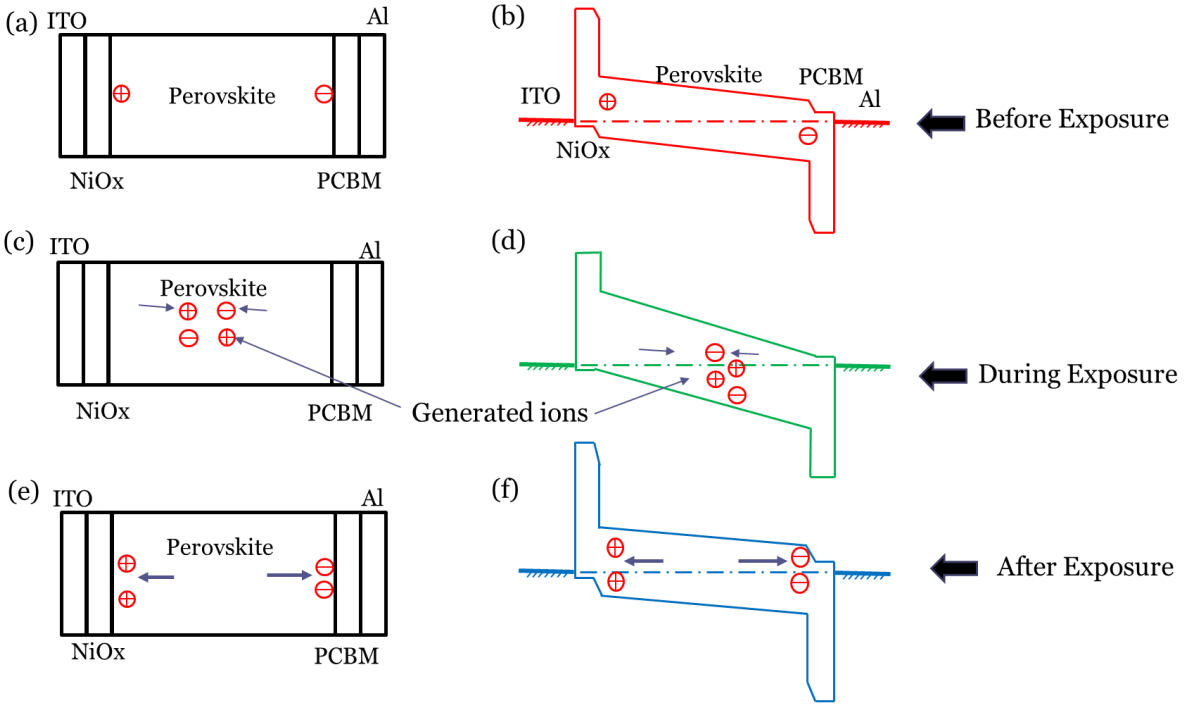

Figure 6.25: Ion-generation-migration model for photon-induced degradation of perovskite solar cell. (a)(c)(e): The motion of ions during and after light exposure. (b)(d)(f): The corresponding change of band diagram during and after exposure.

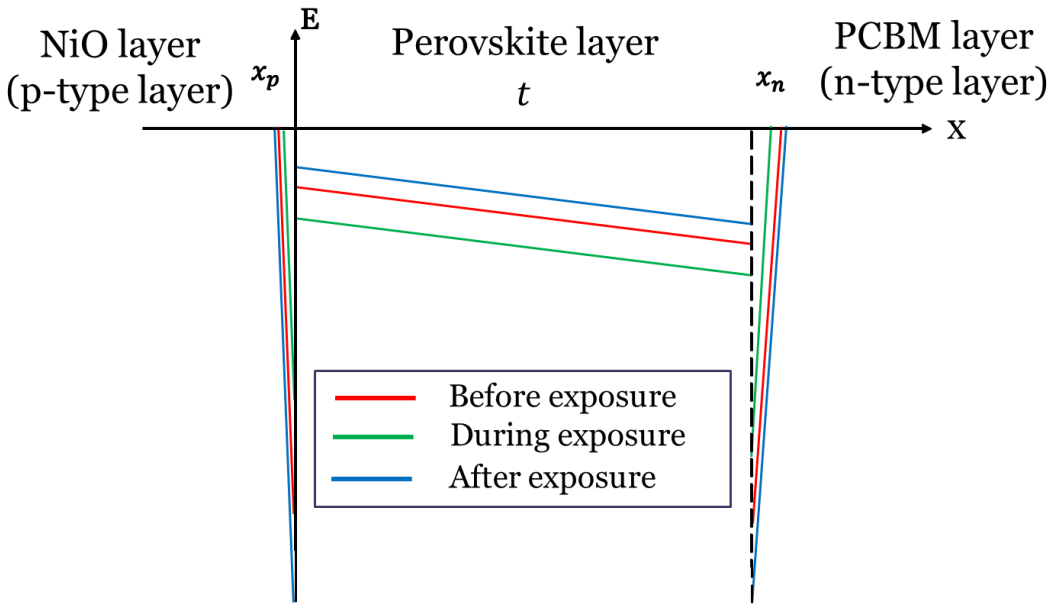

Figure 6.26: Distribution of electric field in perovskite solar cell before, during, and after exposure.

6.4.2 Change of capacitance during and after exposure

Apart from IV measurement, we also monitor the change of capacitance with CV and CF measurement. Figure 6.27 suggests a parallel shift of high frequency (200kHz) CV curve before and after exposure. And after recovery, which is 14 hours after end of exposure, the capacitance almost returns to its initial value. The shift in CV can also be explained with our device model. The capacitance of PN junction can be expressed by Equation (6.1). It depends on both doping concentration N_A and built-in voltage V_0. In our model, there are more ions generated during exposure, and those ions finally accumulate on the interface after exposure, which result in a huge reduction in built-in voltage due to the screening effect. As we see in Equation (6.1), a decrease in V_0 would lead to a left shift of CV curve in x-axis direction, which exactly matches our CV data.

$$C = \frac{\epsilon}{W_d} = \sqrt{\frac{q\epsilon N_A}{2(V_0 - V)}} \tag{6.1}$$

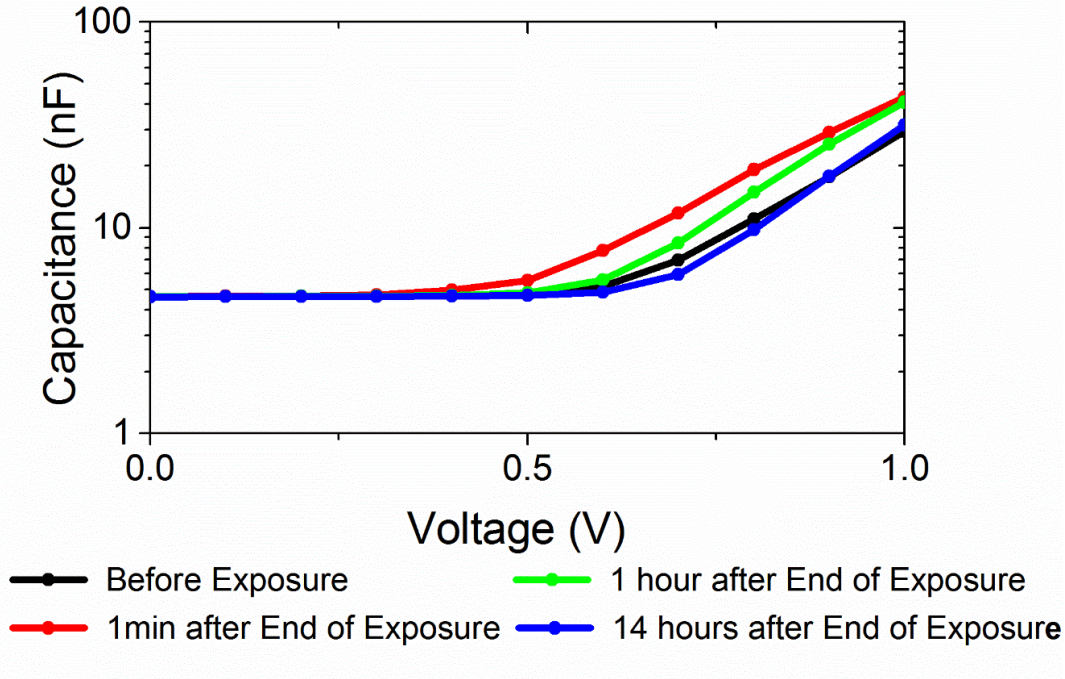

Figure 6.27: Typical change of CV curve of PIN device during degradation and recovery process.

The CF data in Figure 6.28 indicates no DOS change before and after exposure. This is because most of the ions drift towards the interface and accumulated there after exposure, and the ion density in the bulk of perovskite layer would be pretty much the same as it was before the exposure.

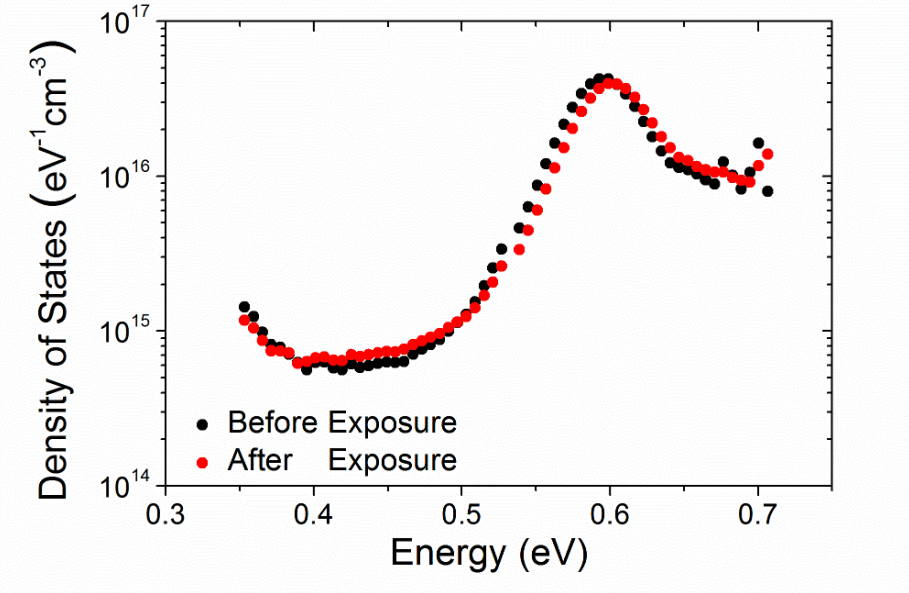

Figure 6.28: DOS before and after exposure.

6.5 Ion Density Measurement

In the previous two sections, we have discussed how perovskite device changes during exposure and recovery process, and we find out the device degradation and recovery originate from the generation and migration of ions. We also proposed a qualitative model to explain the change in IV and capacitance during and after exposure.

In order to further understand the degradation and recovery process of perovskite solar cell, quantitative perspective of ion density before and after exposure is needed.

Figure 6.29 depicts the change of dark IV during exposure and recovery. After exposure, we observe a relatively large negative current at 0 V in the dark IV curve (red curve in Figure 6.29). During the recovery process, this negative current will gradually decrease and finally return to the initial value after 14 hours of recovery, and the dark IV after recovery is exactly the same as the one before exposure.

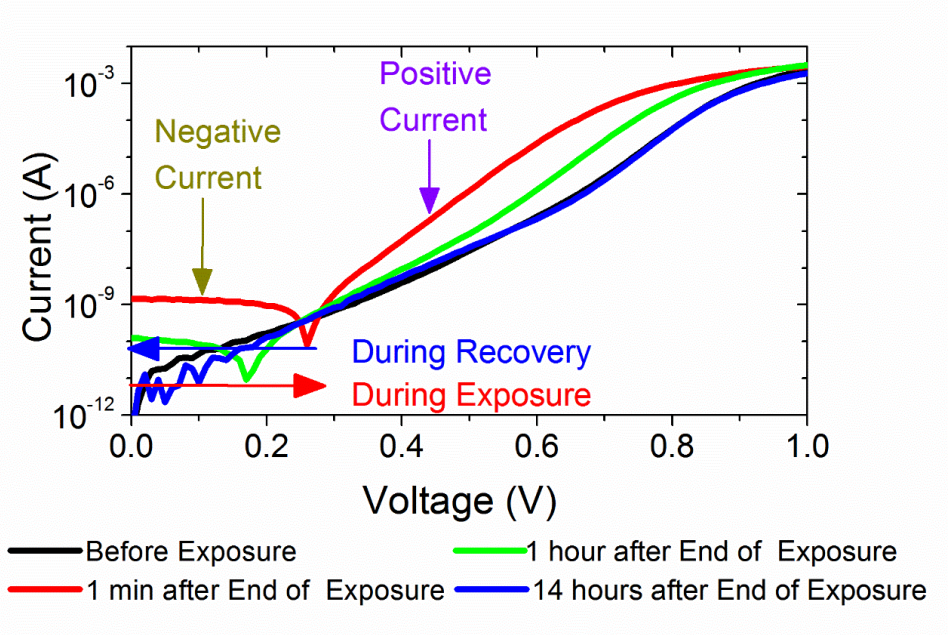

Figure 6.29: Change of dark IV during exposure and recovery.

The existence and diminution of this current can also be explained by our model. In Figure 6.30 (a), there exist large numbers of ions in the bulk of the perovskite, most of which are generated during light exposure. As soon as we keep the device under dark, there will be an internal electric field which will push those charges to the interface of the device, as shown in Figure 6.30 (b). The movement of those charges will induce a displacement current, which is in a negative sign.

If we monitor the change of this ionic displacement current, we can use it to calculate the number of ions in the perovskite. The total number of ions can be express as follows.

$$\mathrm{N}_i = \frac{Q_i}{q} = \frac{\int I(t)dt}{q} \tag{6.2}$$

Here, $I(t)$ is the transient displacement current over time. Q_i is total amount of ion charge.

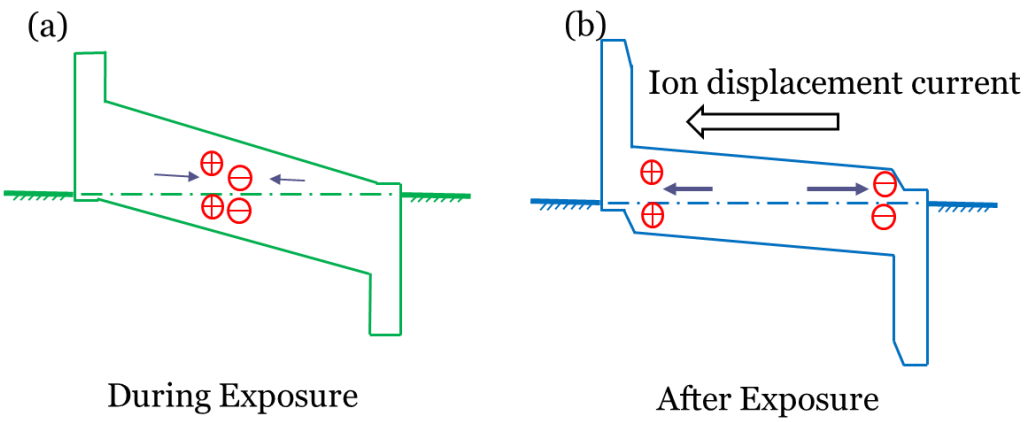

Figure 6.30: Migration of ion in perovskite layer will induce a displacement current, which can be utilized to calculate ion concentration. (a) ion distribution during exposure (b) ion distribution after exposure.

The typical transient current before and after exposure is provided in Figure 6.31. This is measured on a device without adding excess PbI_2 during fabrication process. The effect of excess PbI_2 will be discussed in the following section. Transient ionic current is much larger after 96 hours of 1-sun exposure. The calculated ion density before exposure is 7.4E17/cm^3 and the one after exposure is 3.9E18/cm^3, which is over 50 times higher. This matches our model that most of the ions in the perovskite after exposure are generated during light exposure. Those ions are mostly generated due to the bond breaking of MAI.

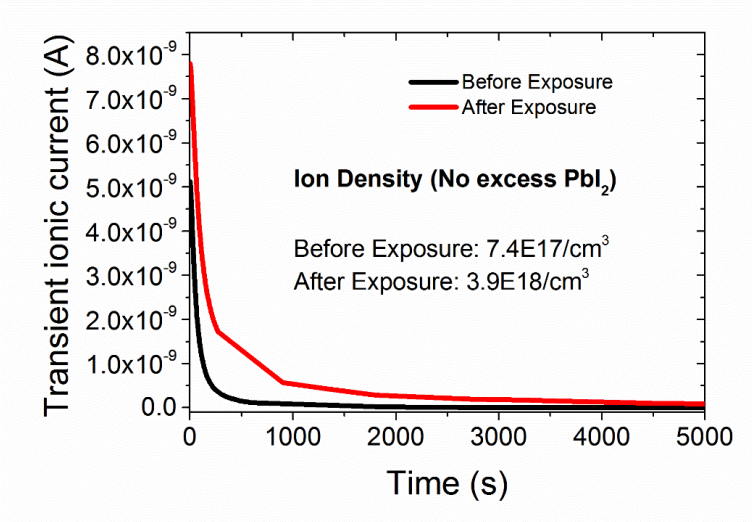

Figure 6.31: Typical transient current vs. time before and after exposure for device without excess PbI_2.

The generation of ions also depends on the light intensity and exposure time. We did exposure on three contacts of same sample with different exposure parameters. The first device was exposed at 1-sun intensity for 96 hours. The second one was exposed at 2X sun intensity for 20 hours. And the third one was exposed at 4X sun intensity for 48 hours. The transient ionic current in the first 5000s after exposure is illustrated in Figure 6.32. The one exposed at 4X sun intensity shows much higher displacement current than the others. The ion density calculated from the transient current is also displayed in Figure 6.32. The ion density after exposure are all in the order of $10^{18}/cm^3$.

If we plot Jsc vs. its corresponding ion density before and after exposure, we will observe a linear relationship between current density loss and generated ion density, which is shown in Figure 6.33. With higher ion density, we observe higher current density loss, which indicates the role as recombination centers of those ions.

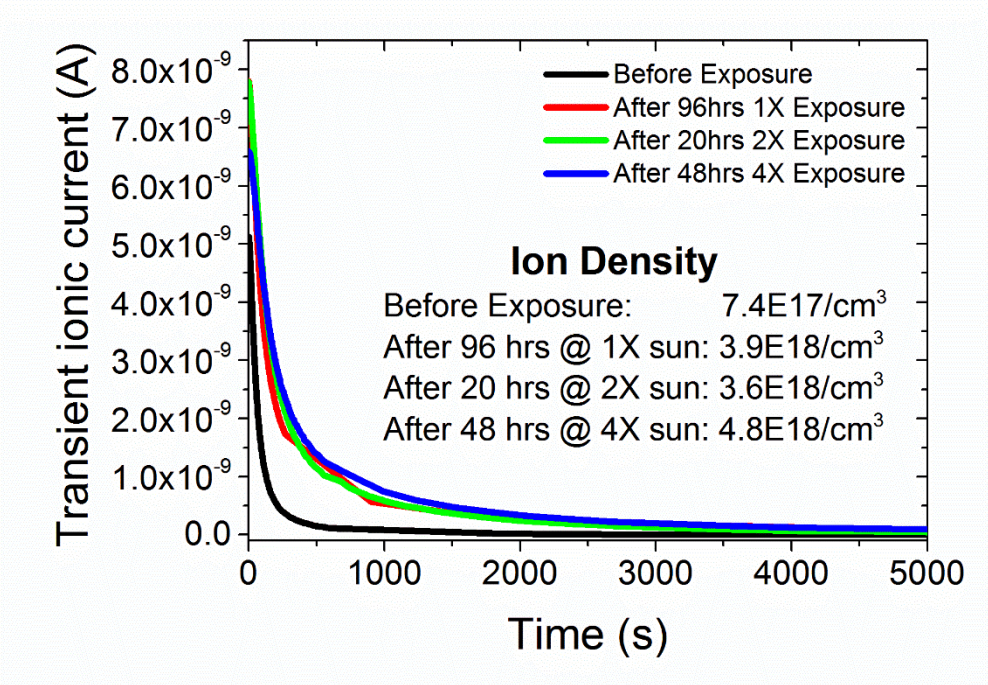

Figure 6.32: Transient ionic current vs. time. Device under exposed by longer time and higher light intensity shows larger transient current, which indicates the ion generation is proportional to the light intensity as well as exposure time.

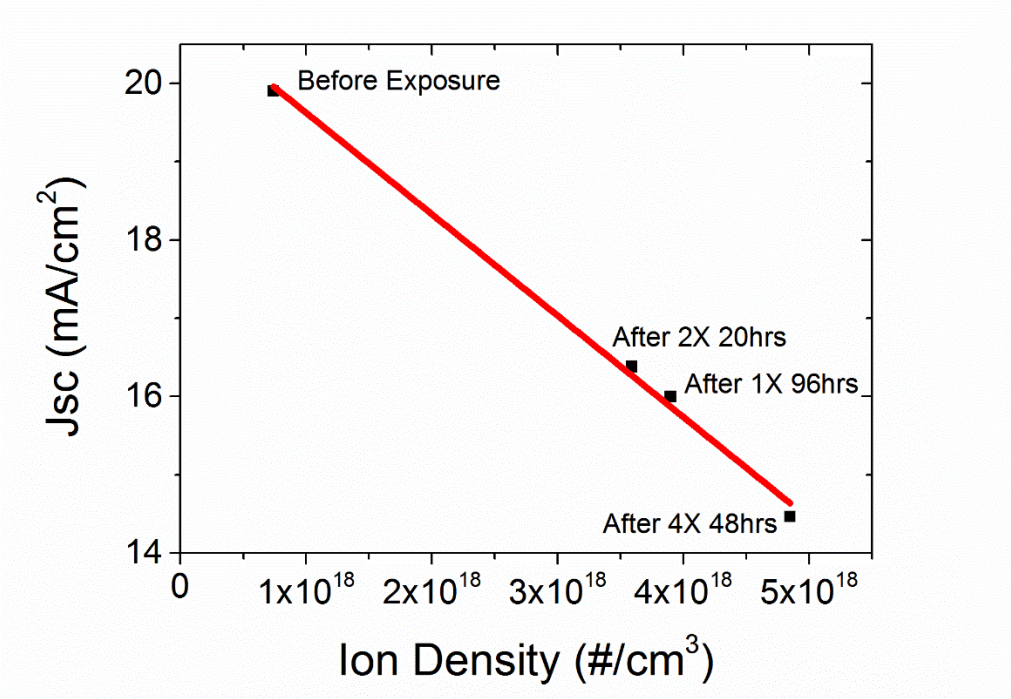

Figure 6.33: Jsc vs. Ion density before and after exposure at different exposure conditions.

6.6 Degradation mitigation

Now we have understood that the photon-induced degradation process of perovskite solar cell is driven by the generation and migration of ions. The next question would be what can we do to mitigate this type of degradation?

6.6.1 Effect of grain size

In order to mitigate photon-induced degradation, we have to know the location of ion generation to slow down the ion generation process, which is the source of device degradation. In this case, by retarding the ion generation in that area, we can effectively improve the device stability.

The MA cations and I anions are generated when there is bond breaking in MAI. Since most of the dangling bonds exist on the grain boundaries in thin film perovskite, we suspect that that is the place where most of the ions are generated.

To prove this hypothesis, we made two types of samples: One with larger grains and one with smaller grains. With bigger grains, the perovskite film would have less grain boundaries and is expected to have better stability. The film with larger grains is made with solvent annealing treatment, and the other one is not. The device structure of both devices is ITO/NiO/Perovskite/PCBM/Al.

Figure 6.34 (c) and (d) are the SEM images of device without solvent annealing and one with solvent annealing. After solvent annealing, the grain size of the perovskite increases from around 400nm to more than 1μm. The IV curves of both devices are shown in Figure 6.34 (a). Two devices have similar performance. The one with solvent annealing has a power conversion efficiency of 15.8% while the one without has 15.2%. QE is provided in Figure 6.34 (b).

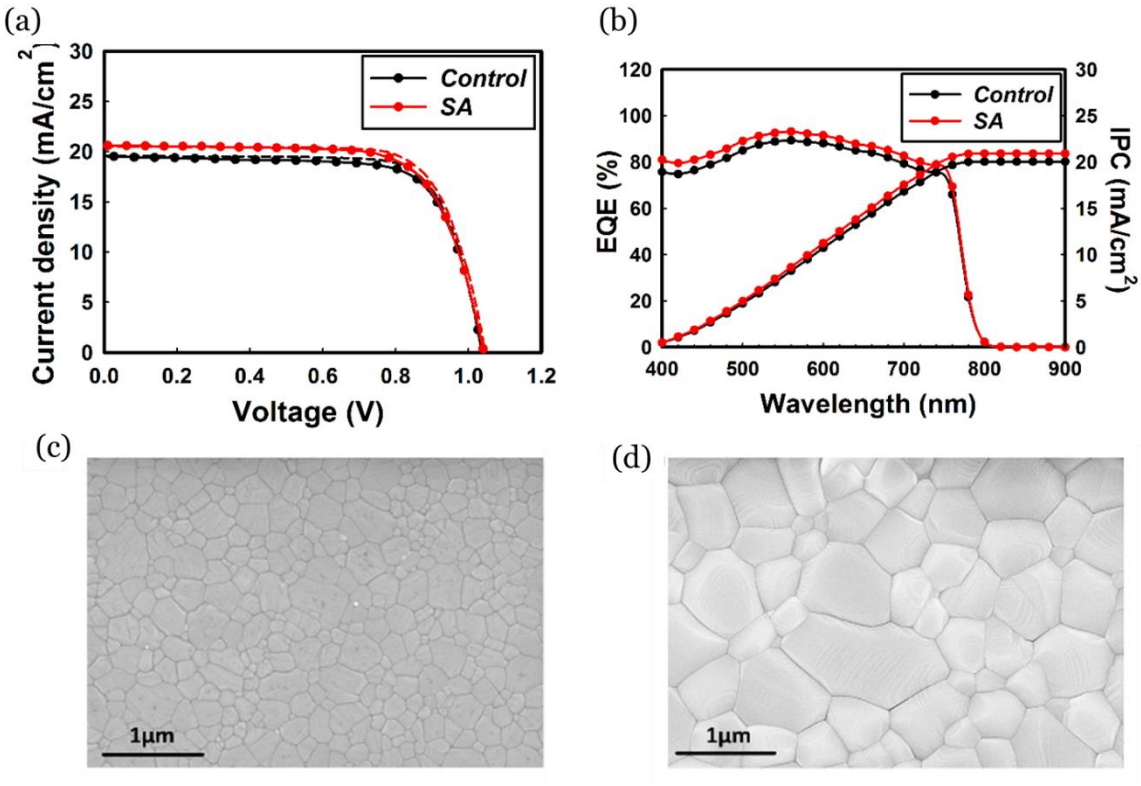

Figure 6.34: (a) IV of control sample and sample with solvent annealing. None of them shows hysteresis. (b) QE of both sample. (c)(d) SEM of sample without and with solvent annealing, respectively.

Both devices are kept at open-circuit condition during the exposure, and the detailed performance degradation is shown in Figure 6.35. The one with bigger grain size (solvent-annealed device) has less degradation in all the parameters, especially in Jsc. The Jsc of solvent-annealed device only decease by 6%, which is less than half of the Jsc reduction in the one without solvent annealing. This means the generation of ions is much slower if the grain size is bigger, which is also proved by ion density measurement in Figure 6.36. Figure 6.36 (a) represents the transient ionic current of both devices before exposure while Figure 6.36 (b) shows the one after exposure. In both cases, the ion density of solvent-annealed device is lower than that of device without solvent annealing.

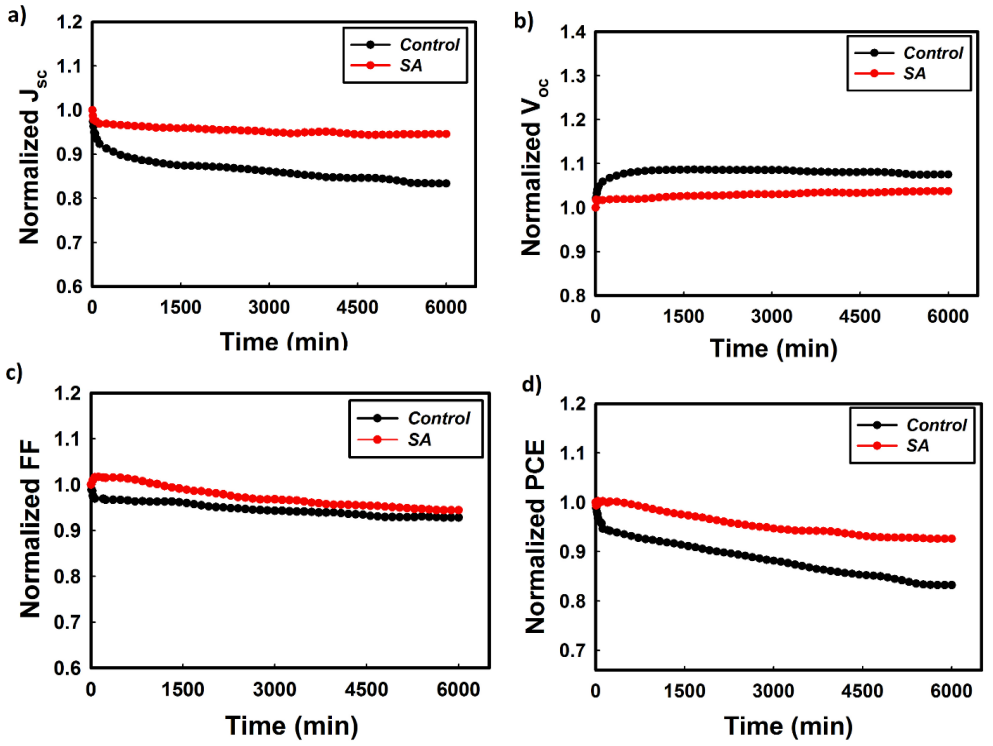

Figure 6.35: Detailed performance degradation trend of device with and without solvent annealing.

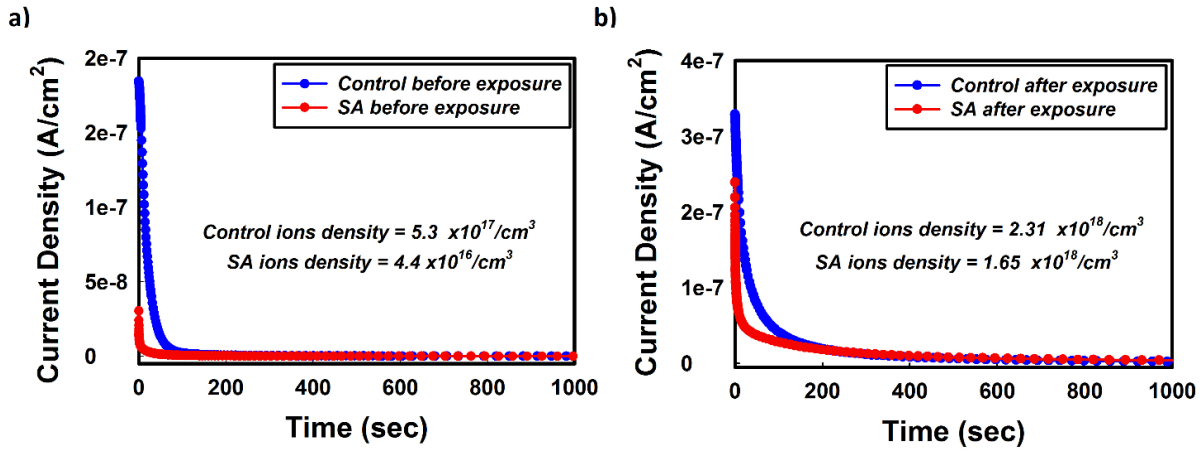

Figure 6.36: (a)Transient ionic current of control device and solvent-annealed device before degradation. (b) Transient ionic current of control device and solvent-annealed device after degradation.

If we plot the Jsc vs. ion density, we can also observe a linear relation between the two.

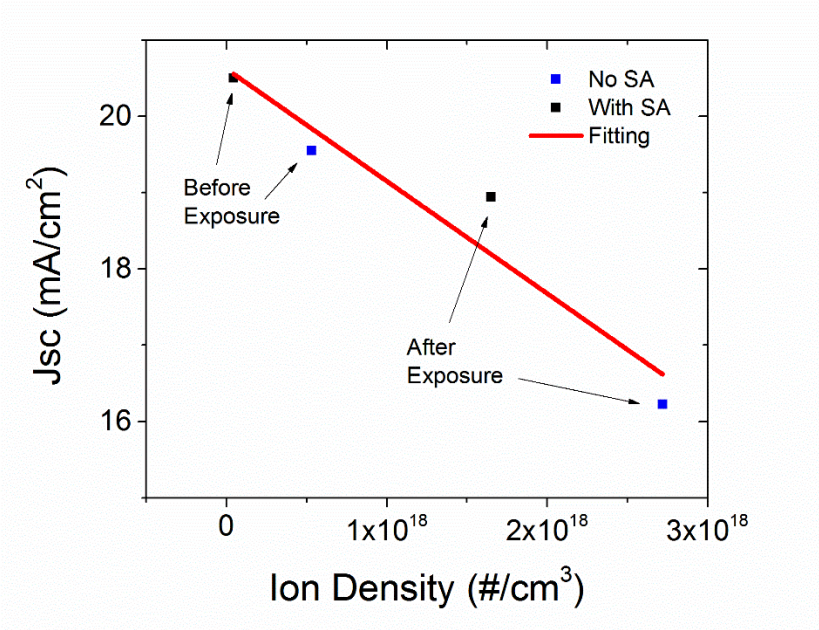

Figure 6.37: Ion density vs. Jsc of control device and solvent-annealed device before and after degradation.

6.6.2 Effect of excess PbI_2

Another method we proposed to reduce the ion generation is adding excess PbI_2 in the perovskite layer. There exists an equilibrium between the degradation and formation of perovskite, which is shown as follows.

$$MAPbI_3 \leftrightarrow MA^+ + I^- + PbI_2$$

During degradation, perovskite can be decomposed to PbI_2 and MAI, and MAI will be further decomposed to MA cation and I anion. This decomposition is also reversible, which is simple a formation process. Finally, the degradation and formation process are stabilized under equilibrium, and about 0.01% to 0.1% of the perovskite degrades and generates MA

cations and I anions according to our ion density calculation. So, adding 6% of excess PbI_2 is expected to significantly push the equilibrium to the left and reduce the ion density.

In this study, we made two types of PIN perovskite devices. One of them adds 6% of excess PbI_2 in the perovskite solution during the perovskite fabrication. The other one is a standard process without adding excess PbI_2. The device structure of both devices is ITO/NiO/Perovskite/PCBM/Al.

The IV curve in Figure 6.38 shows that the device with excess PbI_2 has much higher Voc. According to the detailed IV parameter in Table 6-3, the most significant difference between the device with excess PbI_2 and the one without is Voc; by adding 6% excess PbI_2, the Voc of the device increases from 0.94V to 1.05V, improving the efficiency from 13.1% to 14.6%.

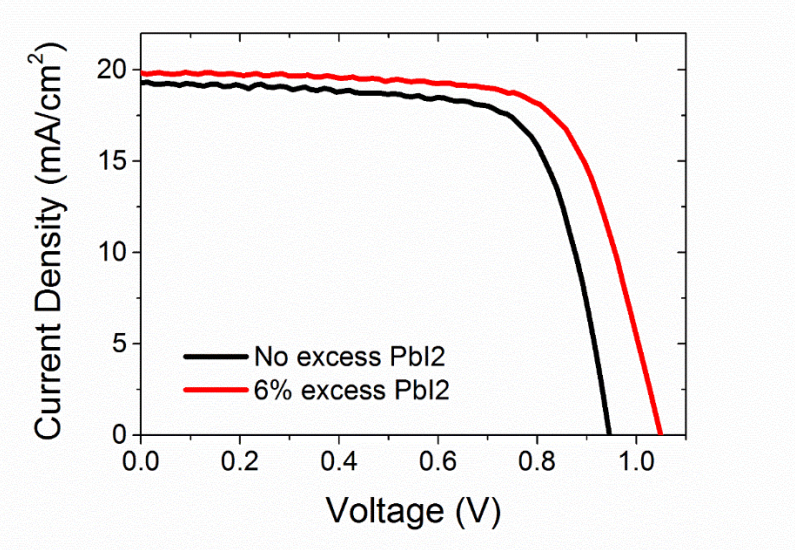

Figure 6.38: IV curves of PIN perovskite device with and without 6% excess PbI_2.

Table 6-3: Detailed device performance of perovskite device with and without 6% PbI_2.

	V_{oc}	J_{sc}	FF	PCE
Standard	0.94 V	19.3 mA/cm^2	72%	13.1%
6% excess	1.05 V	19.8 mA/cm^2	70%	14.6%

We did Sub-gap QE and DOS measurement to see whether this improvement of Voc is attributed to the change of tail states density and mid-gap states density. In a-Si and organic solar cells, the change in Voc is mostly due to the change in defect density, which will lead to a change in diode saturation current I_o. From Chapter 3.2.2, we know that the Voc of the device can be expressed as the following equation.

$$V_{oc} = \frac{nkT}{q} \ln\left(\frac{I_L}{I_o}\right) \tag{6.3}$$

Here, n is the overall ideality factor, and it is normally between 1 to 2. I_L is the generated photo-current. I_o is the diode saturation current, which is controlled by defect density. If there is a notable reduction in defect density, which would lead to a decrease in I_o, we will observe a corresponding increase in Voc.

However, in Figure 6.39, there is no significant difference in the density of tail states and mid-gap states between those two devices. The DOS measurement result in Figure 6.40 also gives the same conclusion: there is no change in mid-gap defect density after adding excess PbI_2.

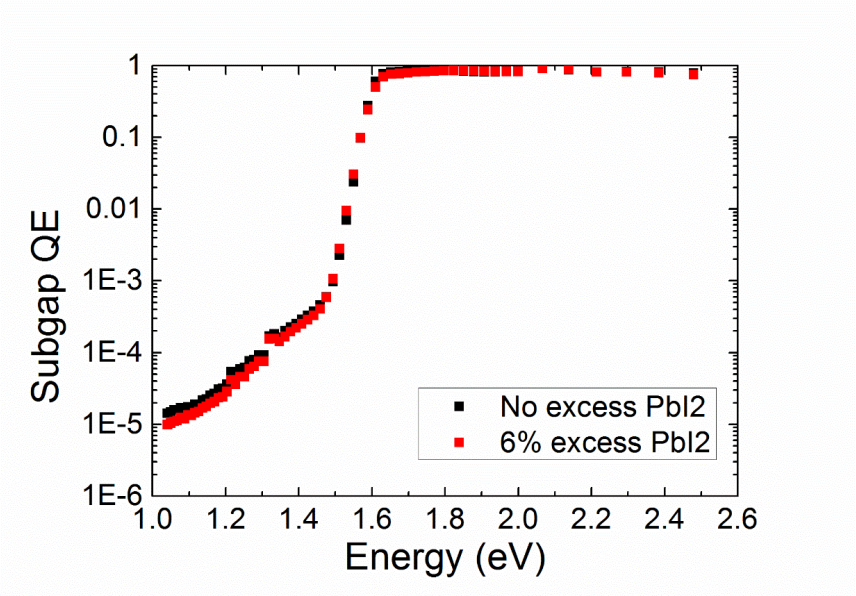

Figure 6.39: Subgap QE of devices with and without 6% excess PbI_2. No significant difference is observed in tail states and mid-gap states.

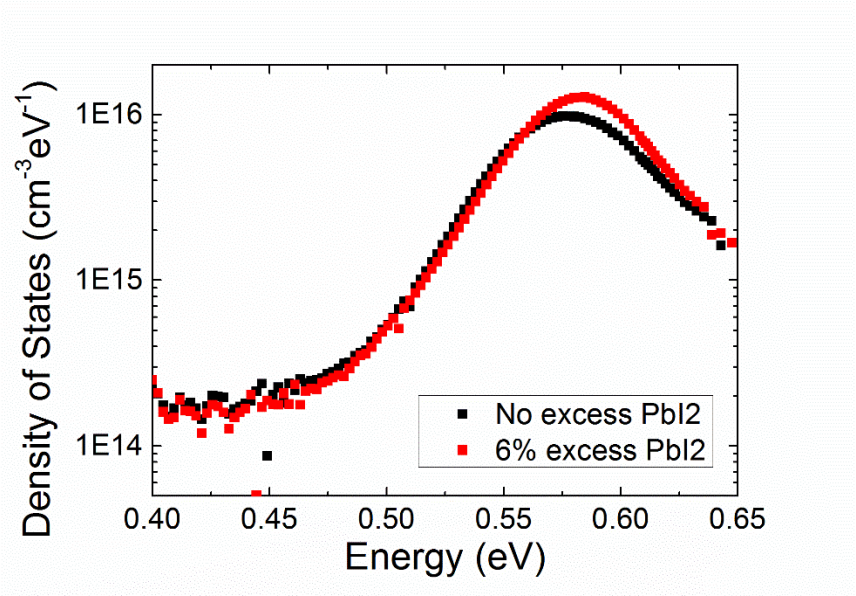

Figure 6.40: DOS of devices with and without 6% excess PbI_2. There is no change in mid-gap states after adding excess PbI_2.

The change in Voc here can be explained by the ion migration model. Since the ions in the perovskite layer originate from the decomposition of only 0.01% of perovskite, adding 6% of excess PbI_2 will significantly push the reaction equilibrium to the left and lead to a reduction

in ion density. Because of the reduction of ion density on the interface, the built-in voltage in perovskite will be improved with less electric field screening. The ion density measurement result in Figure 6.41 confirms our model; by adding 6% excess PbI_2, ion density is reduced by almost 10 times.

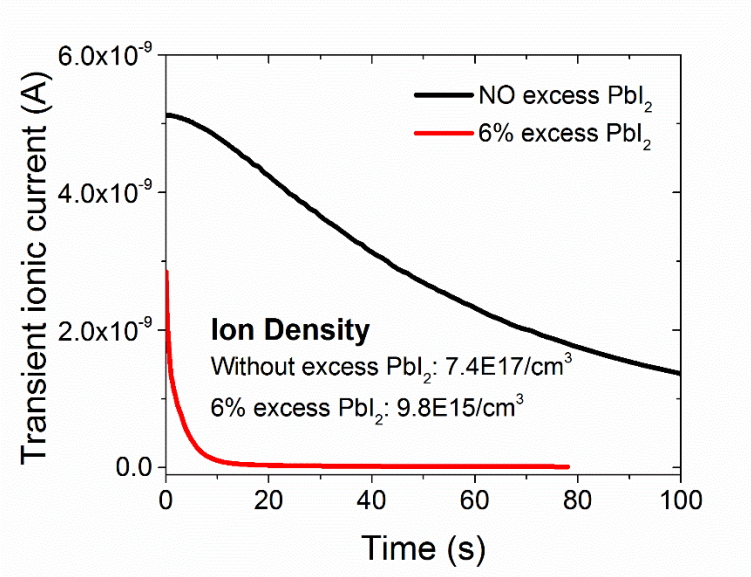

Figure 6.41: Transient ionic current of device with and without 6% excess PbI_2. The one with excess PbI_2 has significant less ions.

We further did the photo-induced degradation study on those two samples. The performance degradation trend of them are shown in Figure 6.42. Voc of both device increased during 96 hours of light exposure; the device with excess PbI_2 has slightly less change. Most of the difference between those two devices is the decrease of Isc. By adding 6% excess PbI_2, the Isc decreases by only 18% instead of 35%, which indicates significantly retard of perovskite degradation. If we look at the ion density data in Figure 6.43, ion density of the device with excess PbI_2 after exposure is 5E17/cm^3, which is 80 times less than that of device without excess PbI_2. The side by side comparison of transient current and ion density of those two devices before and after exposure is provided in Figure 6.44.

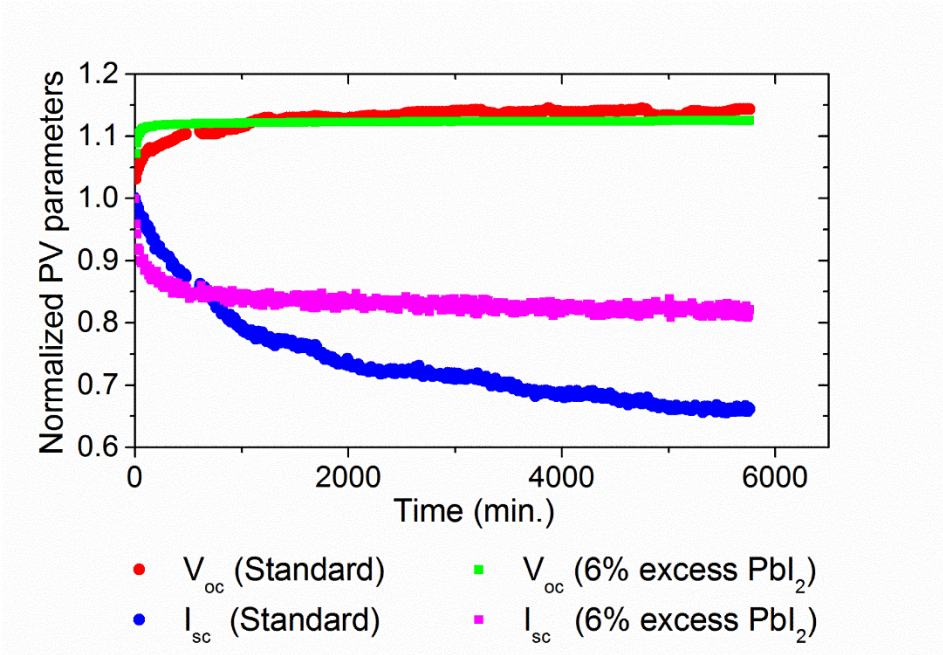

Figure 6.42: Performance degradation trend of devices with and without 6% excess PbI_2. The one with excess PbI_2 has less change in Voc and Isc.

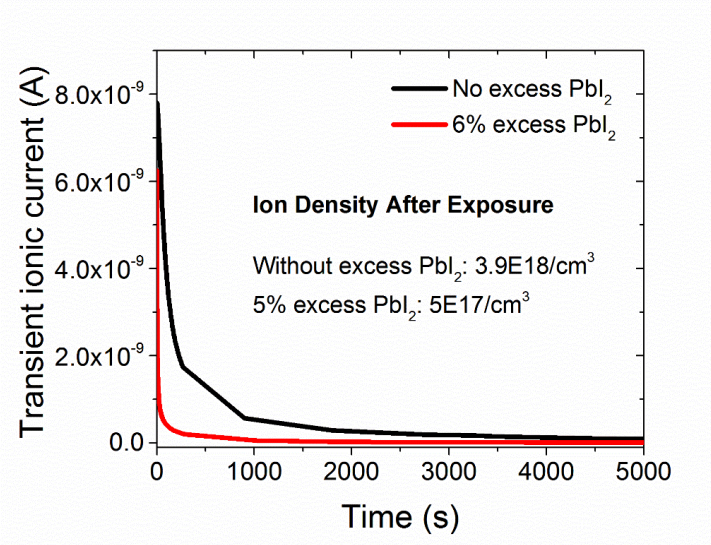

Figure 6.43: Transient ionic current of devices with and without 6% excess PbI_2 after exposure. The one with excess PbI_2 has less ions generated.

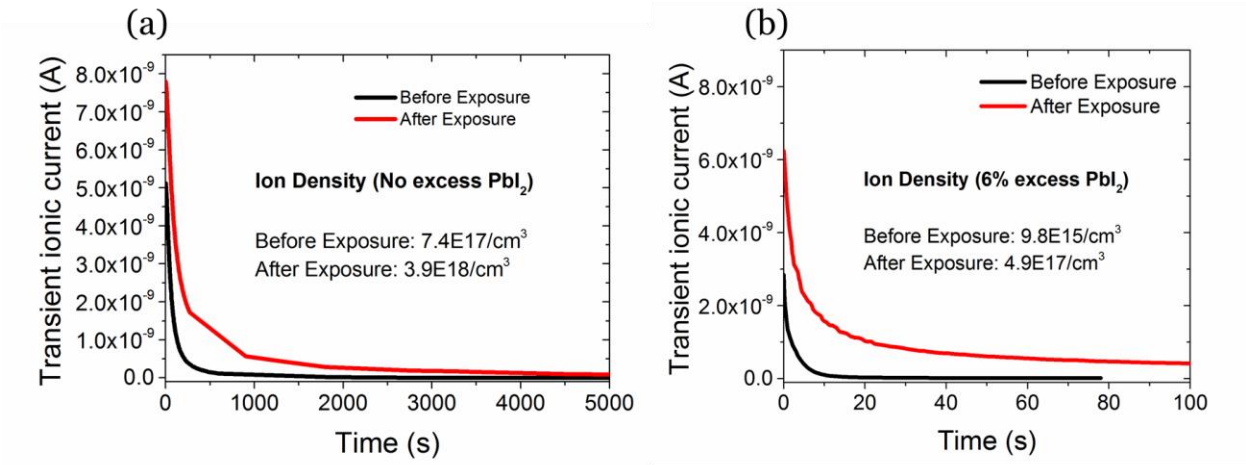

Figure 6.44: Ion density before and after exposure of devices with and without 6% excess PbI_2.

In this chapter, we have proposed an ion-generation-migration model to explain the degradation process of perovskite. Qualitative and quantitative understanding of degradation process is provided and lead to two approaches to mitigate the degradation. By increasing the grain size or adding excess PbI_2, we are able to retard the degradation (ion generation) by 50% respectively.

CHAPTER 7

CONCLUSION AND FUTURE WORK

In this work, we have explored the basic electronic and optical material properties of perovskite. We have performed systematic process and device optimization based on our understanding of this material and developed a 16% perovskite solar cell with standard structure and a 14% cell with bifacial structure. Finally, we studied the physics of photon induced degradation of perovskite solar cell and proposed a device model to explain the degradation and recovery process based on the generation and migration of ions. We also provided two approaches to mitigate this type of degradation by increasing the grain size and adding excess PbI_2.

7.1 Conclusion

7.1.1 Perovskite solar cells

- Systematic process optimization has been performed, and a PIN solution process was developed with device efficiency over 16%.
- We developed solvent annealing process on our PIN solution process, which significantly enhanced the grain size from 200 nm to 1 µm.
- By adding 6% excess PbI_2, we improved the V_{oc} of our solution processed device from 0.94 V to 1.05 V. Subgap QE, CF, and ion density measurement have been performed to investigate the device physics of device with excess PbI_2; improvement of V_{oc} was found to originate from the reduction of ion density.
- We studied the electronic defects distribution of perovskite by using sub-gap QE and CFT measurement, and two distinct mid-gap state bands were discovered.

- We measured the dark IV of our PIN solution device and found that it perfectly fits the two-diode model.
- We made a hole-only device sandwiched by NiO and P3HT and found that the dark current was proportional to V^2, which indicated that our perovskite was p-type doped.
- We performed photoconductivity measurement, and the diffusion length of our perovskite was found to be around 4 μm under the assumption that the mobility of electrons and holes was almost the same.

7.1.2 Bifacial perovskite solar cell

- We developed a room-temperature ZnO:Al RF sputtering process, and it provided exactly the same film transmission when compared with our standard 150℃ sputtering process.
- By carefully considering the material property of perovskite and electron-transport layer on top, a bifacial perovskite solar cell was successfully developed by adding CdS layer between perovskite and ZnO:Al as a buffer layer. After device optimization, we achieved 14% efficiency with light coming from the top (ZnO:Al side), which was one of best efficiency in the field.
- The bifacial PIN device possesses great environmental stability and it does not degrade after being kept in air for 3 months. With a controlled experiment, we found that it was the ZnO:Al layer that provided excellent encapsulation for perovskite solar cell.

- We performed QE vs. bias measurement on both sides of our bifacial perovskite solar cell to measure the diffusion length of both electrons and holes. We also built a model considering the interface region with low diffusion length. The diffusion lengths of electrons and holes in the bulk region of perovskite were calculated to be 7 and 4.7 μm respectively, and the diffusion lengths of electrons and holes near the interface were found to be 1.8 μm and 370 nm.

7.1.3 Photon induced degradation of perovskite solar cell

- Detailed device analysis on our PIN perovskite solar cell during light exposure was performed, and we found that the degradation of device originated from the generation and migration of ions.
- We performed ion density measurement of perovskite by using transient dark current. The measurement data showed a linear relationship between the reduction of photo-current and generation of ions.
- The effect of gain size on photon induced degradation was investigated. By increasing the grain size from 400nm to 1μm, we observed a huge decrease in ion density before and after degradation, which led to 50% less degradation. We also did ion density measurement on both devices and found the one with larger grain size has less ion density before and after exposure. This experiment demonstrated that most of ions were generated on the grain boundaries.
- We studied the effect of excess PbI_2 on device degradation. By adding 6% excess PbI_2, we found that the ion density of perovskite was reduced by 80 times. With

less amount of ion charge, we observed 50% less photo-current degradation of the sample with excess PbI_2.

7.2 Future Work

7.2.1 Device physics behind cesium enhanced perovskite photo-stability

Gratzel and co-workers improved the efficiency of mixed cation perovskite to over 20% by incorporating 5% cesium during fabrication, which is show in Figure 7.1 (a). Meanwhile, as shown in Figure 7.1 (b), they also found that photo-stability of the device with cesium was significantly enhanced[45]. However, detailed material and device analysis was not provided to explain the enhancement of photo-stability. Another concern of their photo-stability study is that the light source they used is a LED light, which lacks UV and infrared spectrum.

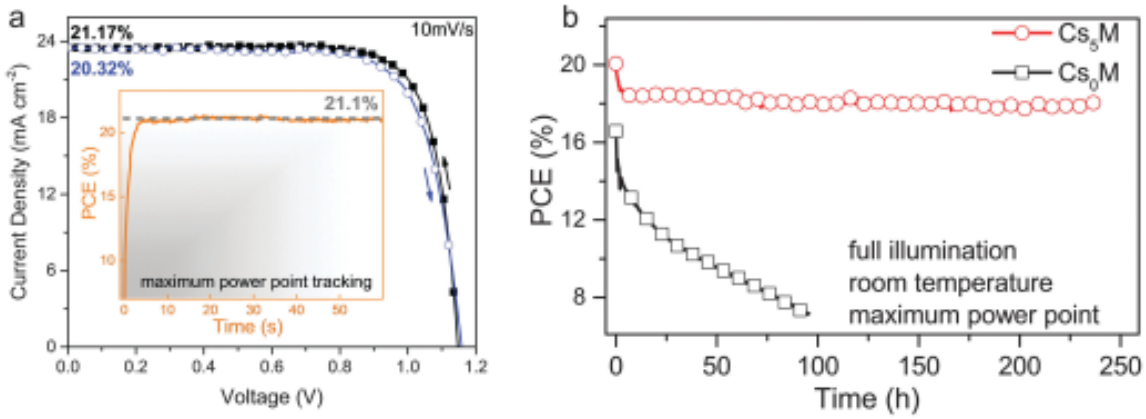

Figure 7.1: (a) IV hysteresis of the champion cell shows device efficiency over 21%. (b) Device with 5% cesium has much better photo-stability[45].

So, full-spectrum degradation study is necessary in order to explore the role of cesium in enhancing the photo-stability. We also need to do a complete device characterization of the device before and after degradation to understand what happens during the exposure. Ion

density should also be measured to see whether this improvement in photo-stability also results from the reduction of ion generation like what we see in $MAPbI_3$ perovskite.

7.2.2 Further study of the effect of excess PbI_2 on photo-stability

In Chapter 6.6.2, I have investigated the effect of excess PbI_2 on device performance and its degradation process. What we found was the perovskite device contained less ions after adding 6% excess PbI_2, which led to less interface ion charge and higher Voc. By adding excess PbI_2, the generation of MA^+ and I^- ion will get slowed during exposure and result in better device stability under light. However, the amount of excess PbI_2 I referred to was that in the solution. We should perform EDS on our perovskite film to see how much excess PbI_2 is finally introduced, which could differ from what in the perovskite solution. Meanwhile, we should also study how different amount of excess PbI_2 would affect the device performance and photo-stability. 2%, 4%, 6%, 8%, and 10% of excess PbI_2 could be introduced in the perovskite film, and their corresponding device performance and photo-stability can be studied.

7.2.3 Relation between ion density and open-circuit voltage

We have measured the ion density of perovskite using transient dark current and investigated the relation between ion density and short-circuit current. In our degradation model, we found that open-circuit voltage changes with the ion density on the interface. Since Voc and Isc are the two parameters that change during light exposure. Understanding the relation between Voc and ion density is critical for us to explain and predict the change of device performance during and after the exposure. Since the reduction of Voc after exposure results from the screening effect of interface ion charge, we can use CV measurement to

monitor the change of built-in voltage, which would be a function of ion density. Almora et al. introduced a method to calculate ion density from capacitance by considering the ionic Debye length[87]. However, according to their model, the potential drop due to ion charge would be kT/q, which is independent of ion density. So, an appropriate device model is needed to bridge the interface ion density and potential drop of the perovskite layer.

REFERENCE

1 BP, "Statistical review of world energy", (London, 2016).

2 C. H. Sang, S. J. Chou, F. M. Pan, and J. T. Sheu, "Fluorescence enhancement and multiple protein detection in zno nanostructure microfluidic devices", Biosens Bioelectron, **75**, 285 (2016). doi:10.1016/j.bios.2015.08.050

3 J. Tsao, N. Lewis, and G. Crabtree, "Solar faqs", (Sandia National Laboratory, 2006).

4 M. Ramn and N. S. Negi, "Effect of (fe, co) co-doping on the structural, electrical and magnetic properties of zno nanocrystals prepared by solution combustion method", Physica B, **481**, 185 (2016). doi:10.1016/j.physb.2015.11.014

5 "Time to switch on to alternative energy", (http://zafarson.com/services/solar-panels/).

6 "Musk's cousins battle utilities to make solar rooftops cheap", (https://www.bloomberg.com/news/articles/2015-04-15/elon-musk-s-cousins-battle-utilities-to-make-solar-rooftops-cheap).

7 "Growth of photovoltaics", (https://en.wikipedia.org/wiki/Growth_of_photovoltaics).

8 "Levelized cost and levelized avoided cost of new generation resources in the annual energy outlook 2015", (US Energy Information Administration (EIA), 2015).

9 R. Fu, D. Chung, T. Lowder, D. Feldman, K. Ardani, and R. Margolis, "U.S. Solar photovoltaic system cost benchmark: Q1 2016", (National Renewable Energy Laboratory (NREL), 2016).

10 "Sunshot vison study", (U.S. Department of Energy, 2012).

11 J. I. Pankove, *Optical processes in semiconductors*. (Dover Publications, New York, 1971).

12 F. Urbach, "The long-wavelength edge of photographic sensitivity and of the electronic absorption of solids", Phys. Rev., **92**, 1324 (1953). doi:10.1103/PhysRev.92.1324

13 R. F. Pierret, *Advanced semiconductor fundamentals*. (Addison-Wesley Publishing Company, Reading, 1987).

14 B. G. Streetman and S. K. Banerjee, *Solid state electronic devices*. (Pearson Education, New Jersey, 2006), 6 ed.

15 A. L. Fahrenbruch and R. H. Bube, *Fundamentals of solar cells*. (Academic Press, New York, 1983).

16 A. McEvoy, L. Castaner, and T. Markvart, *Solar cells: Materials, manufacture and operation*. (Academic Press, 2012), 2 ed.

17 R. A. Smith, *Semiconductors*. (Cambridge Univeristy Press, London and New York, 1968).

18 W. Shockley and H. J. Queisser, " Detailed balance limit of efficiency of p-n junction solar cells", J. Appl. Phys., **32**, 510 (1961). doi:10.1063/1.1736034

19 Adopted from https://en.wikipedia.org/wiki/Shockley%E2%80%93Queisser_limit.

20 Adopted from http://www.pveducation.org/pvcdrom/solar-cell-operation/fill-factor.

21 Adoped from https://ecee.colorado.edu/~bart/book/book/chapter4/ch4_4.htm.

22 M. Samiee, PhD Dissertation, Iowa State University, 2015.

23 Adoped from http://www.pveducation.org/pvcdrom/solar-cell-operation/quantum-efficiency.

24 E. A. Davis and N. F. Mott, "Conduction in non-crystalline systems v. Conductivity, optical absorption and photoconductivity in amorphous semiconductors", Phil. Mag., **22**, 903 (1970).

25 V. L. Dalal and P. Sharma, "Defect density and diffusion length of holes in nanocrystalline silicon devices", Appl. Phys. Lett., **86**, 103510 (2005). doi:10.1063/1.1873062

26 L. C. Kimerling, "Influence of deep traps on the measurement of free-carrier distributions in semiconductors by junction capacitance techniques", J. Appl. Phys., **45**, 1839 (1974). doi:10.1063/1.1663500

27 T. Walter, R. Herberholz, C. Müller, and H. W. Schock, "Determination of defect distributions from admittance measurements and application to cu(in,ga)se2 based heterojunctions", J. Appl. Phys., **80**, 4411 (1996). doi:10.1063/1.363401

28 D. K. Schroder, *Semiconductor material and device characterization*. (Wiley-IEEE Press, New York, 2015), 3 ed.

29 D. Basu, PhD Dissertation, University of Texas at Austin, 2007.

30 W. B. Leigh, *Devices for optoelectronics*. (CRC Press, Boca Raton, 1996).

31 J. A. Carr, PhD Dissertation, Iowa State University, 2014.

32 M. A. Green, A. Ho-Baillie, and H. J. Snaith, "The emergence of perovskite solar cells", Nat. Photonics, **8**, 506 (2014). doi:10.1038/nphoton.2014.134

33 C. Li, X. Lu, W. Ding, L. Feng, Y. Gao, and Z. Guo, "Formability of abx3 (x = f, cl, br, i) halide perovskites", Acta Crystallogr B, **64**, 702 (2008). doi:10.1107/S0108768108032734

34 H. Topsöe, "Krystallographisch-chemische untersuchungen homologer verbindungen", Zeitschrif für Kristallographie, **8**, 246 (1884).

35 D. B. Mitzi, S. Wang, C. A. Feild, C. A. Chess, and A. M. Guloy, "Conducting layered organic–inorganic halides containing <110>-oriented perovskite sheets", Science, **267**, 1473 (1995).

36 D. B.Mitzi, K. Chondroudis, and C. R. Kagan, "Organic-inorganic electronics", IBM J. Res. Dev., **45**, 29 (2001).

37 A. Kojima, K. Teshima, T. Miyasaka, and Y. Shirai, "Novel photoelectrochemical cell with mesoscopic electrodes sensitized by lead-halide compounds (2)", in Proc. 210th ECS Meeting (ECS, 2006).

38 A. Kojima, K. Teshima, Y. Shirai, and T. Miyasaka, "Organometal halide perovskites as visible-light sensitizers for photovoltaic cells", J. Am. Chem. Soc., **131**, 6050 (2009). doi:10.1021/ja809598r

39 J. H. Im, C. R. Lee, J. W. Lee, S. W. Park, and N. G. Park, "6.5% efficient perovskite quantum-dot-sensitized solar cell", Nanoscale, **3**, 4088 (2011). doi:10.1039/c1nr10867k

40 H. S. Kim, C. R. Lee, J. H. Im, K. B. Lee, T. Moehl, A. Marchioro, S. J. Moon, R. Humphry-Baker, J. H. Yum, J. E. Moser, M. Gratzel, and N. G. Park, "Lead iodide perovskite sensitized all-solid-state submicron thin film mesoscopic solar cell with efficiency exceeding 9%", Sci. Rep., **2**, 591 (2012). doi:10.1038/srep00591

41 J. H. Noh, S. H. Im, J. H. Heo, T. N. Mandal, and S. I. Seok, "Chemical management for colorful, efcient, and stable inorganic-organic hybrid nanostructured solar cells.", Nano Lett., **13**, 1764 (2013).

42 J. Burschka, N. Pellet, S. J. Moon, R. Humphry-Baker, P. Gao, M. K. Nazeeruddin, and M. Gratzel, "Sequential deposition as a route to high-performance perovskite-sensitized solar cells", Nature, **499**, 316 (2013). doi:10.1038/nature12340

43 M. Liu, M. B. Johnston, and H. J. Snaith, "Efficient planar heterojunction perovskite solar cells by vapour deposition", Nature, **501**, 395 (2013). doi:10.1038/nature12509

44 W. S. Yang, J. H. Noh, N. J. Jeon, Y. C. Kim, S. Ryu, J. Seo, and S. I. Seok, "High-performance photovoltaic perovskite layers fabricated through intramolecular exchange", Science, **348**, 1234 (2015). doi:10.1126/science.aaa9272

45 M. Saliba, T. Matsui, J.-Y. Seo, K. Domanski, J.-P. Correa-Baena, M. K. Nazeeruddin, S. M. Zakeeruddin, W. Tress, A. Abate, A. Hagfeldt, and M. Gratzel, "Cesium-containing triple cation perovskite solar cells: Improved stability, reproducibility and high efficiency", Energy Environ. Sci., **9**, 1989 (2016). doi:10.1039/C5EE03874J

46 J. B. You, Z. R. Hong, Y. Yang, Q. Chen, M. Cai, T. B. Song, C. C. Chen, S. R. Lu, Y. S. Liu, and H. P. Zhou, "Low-temperature solution-processed perovskite solar cells with high efficiency and flexibility", ACS Nano, **8**, 1674 (2014). doi:Doi 10.1021/Nn406020d

47 Z. Xiao, C. Bi, Y. Shao, Q. Dong, Q. Wang, Y. Yuan, C. Wang, Y. Gao, and J. Huang, "Efficient, high yield perovskite photovoltaic devices grown by interdiffusion of solution-processed precursor stacking layers", Energy Environ. Sci., **7**, 2619 (2014). doi:10.1039/c4ee01138d

48 N. Ahn, D. Y. Son, I. H. Jang, S. M. Kang, M. Choi, and N. G. Park, "Highly reproducible perovskite solar cells with average efficiency of 18.3% and best efficiency of 19.7% fabricated via lewis base adduct of lead(ii) iodide", J. Am. Chem. Soc., **137**, 8696 (2015). doi:10.1021/jacs.5b04930

49 Y. Zhou, M. Yang, W. Wu, A. L. Vasiliev, K. Zhu, and N. P. Padture, "Room-temperature crystallization of hybrid-perovskite thin films via solvent–solvent extraction for high-performance solar cells", J. Mater. Chem. A, **3**, 8178 (2015). doi:10.1039/c5ta00477b

50 M. Xiao, F. Huang, W. Huang, Y. Dkhissi, Y. Zhu, J. Etheridge, A. Gray-Weale, U. Bach, Y.-B. Cheng, and L. Spiccia, "A fast deposition-crystallization procedure for highly efficient lead iodide perovskite thin-film solar cells ", Angew. Chem., **126**, 10056 (2014).

51 X. Li, D. Bi, C. Yi, J. D. Decoppet, J. Luo, S. M. Zakeeruddin, A. Hagfeldt, and M. Gratzel, "A vacuum flash-assisted solution process for high-efficiency large-area perovskite solar cells", Science, **353**, 58 (2016). doi:10.1126/science.aaf8060

52 O. Malinkiewicz, A. Yella, Y. H. Lee, G. M. Espallargas, M. Graetzel, M. K. Nazeeruddin, and H. J. Bolink, "Perovskite solar cells employing organic charge-transport layers", Nat. Photonics, **8**, 128 (2014). doi:Doi 10.1038/Nphoton.2013.141

53 Q. Lin, A. Armin, R. C. R. Nagiri, P. L. Burn, and P. Meredith, "Electro-optics of perovskite solar cells", Nat. Photonics, **9**, 106 (2014). doi:10.1038/nphoton.2014.284

54 D. Zhao, W. Ke, C. R. Grice, A. J. Cimaroli, X. Tan, M. Yang, R. W. Collins, H. Zhang, K. Zhu, and Y. Yan, "Annealing-free efficient vacuum-deposited planar perovskite solar cells with evaporated fullerenes as electron-selective layers", Nano Energy, **19**, 88 (2016). doi:10.1016/j.nanoen.2015.11.008

55 C.-W. Chen, H.-W. Kang, S.-Y. Hsiao, P.-F. Yang, K.-M. Chiang, and H.-W. Lin, "Efficient and uniform planar-type perovskite solar cells by simple sequential vacuum deposition", Adv. Mater., **26**, 6647 (2014). doi:10.1002/adma.201402461

56 H. A. Abbas, R. Kottokkaran, B. Ganapathy, M. Samiee, L. Zhang, A. Kitahara, M. Noack, and V. L. Dalal, "High efficiency sequentially vapor grown n-i-p ch3nh3pbi3 perovskite solar cells with undoped p3ht as p-type heterojunction layer", APL Materials, **3**, 016105 (2015). doi:10.1063/1.4905932

57 Q. Chen, H. Zhou, Z. Hong, S. Luo, H. S. Duan, H. H. Wang, Y. Liu, G. Li, and Y. Yang, "Planar heterojunction perovskite solar cells via vapor-assisted solution process", J. Am. Chem. Soc., **136**, 622 (2014). doi:10.1021/ja411509g

58 N. J. Jeon, J. H. Noh, Y. C. Kim, W. S. Yang, S. Ryu, and S. I. Seok, "Solvent engineering for high-performance inorganic-organic hybrid perovskite solar cells", Nat. Mater., **13**, 897 (2014). doi:10.1038/nmat4014

59 G. Balaji, P. H. Joshi, H. A. Abbas, L. Zhang, R. Kottokkaran, M. Samiee, M. Noack, and V. L. Dalal, "Ch3nh3pbi3 from non-iodide lead salts for perovskite solar cells via the formation of pbi2", Physical chemistry chemical physics : PCCP, **17**, 10369 (2015). doi:10.1039/c5cp00073d

60 Z. Xiao, Q. Dong, C. Bi, Y. Shao, Y. Yuan, and J. Huang, "Solvent annealing of perovskite-induced crystal growth for photovoltaic-device efficiency enhancement", Adv. Mater., **26**, 6503 (2014). doi:10.1002/adma.201401685

61 J. Liu, C. Gao, X. He, Q. Ye, L. Ouyang, D. Zhuang, C. Liao, J. Mei, and W. Lau, "Improved crystallization of perovskite films by optimized solvent annealing for high efficiency solar cell", ACS applied materials & interfaces, **7**, 24008 (2015). doi:10.1021/acsami.5b06780

62 M. Samiee, S. Konduri, B. Ganapathy, R. Kottokkaran, H. A. Abbas, A. Kitahara, P. Joshi, L. Zhang, M. Noack, and V. Dalal, "Defect density and dielectric constant in perovskite solar cells", Appl. Phys. Lett., **105**, 153502 (2014). doi:10.1063/1.4897329

63 S. D. Stranks, G. E. Eperon, G. Grancini, C. Menelaou, M. J. P. Alcocer, T. Leijtens, L. M. Herz, A. Petrozza, and H. J. Snaith, "Electron-hole diffusion lengths exceeding 1 micrometer in an organometal trihalide perovskite absorber", Science, **342**, 341 (2013). doi:10.1126/science.1243982

64 N. K. Noel, S. D. Stranks, A. Abate, C. Wehrenfennig, S. Guarnera, A.-A. Haghighirad, A. Sadhanala, G. E. Eperon, S. K. Pathak, M. B. Johnston, A. Petrozza, L. M. Herz, and H. J. Snaith, "Lead-free organic-inorganic tin halide perovskites for photovoltaic applications", Energy Environ. Sci., **7**, 3061 (2014). doi:10.1039/C4EE01076K

65 Y.-Y. Sun, J. Shi, J. Lian, W. Gao, M. L. Agiorgousis, P. Zhang, and S. Zhang, "Discovering lead-free perovskite solar materials with a split-anion approach", Nanoscale, **8**, 6284 (2016). doi:10.1039/C5NR04310G

66 F. Hao, C. C. Stoumpos, D. H. Cao, R. P. H. Chang, and M. G. Kanatzidis, "Lead-free solid-state organic-inorganic halide perovskite solar cells", Nat Photon, **8**, 489 (2014). doi:10.1038/nphoton.2014.82

67 T. A. Berhe, W.-N. Su, C.-H. Chen, C.-J. Pan, J.-H. Cheng, H.-M. Chen, M.-C. Tsai, L.-Y. Chen, A. A. Dubale, and B.-J. Hwang, "Organometal halide perovskite solar cells: Degradation and stability", Energy Environ. Sci., **9**, 323 (2016). doi:10.1039/C5EE02733K

68 X. Li, M. Ibrahim Dar, C. Yi, J. Luo, M. Tschumi, S. M. Zakeeruddin, M. K. Nazeeruddin, H. Han, and M. Grätzel, "Improved performance and stability of

perovskite solar cells by crystal crosslinking with alkylphosphonic acid ω-ammonium chlorides", Nat Chem, **7**, 703 (2015). doi:10.1038/nchem.2324

69 N. H. Tiep, Z. Ku, and H. J. Fan, "Recent advances in improving the stability of perovskite solar cells", Adv. Energy Mater., **6**, n/a (2016). doi:10.1002/aenm.201501420

70 S. D. Stranks and H. J. Snaith, "Metal-halide perovskites for photovoltaic and light-emitting devices", Nat Nano, **10**, 391 (2015). doi:10.1038/nnano.2015.90

71 I. Hwang, I. Jeong, J. Lee, M. J. Ko, and K. Yong, "Enhancing stability of perovskite solar cells to moisture by the facile hydrophobic passivation", ACS Appl. Mater. Interfaces, **7**, 17330 (2015). doi:10.1021/acsami.5b04490

72 N. V. Yastrebova, *High-efficiency multi-junction solar cells: Current status and future potential*. (Sunlab, 2007).

73 S. R. Kurtz, P. Faine, and J. M. Olson, "Modeling of two-junction, series-connected tandem solar cells using top-cell thickness as an adjustable parameter", J. Appl. Phys., **68**, 1890 (1990). doi:10.1063/1.347177

74 S. A. Kulkarni, T. Baikie, P. P. Boix, N. Yantara, N. Mathews, and S. Mhaisalkar, "Band-gap tuning of lead halide perovskites using a sequential deposition process", J. Mater. Chem. A., **2**, 9221 (2014). doi:10.1039/C4TA00435C

75 G. E. Eperon, T. Leijtens, K. A. Bush, R. Prasanna, T. Green, J. T. Wang, D. P. McMeekin, G. Volonakis, R. L. Milot, R. May, A. Palmstrom, D. J. Slotcavage, R. A. Belisle, J. B. Patel, E. S. Parrott, R. J. Sutton, W. Ma, F. Moghadam, B. Conings, A. Babayigit, H. G. Boyen, S. Bent, F. Giustino, L. M. Herz, M. B. Johnston, M. D. McGehee, and H. J. Snaith, "Perovskite-perovskite tandem photovoltaics with optimized band gaps", Science, **354**, 861 (2016). doi:10.1126/science.aaf9717

76 Y. Han, S. Meyer, Y. Dkhissi, K. Weber, J. M. Pringle, U. Bach, L. Spiccia, and Y.-B. Cheng, "Degradation observations of encapsulated planar ch3nh3pbi3 perovskite solar cells at high temperatures and humidity", J. Mater. Chem. A., **3**, 8139 (2015). doi:10.1039/C5TA00358J

77 H. C. Weerasinghe, Y. Dkhissi, A. D. Scully, R. A. Caruso, and Y.-B. Cheng, "Encapsulation for improving the lifetime of flexible perovskite solar cells", Nano Energy, **18**, 118 (2015). doi:10.1016/j.nanoen.2015.10.006

78 J. You, L. Meng, T.-B. Song, T.-F. Guo, Y. Yang, W.-H. Chang, Z. Hong, H. Chen, H. Zhou, Q. Chen, Y. Liu, N. De Marco, and Y. Yang, "Improved air stability of perovskite solar cells via solution-processed metal oxide transport layers", Nat Nano, **11**, 75 (2016). doi:10.1038/nnano.2015.230

79 T. Leijtens, G. E. Eperon, S. Pathak, A. Abate, M. M. Lee, and H. J. Snaith, "Overcoming ultraviolet light instability of sensitized tio(2) with meso-

superstructured organometal tri-halide perovskite solar cells", Nat. Commun., **4**, 2885 (2013). doi:10.1038/ncomms3885

80 S. Guarnera, A. Abate, W. Zhang, J. M. Foster, G. Richardson, A. Petrozza, and H. J. Snaith, "Improving the long-term stability of perovskite solar cells with a porous al2o3 buffer layer", J. Phys. Chem. Lett., **6**, 432 (2015). doi:10.1021/jz502703p

81 M. Bag, L. A. Renna, R. Y. Adhikari, S. Karak, F. Liu, P. M. Lahti, T. P. Russell, M. T. Tuominen, and D. Venkataraman, "Kinetics of ion transport in perovskite active layers and its implications for active layer stability", J. Am. Chem. Soc., **137**, 13130 (2015). doi:10.1021/jacs.5b08535

82 H. J. Snaith, A. Abate, J. M. Ball, G. E. Eperon, T. Leijtens, N. K. Noel, S. D. Stranks, J. T.-W. Wang, K. Wojciechowski, and W. Zhang, "Anomalous hysteresis in perovskite solar cells", J. Phys. Chem. Lett., **5**, 1511 (2014). doi:10.1021/jz500113x

83 H.-S. Kim and N.-G. Park, "Parameters affectingi–vhysteresis of ch3nh3pbi3perovskite solar cells: Effects of perovskite crystal size and mesoporous tio2layer", J. Phys. Chem. Lett., **5**, 2927 (2014). doi:10.1021/jz501392m

84 R. S. Sanchez, V. Gonzalez-Pedro, J. W. Lee, N. G. Park, Y. S. Kang, I. Mora-Sero, and J. Bisquert, "Slow dynamic processes in lead halide perovskite solar cells. Characteristic times and hysteresis", J. Phys. Chem. Lett., **5**, 2357 (2014). doi:10.1021/jz5011187

85 E. L. Unger, E. T. Hoke, C. D. Bailie, W. H. Nguyen, A. R. Bowring, T. Heumüller, M. G. Christoforo, and M. D. McGehee, "Hysteresis and transient behavior in current–voltage measurements of hybrid-perovskite absorber solar cells", Energy Environ. Sci., **7**, 3690 (2014). doi:10.1039/c4ee02465f

86 J. Wei, Y. Zhao, H. Li, G. Li, J. Pan, D. Xu, Q. Zhao, and D. Yu, "Hysteresis analysis based on the ferroelectric effect in hybrid perovskite solar cells", J. Phys. Chem. Lett., **5**, 3937 (2014). doi:10.1021/jz502111u

87 O. Almora, I. Zarazua, E. Mas-Marza, I. Mora-Sero, J. Bisquert, and G. Garcia-Belmonte, "Capacitive dark currents, hysteresis, and electrode polarization in lead halide perovskite solar cells", J. Phys. Chem. Lett., **6**, 1645 (2015). doi:10.1021/acs.jpclett.5b00480

88 B. C. O'Regan, P. R. Barnes, X. Li, C. Law, E. Palomares, and J. M. Marin-Beloqui, "Optoelectronic studies of methylammonium lead iodide perovskite solar cells with mesoporous tio(2): Separation of electronic and chemical charge storage, understanding two recombination lifetimes, and the evolution of band offsets during j-v hysteresis", J. Am. Chem. Soc., **137**, 5087 (2015). doi:10.1021/jacs.5b00761

89 W. Tress, N. Marinova, T. Moehl, S. M. Zakeeruddin, M. K. Nazeeruddin, and M. Grätzel, "Understanding the rate-dependent j–v hysteresis, slow time component, and aging in ch3nh3pbi3perovskite solar cells: The role of a compensated electric field", Energy Environ. Sci., **8**, 995 (2015). doi:10.1039/c4ee03664f

90 J. Beilsten-Edmands, G. E. Eperon, R. D. Johnson, H. J. Snaith, and P. G. Radaelli, "Non-ferroelectric nature of the conductance hysteresis in ch3nh3pbi3 perovskite-based photovoltaic devices", Appl. Phys. Lett., **106**, 173502 (2015). doi:10.1063/1.4919109

91 H. W. Chen, N. Sakai, M. Ikegami, and T. Miyasaka, "Emergence of hysteresis and transient ferroelectric response in organo-lead halide perovskite solar cells", J. Phys. Chem. Lett., **6**, 164 (2015). doi:10.1021/jz502429u

92 C. Huang, C. Liu, Y. Di, W. Li, F. Liu, L. Jiang, J. Li, X. Hao, and H. Huang, "Efficient planar perovskite solar cells with reduced hysteresis and enhanced open circuit voltage by using pw12-tio2 as electron transport layer", ACS applied materials & interfaces, **8**, 8520 (2016). doi:10.1021/acsami.6b00846

93 J. M. Frost, K. T. Butler, F. Brivio, C. H. Hendon, M. van Schilfgaarde, and A. Walsh, "Atomistic origins of high-performance in hybrid halide perovskite solar cells", Nano Lett., **14**, 2584 (2014). doi:10.1021/nl500390f

94 Z. Fan, J. Xiao, K. Sun, L. Chen, Y. Hu, J. Ouyang, K. P. Ong, K. Zeng, and J. Wang, "Ferroelectricity of ch3nh3pbi3 perovskite", J. Phys. Chem. Lett., **6**, 1155 (2015). doi:10.1021/acs.jpclett.5b00389

95 J. M. Azpiroz, E. Mosconi, J. Bisquert, and F. De Angelis, "Defect migration in methylammonium lead iodide and its role in perovskite solar cell operation", Energy Environ. Sci., **8**, 2118 (2015). doi:10.1039/C5EE01265A

96 C. Eames, J. M. Frost, P. R. F. Barnes, B. C. O/'Regan, A. Walsh, and M. S. Islam, "Ionic transport in hybrid lead iodide perovskite solar cells", Nat. Commun., **6** (2015). doi:10.1038/ncomms8497

97 A. Buin, P. Pietsch, J. Xu, O. Voznyy, A. H. Ip, R. Comin, and E. H. Sargent, "Materials processing routes to trap-free halide perovskites", Nano Lett., **14**, 6281 (2014). doi:10.1021/nl502612m

98 Z. Xiao, Y. Yuan, Y. Shao, Q. Wang, Q. Dong, C. Bi, P. Sharma, A. Gruverman, and J. Huang, "Giant switchable photovoltaic effect in organometal trihalide perovskite devices", Nat. Mater., **14**, 193 (2015). doi:10.1038/nmat4150

99 A. Walsh, D. O. Scanlon, S. Chen, X. G. Gong, and S. H. Wei, "Self-regulation mechanism for charged point defects in hybrid halide perovskites", Angewandte Chemie, **54**, 1791 (2015). doi:10.1002/anie.201409740

100 I. Levine, P. K. Nayak, J. T.-W. Wang, N. Sakai, S. Van Reenen, T. M. Brenner, S. Mukhopadhyay, H. J. Snaith, G. Hodes, and D. Cahen, "Interface-dependent ion migration/accumulation controls hysteresis in mapbi3 solar cells", J. Phys. Chem. C, **120**, 16399 (2016). doi:10.1021/acs.jpcc.6b04233

101 J. Bhattacharya, R. W. Mayer, M. Samiee, and V. L. Dalal, "Photo-induced changes in fundamental properties of organic solar cells", Appl. Phys. Lett., **100**, 193501 (2012). doi:10.1063/1.4711806

102 P. H. Joshi, L. Zhang, I. M. Hossain, H. A. Abbas, R. Kottokkaran, S. P. Nehra, M. Dhaka, M. Noack, and V. L. Dalal, "The physics of photon induced degradation of perovskite solar cells", AIP Advances, **6**, 115114 (2016). doi:10.1063/1.4967817